



Pilkington Library

Author/Filing Title DAVILA, A.

Accession/Copy No. 040129736

Vol. No. Class Mark

26 JUN 1998	LOAN COPY 12 MAY 2000
25 JUN 1999	
14 JAN 2000	
14 JAN 2000	

0401297365



BADMINTON PRESS
18 THE HALFBOOTS
LEICESTER LE11 1LD
ENGLAND
TEL: 0116 269 2917
FAX: 0116 269 6639


Transient Displacement Analysis using Double Pulsed ESPI and Fringe Processing Methods

A. Dávila ¹

Department of Mechanical Engineering
Loughborough University of Technology

July, 1996

¹Supported by Consejo Nacional de Ciencia y Tecnología and Centro de Investigaciones en Optica (México)

 University of Toronto Library
Date Feb 97
Class
Acc No. 040129736

9/6/51991

To my lovely wife and family

ACKNOWLEDGEMENTS

This work was carried out in the Department of Mechanical Engineering at Loughborough University of Technology between October 1992 and November 1995, and was supervised by Dr David Kerr, whose encouragement and advice have been much appreciated. The Director of Research was N. Halliwell. Funding was provided by Consejo Nacional de Ciencia y Tecnología and Centro de Investigaciones en Optica (México).

I would like to thank to my friend and colleague Professor Guillermo Kaufmann who has collaborated closely with me on several research aspects. Very special thanks also to all the members of the Optics Group for support and assistance on many occasions, in particular Jon Petzing, Mark Reeves, George Graham, Robert Boyd and Terry West. Thanks also to staff and postgraduate researchers in the Department of Mechanical Engineering who have made my time at Loughborough University more enjoyable. Thanks are also due to the technical staff in the department for their contributions, especially Vince Scothern for photographic work.

Contents

0.1	Introduction	2
1	Non Destructive Optical Techniques	8
1.1	Single Point Optical Displacement Measurement	10
1.2	Whole Field Optical Displacement Measurement	10
2	Electronic Speckle Pattern Interferometry Devices	19
2.1	Basic devices	20
2.2	Industrial Applications	24
2.3	Problems with Current ESPI Devices	25
2.4	Noise Reduction Techniques	27
2.4.1	Noise Consequences in Displacement Measurement	29
2.4.2	Standard Techniques	33

2.5	Enhancement of Addition Fringe Patterns	35
2.5.1	Enhancement of Addition fringes by zero order re- moval	36
2.6	Phase Extraction Methods	39
2.6.1	Phase Stepping	39
2.6.2	Fourier Transform	41
2.6.3	Carrier Fringes	44
2.7	Whole Field Transient Event Detection	46
2.7.1	Multicamera Phase Stepping	48
2.7.2	Spatial Phase-Shifting Method	50
3	Phase Encoded Displacement Measurement by Speckle Cor- relation	57
3.1	Speckle Phenomena and Interference	58
3.2	Coherent combination of Speckle and Uniform Fields	65
3.3	Coherent combination of Speckle Fields	66
3.4	Addition of Fields in Intensity Basis	66
3.5	Correlation	68

	3
4 Fringe Quality Assessment	70
4.1 Simulation of ESPI fringe patterns	71
4.1.1 Interference	71
4.1.2 Sampling Consequences	73
4.1.3 Correlation	74
4.2 Assessment of Speckle Noise Reduction	77
5 Noise Reduction Techniques	83
5.1 Synthetic Aperture Radar Techniques	83
5.2 Spectral Subtraction Image Restoration	97
5.3 Noise Reduction Using a Scale-Space Filter	104
5.4 Summary and Remarks	113
6 Enhancement of Addition Fringe Patterns	118
6.1 Experimental Enhancement of Addition Fringes by Zero Order Removal	119
6.2 Enhancement of Addition Fringes by Subtraction of a Refer- ence Interferogram	122
7 Phase Extraction Methods	124

7.1	Carrier fringe limitations	124
7.2	Phase Unwrapping Algorithm	127
8	Whole Field Transient Event Detection	134
8.1	High Speed Optical System for Carrier Generation	135
8.2	Discussion of Trade-offs	153
9	Discussions and Conclusions	158
9.1	Future of Opto-Electronic Developments	158
9.2	Assessment of Speckle Noise	160
9.3	Noise Reduction Techniques	161
9.4	Phase Extraction	162
9.5	Systems for Transient Event Detection	163
9.6	Future Applications in ESPI	164

Abstract

This thesis deals with techniques for the displacement measurement of fast transient phenomena using ESPI. Four main contributions are presented. First, a computer model for speckle noise and ESPI fringe generation is proposed. An assessment methodology for speckle noise reduction algorithms is then derived using the computer model. Then the noise in the ESPI fringe patterns is analyzed using computer generated speckle and several solutions for its reduction are proposed and assessed. Finally, a fast electro-optical system is presented as a solution to the unambiguous phase extraction problem from a single interferogram. With this novel system, whole field transient displacements occurring in time intervals as short as 20ns can be successfully registered and retrieved.

The work done was directed first towards the noise reduction and enhancement of speckled fringe patterns correlated mainly by addition. As only a single interferogram is available when double pulse lasers are used to record the transient events, the methods proposed here are mainly suitable for these kind of fringe patterns. A computer model for speckle generation was developed for noise reduction assessment purposes. Secondly, ESPI technology has been extended in its capabilities to deal with a broader range of phenomena in the time domain. At the present time there is no satisfactory method of obtaining continuous space and time coverage simultaneously. The solution presented here provides a novel alternative to tackle this problem, in particular, whole field transient displacement detection and the problem of unambiguous phase extraction from a single addition interferogram.

0.1 Introduction

Since 1978, considerable interest has been shown in the measurement of high speed displacements using Electronic Speckle Pattern Interferometry (ESPI) or TV Holography [1, 2, 3]. This thesis will deal mainly with the techniques for high speed analysis and processing of the ESPI fringe patterns.

Analysis of high speed displacements can be carried out at rough scale by observing the movement of mechanical components using very fast cameras ¹. However, this approach fails to show the strain of the material components, mainly because it occurs at very small scales, of the order of the wavelength of visible light. To analyze successfully very small displacements (or strain), various interferometric techniques have been developed in past years [5] such as holographic and speckle pattern interferometry that provide spatial coverage of a surface. Although this techniques obtains spatial information of displacement, at the present there is no satisfactory method of obtaining continuous space and time coverage simultaneously.

Electronic speckle pattern interferometry is a nondestructive, whole field technique to measure static and dynamic deformations of a diffuse object [6]. It was first developed by Butters and Leendertz [7] at Loughborough University of Technology and contemporaneously by Macovski [8]. Before this

¹To observe displacement in very short time intervals, high speed cameras have been developed to record transient events. Nowadays, the film based cameras (rotating mirror cameras) can reach speeds of the order of 25 million frames per second and video cameras of the order of 10 million of frames per second for the latest models [4]. However, as they are designed to capture just images, they fail to show figures of displacements smaller than their spatial resolution.

technique, holographic interferometry (HI) had proved to be more efficient in terms of spatial resolution for deformation measurement [9]. But nowadays, the cost of electronic technology is decreasing while availability and quality are continuously increasing. Moreover, the absence of chemical or thermal process, and unlimited supply of images make ESPI an excellent alternative among the non-destructive displacement measuring techniques.

When compared with HI, ESPI techniques typically have less precision for measurement purposes. This is due to different phenomena occurring in each step of the imaging, acquisition and correlation processes. At this last step, the noisy nature of the fringe patterns can be easily perceived, and the requirement of a noise reduction plan becomes evident.

When continuous wave (cw) lasers are used, HI and ESPI exhibit another important disadvantage: both techniques require isolation tables to avoid detecting mechanical perturbations generated from other sources than the system under test. To avoid isolation, high speed acquisition can be used to analyze the range of displacements of interest. For this purpose, speckle interferometry has been used with fast cameras [10]. Nevertheless, just a limited number of frames can be obtained and the analysis procedure has to wait for the development of the photographic media. An equivalent technique can be implemented using fast video cameras and ESPI. Unfortunately as more speed is needed, fast cameras become more expensive and their spatial resolution tends to decrease.

During the last decade, applications outside the stable laboratory environment induced the use of pulsed lasers in ESPI [1] to reduce the stability requirements of cw lasers. Nowadays, the most flexible of such lasers is the

twin pulsed, diode seeded Nd:YAG laser [11, 2]. This is composed of two identical cavities which are capable of emitting double pulses that can be synchronized with the TV frame rate. Both oscillators are seeded by the same diode laser so as to produce two mutually coherent pulses with the same intensity and variable separation.

Pulsed ESPI has most commonly been used with this laser operating in the single pulse mode. In this case, the time separation between two correlated exposures is relatively large (≥ 40 ms), so that interferograms are recorded on separate TV frames and then digitally subtracted in a frame grabber. The subtraction process not only correlates both interferograms to produce a fringe pattern, but also ensures a significant reduction of the speckle noise. Thus, subtraction fringes are usually of good quality and sufficiently smooth to allow the use of phase stepping methods for automating the displacement evaluation [12].

It was soon discovered that the relatively large time separations between single pulses made this last technique quite sensitive to experimental instabilities. Also, it did not allow the study of several important phenomena such as power flow and high speed transient ² events. In fact, one of the recent concerns in engineering is to analyze the transmission of energy [13, 14] in mechanical systems. A car collision experiment is a potential example of a transient transmission of energy, where the main concern is to optimize the

²For practical purposes in this work, a transient event will be defined as a displacement, assumed non-repeatable, which has a duration of less than 1/30 of a second i.e. one TV frame time for the NTSC system.

absorption of energy along propagation paths through its shock absorbing structures.

These problems can be overcome by operating the laser in the twin pulse mode in which two pulses are fired during one exposure. As a consequence of the small time separations, typically from 10ns to 500 μ s, both interferograms are added in the TV camera to produce a single video image.

Even though the addition operation still produces correlation fringes, it does not remove the fixed pattern noise, so the result is that addition fringes have a very low visibility. Standard noise reduction methods, have not proved to be sufficient for subsequent automatic computer analysis and phase values are usually corrupted by noise. Another important drawback introduced by the addition operation is that only a single interferogram is recorded, so phase stepping techniques can not be applied and the standard phase extraction methods produce ambiguous phase [15].

In this thesis, two main contributions are presented. First, noise in the ESPI fringe patterns is analyzed using computer generated speckle and several solutions for its reduction are proposed using a novel assessment technique. Secondly, a fast electro-optical system is presented as a solution to the unambiguous phase extraction problem from a single interferogram. With this novel system, whole field transient displacements occurring in time intervals as short as 20ns can be successfully registered. The aim of this work is to take ESPI technology a step forward in its use not only as a whole field technique but to extend its capabilities to deal with a broader range of phenomena in the time domain. By developing techniques for the analysis of pulsed fringe patterns and the design of the electro-optical system to extract

displacement data from those patterns, this aim has been successfully fulfilled. The high speed achieved in the capture of ESPI pulsed fringe patterns using conventional CCD cameras, extends the range of transient analysis to intervals of time never achieved before. It is expected that the engineering community will benefit from the application of this technique in its study of fast displacement phenomena, and also as a replacement for some traditional techniques.

Chapter one starts with a review of the most common non-destructive optical systems for single point and whole field displacement measurement.

In chapter two, first the standard ESPI devices are reviewed together with their industrial applications and a discussion of the main problems of this technology. Secondly, three fundamental techniques applied to the ESPI fringe patterns are reviewed: noise reduction, enhancement of addition fringe patterns and phase extraction methods. In the noise reduction techniques, the noise consequences in displacement measurement are first discussed followed by a review of the standard techniques for noise reduction. The problem of enhancement of addition fringe patterns is also reviewed and several solutions are discussed. As a complement, the last subsection includes a review of the most common phase extraction methods. Finally, the last section of chapter two includes a review of the recent techniques to measure whole field transient displacement,

In chapter three, the speckle phenomena basics and their role in the representation of displacement is described.

Starting with a computer model to simulate ESPI main phenomena, chapter

four gives an idea of the expected behaviour of an ESPI under ideal conditions. This computer techniques are complemented with a novel method for assesment of the processed fringe patterns.

In chapter five, the techniques explored in this work to reduce noise in the fringe patterns are presented and evaluated using the computer model and the assessment techniques previously introduced.

Chapter six deals with the problem of experimental enhancement of addition fringe patterns and several solutions are discussed.

In chapter seven the performance of the carrier fringe technique for phase extraction is evaluated for ESPI fringe patterns and the phase unwrapping algorithm used in this work is reviewed.

Chapter eight presents the author's solution to the whole field transient displacement detection and to the problem of unambiguous phase extraction from a single interferogram. Finally, chapter nine present conclusions and future work.

Chapter 1

Non Destructive Optical Techniques

Optical techniques are not the only way of measuring displacement. Displacement transducers are currently found in the designers toolbox; these devices can use different physical properties as shown in table 1.1.

The first four techniques represent most of the time a cheap solution for certain cases of point measurement. Nonetheless, the Non Destructive Optical Techniques (NDOT) are usually preferred (despite their relative expense) because they are non-contact and have the great advantage of leaving the object under test intact.

Two current trends exist nowadays for the use NDOT for displacement measurement; single point and whole field measurements. Their main difference is that single point techniques provide a very high resolution in time but not

in space. In contrast, the whole field measurements provide spatial information but are not able to provide a high resolution in time. The first section of this chapter deals with these two techniques for single point and whole field measurements.

Physical Property	Transducer	Consequence of Test	Area
Capacitance	Strain Gages	Possible Destruction	Point
Resistance	Strain Gages	Possible Destruction	Point
Magnetic Flux	Point Profilometers	Possible Destruction	Point
Piezoelectric Effect	Accelerometers	Possible Destruction	Point
Optical Path Difference	Non Destructive Optical Techniques	None	Point and Whole Field

Table 1.1: Physical properties of transducers, possible consequences and area of application.

Two non-destructive optical methods are first discussed in this chapter, restricted to the techniques that can provide displacement measures of the order of the wavelength of the light used in the test. The first is a single point technique that provides the analysis of surface displacements at high speed but gives only a partial idea of the phenomena occurring in a whole area. The second, describes several whole field techniques and compares them in their attempt to provide information of displacements at high speeds.

1.1 Single Point Optical Displacement Measurement

The most successful technique for single point measurement is the Laser Doppler Vibrometer (LDV) [16]. Figure 1.1 shows an schematic diagram of an LDV. A time phase shift is continuously introduced by a reference beam represented as R in the diagram. The interference of this beam with the light that is reflected by the object is then registered in the detector. Assuming that the object is static, the intensity pattern is then oscillating with a frequency proportional to the velocity of the phase shift. As the object moves, this frequency suffers a shift proportional to the velocity of the object.

The electronics after the detector produces an analogue signal proportional to the difference of frequencies generated by the reference beam and the object beam. As a standard addition in the commercial LDV it is possible to measure displacement directly. The actual limitation of this device is that as a single point is measured, it is necessary to scan the object under test to obtain a complete analysis of the whole object. However, time resolution is in general very high of the order of $20\mu\text{s}$ [17].

1.2 Whole Field Optical Displacement Measurement

As seen in the last section, point techniques provide very fast analysis of displacements, but lack spatial resolution. To obtain whole field measure-

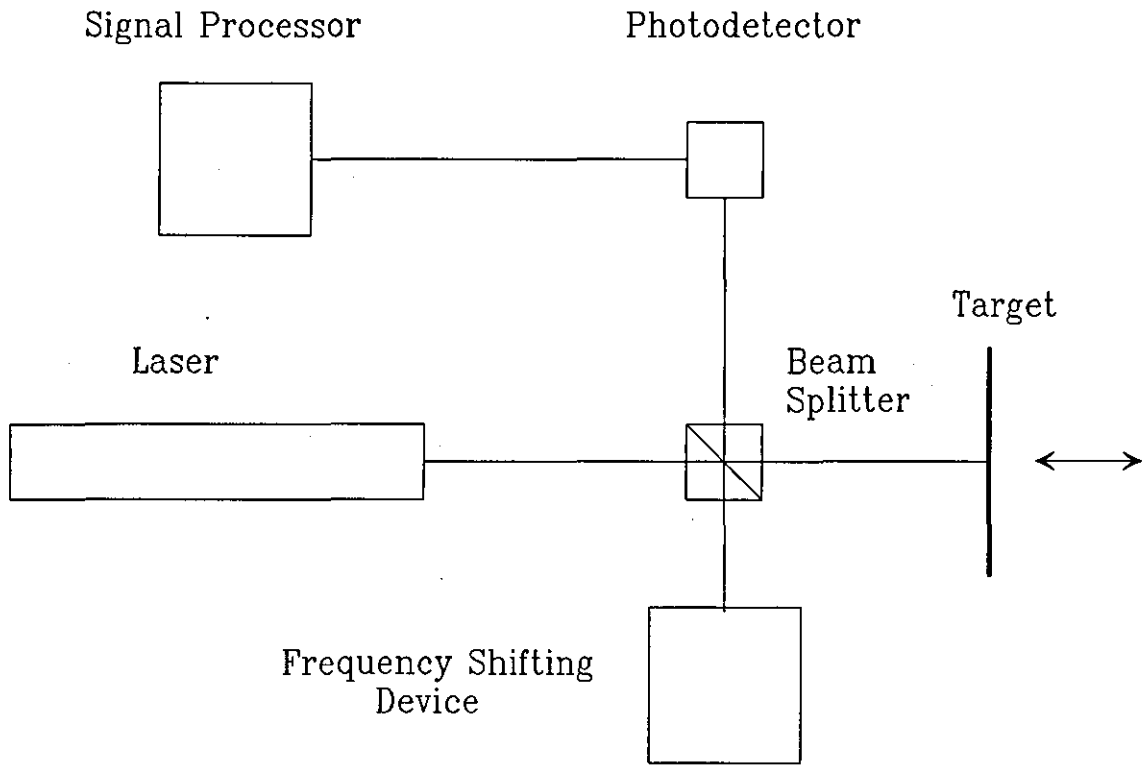


Figure 1.1: Diagram of a Laser Doppler Vibrometer

ments usually it is necessary to use two-dimensional detectors such as films or electronic cameras.

There are multiple optical approaches to determine displacements of the order of the wavelength of light using two-dimensional detectors: Holographic Interferometry, Speckle Pattern Photography, Speckle Pattern Correlation Interferometry, Moiré Interferometry.

Holographic Interferometry was the first technique capable of measuring very small displacements and was developed from the very well know technique of holography.

A typical arrangement is shown in figure 1.2. Two wavefronts are recorded in the same hologram by a double exposure of the holographic plate. When the double exposure is made, a slight distortion of the object is introduced between exposures. Then the reconstruction of the hologram by the reference beam when the plate is in exactly the original geometry (and without object beam) gives fringes crossing the reconstructed image. These fringes represent the displacement introduced between exposures.

HI has been shown to be very successful if a thermoplastic recording medium is used. Nonetheless, real time observation is not possible due to the processing time of 50 seconds. Another problem is that the thermoplastic medium is reusable for a limited number of exposure-erasure cycles, in some cases only 300 consecutive cycles are guaranteed for each thermoplastic plate [18].

Moiré interferometry [19, 20] is an alternative technique to measure displacements at small scales. Capable of achieving very high resolutions with grat-

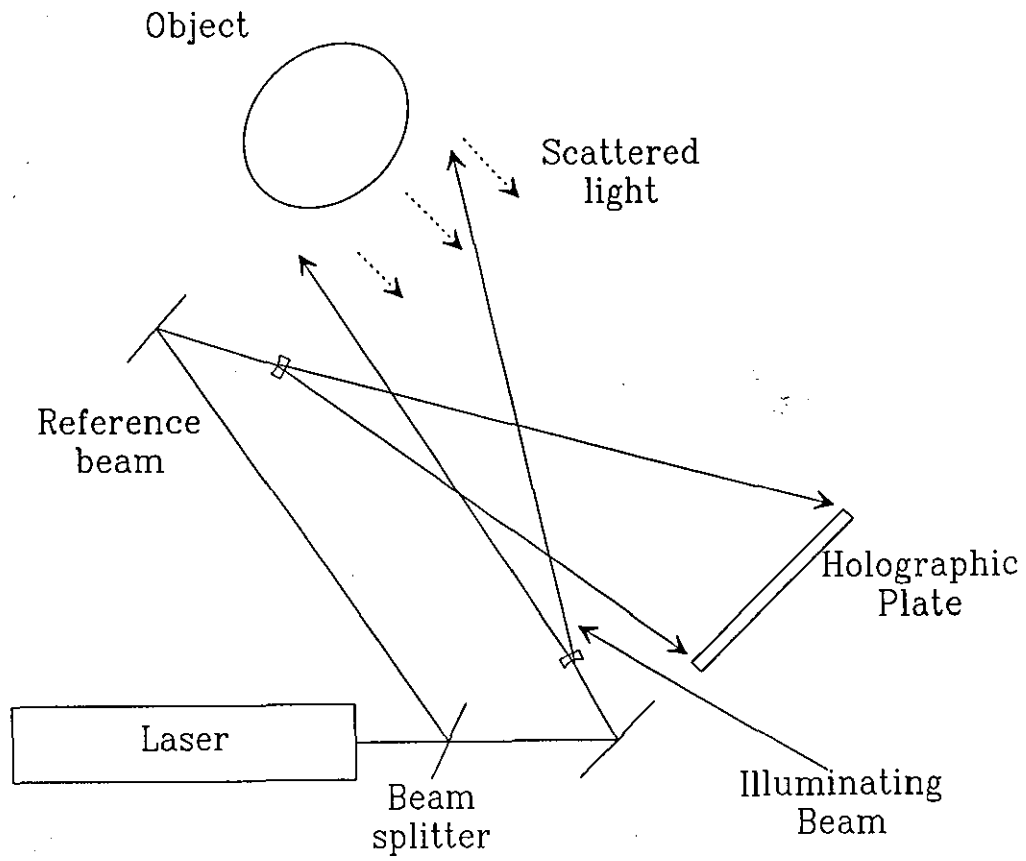


Figure 1.2: Diagram illustrating the principle of holographic interferometry

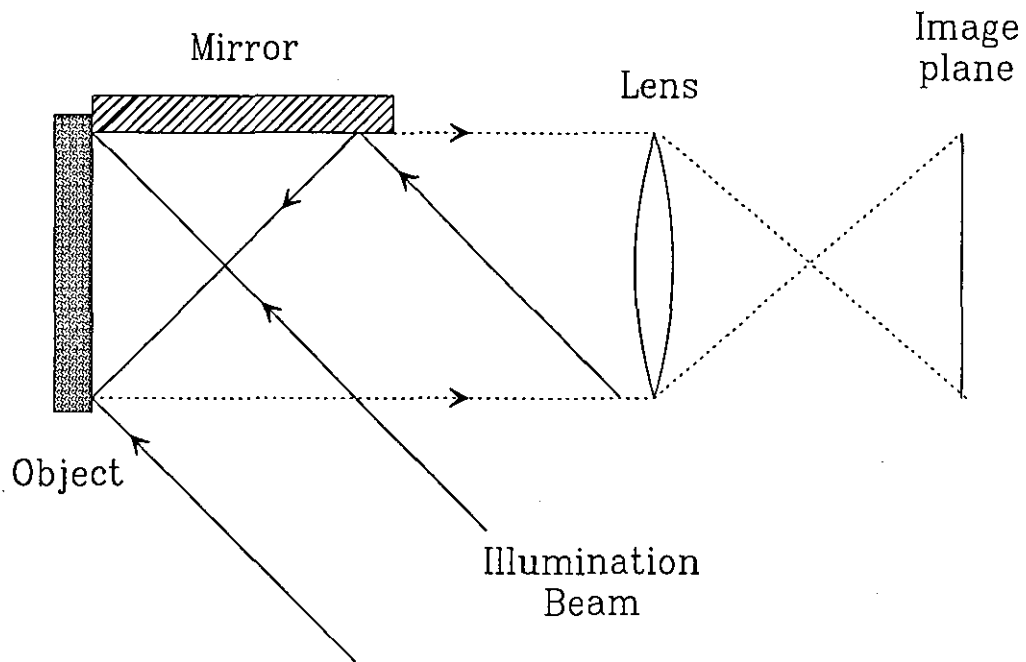


Figure 1.3: Diagram illustrating the principle of Moiré interferometry

ings of 4000 1/mm, this technique requires a flat surface to apply a very fine grating whose deformations are used to obtain interference between the diffracted orders.

This technique has several disadvantages, as the grating (Fig. 1.2) must be attached to the surface under test, the technique ceases to be non-invasive to a certain extent. As suggested by [21] most of the problems with contact transducers originate in the couplant, usually they can not be used over a sufficiently wide temperature range for all applications. And there is also concern about possible chemical attack.

As phase stepping methods are used to extract the phase in this technique, only the camera speed and the time spent in the phase stepping procedure

limit this technique from being capable of near real time processing; of course if the time spend to attach the grating is neglected.

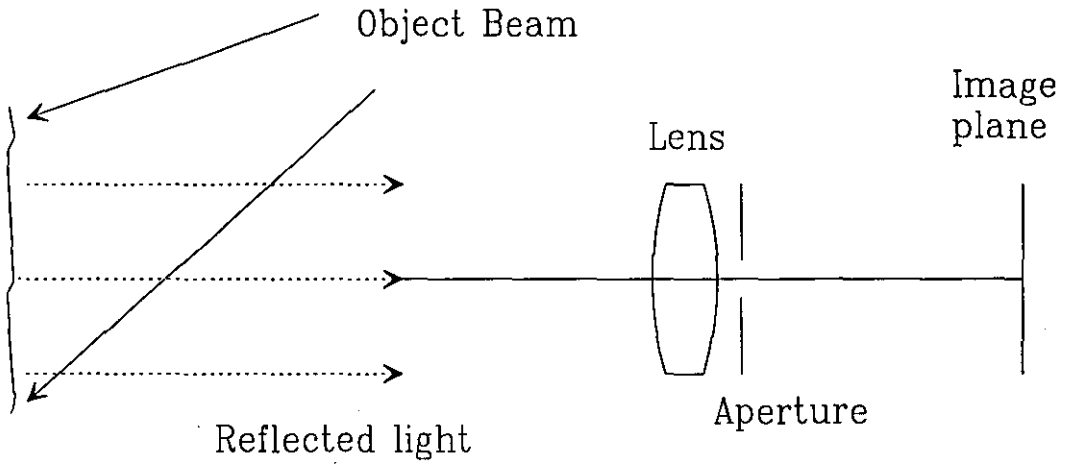
Speckle photography can be used to measure displacements by using only an object beam as shown in figure 1.4(a) for in-plane measurement. In this technique, two exposures are taken, before and after displacement.

A post-processing step is required to analyze the correlation generated as shown in figure 1.4(b). As no reference beam is used to produce correlation, speckle displacement can only be correlated in a local area determined by the speckle size. Even so, high speeds systems using speckle photography have been developed [10], the main disadvantage of this technique is the need of a pre-processing step as well as the problems associated with the film processing.

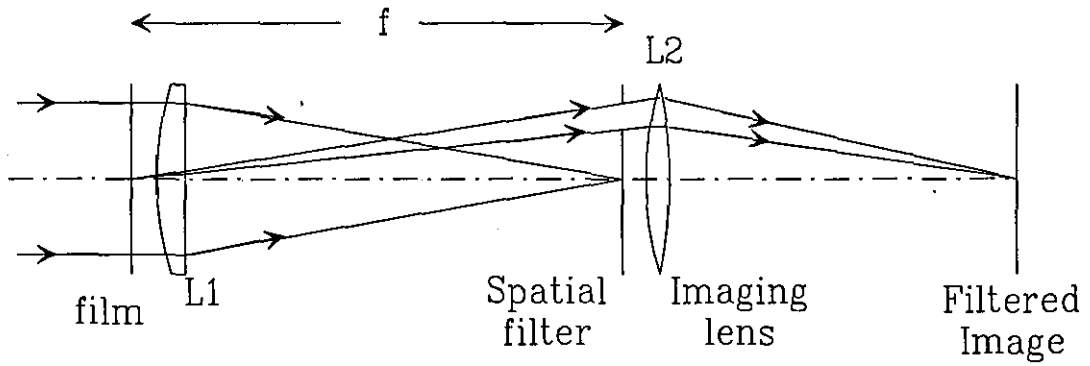
Speckle Pattern Correlation Interferometry differs from speckle photography in that it involves the interference of a uniform reference field or another speckle field (e.g. see section 3). This interference produces correlation fringes, first observed [22, 23] in the study of vibrating objects. Later film was used to record the correlation fringes [24, 25, 26].

Soon it was realized that film could be avoided if cameras and electronic devices were used to produce the correlation effect [7, 8]. This technology was known as ESPI or TV holography. As the nature of the detector was different new phenomena were introduced and required an analysis of the fringe contrast which was studied by Slettemoen [27, 28, 29].

The use of pulsed lasers gave some additional advantages for the application



(a)



(b)

Figure 1.4: Optical setup for (a) in-plane speckle photography, (b) observation of in-plane displacements

of ESPI in industrial environments [1]. The first pulsed lasers used in ESPI were of ruby type, which Q-switched twice within one flash tube cycle produced two laser pulses in a time interval between $10\mu\text{s}$ to 1ms with a pulse width of about $20\text{-}50\text{ns}$. Unfortunately, if new interferograms were required, the laser could give only one every ten seconds. This limited strongly the supply of continuous images for TV rates. A preliminary solution to this problem was the Q-switched Nd:YAG laser [30], which was able to sustain double pulse repetition at TV rates. However, when operating in Q-switched mode, fluctuations of intensity (spatially and temporally) introduce a very low quality in visibility of the fringe pattern. To overcome this problem, the use of two identical cavities and a seeding diode laser, has been shown to reduce the temporal instability in intensity. This happens when both oscillators are seeded by the same diode laser so as to produce two mutually coherent pulses with variable separation [31]. This laser was capable of reducing even more the double pulse separation and to provide an unlimited supply of twin pulses with constant intensity. It also gave unprecedented advantages for the analysis of transient events.

As lasers evolved to produce smaller times between pulses, this time capability was not followed by the camera technology. So standard cameras were modified to cope with the small times required to analyse transient events [30]. Acquisition times of 200ms for single cavity Nd:YAG double pulse laser have been achieved with an interline-transfer CCD. However, as a single pattern was possible phase stepping techniques were impossible to apply. To overcome this problem, the use of larger speckle sizes with tilted reference beams has allowed encoding of several phase steps before correlation [3, 32]. However, until the writing of this thesis, this approach has been

only tested using single pulse ruby lasers. Nonetheless, transient events have been analysed using this method with time resolutions greater than $30\mu\text{s}$ with the consequent disadvantage of the low repetition rate.

Chapter 2

Electronic Speckle Pattern Interferometry Devices

In this chapter, first the standard ESPI devices are reviewed ¹ together with their industrial applications and a discussion of the main problems of this technology. Secondly, three fundamental techniques applied to the ESPI fringe patterns are reviewed: noise reduction, enhancement of addition fringe patterns and phase extraction methods. In the noise reduction techniques, the noise consequences in displacement measurement are first discussed followed by a review of the standard techniques for noise reduction. The problem of enhancement of addition fringe patterns is also reviewed and several solutions are discussed. As a complement, the last subsection includes a review of the most common phase extraction methods. Finally, the last section

¹The reader can find a more detailed explanation in reference [6].

of this chapter includes a review of two recent techniques to measure whole field transient displacement,

2.1 Basic devices

There are three basic configurations of ESPI systems. In each configuration displacement is represented in a different way. The most common configuration is the out-of-plane ESPI, in this optical arrangement, displacement is expressed as a change in the phase along the axis of observation.

As shown in figure 2.1(a) the basic out-of-plane ESPI system makes use of the intensity registered in a camera (Image plane) by the interference of a speckle field (Reflected light) and a reference beam. Their generation involve several phenomena simultaneously, but just some are presented here to provide an understanding of the optical setup. The speckle field is generated by the light reflected from a test object and collected by a lens with a small aperture. This last, and the size of its aperture determine the speckle size. The average dimensions of a speckle can be calculated [5] from the width of the autocorrelation peak obtained using the second order statistics of speckle patterns and from the autocorrelation function of the intensity in the speckle pattern given by the relation

$$R_I(\Delta x, \Delta y) = \langle I \rangle^2 \left(1 + \left| \frac{\int \int_{-\infty}^{\infty} |A(x_1, y_1)|^2 \exp[(i2\pi/\lambda z)(x_1\Delta x + y_1\Delta y)] dx_1 dy_1}{\int \int_{-\infty}^{\infty} |A(x_1, y_1)|^2 dx_1 dy_1} \right|^2 \right) \quad (2.1)$$

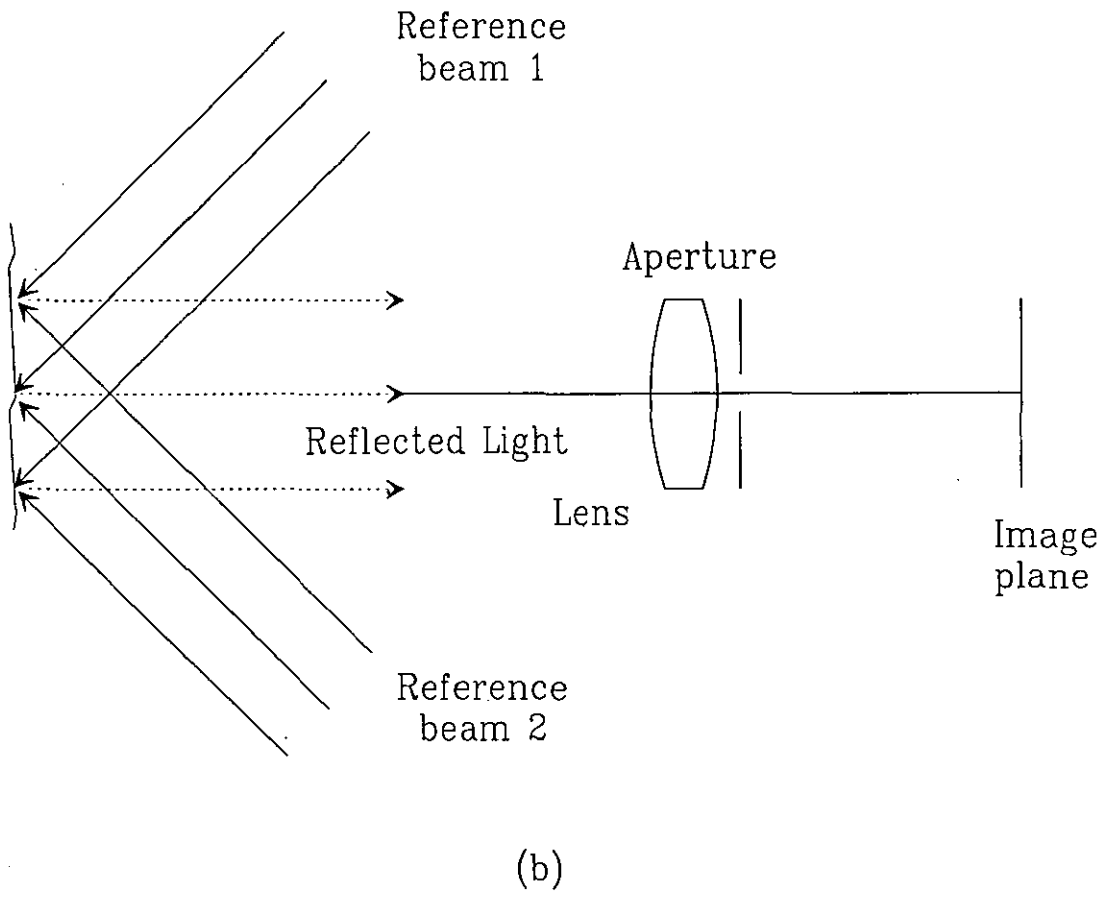
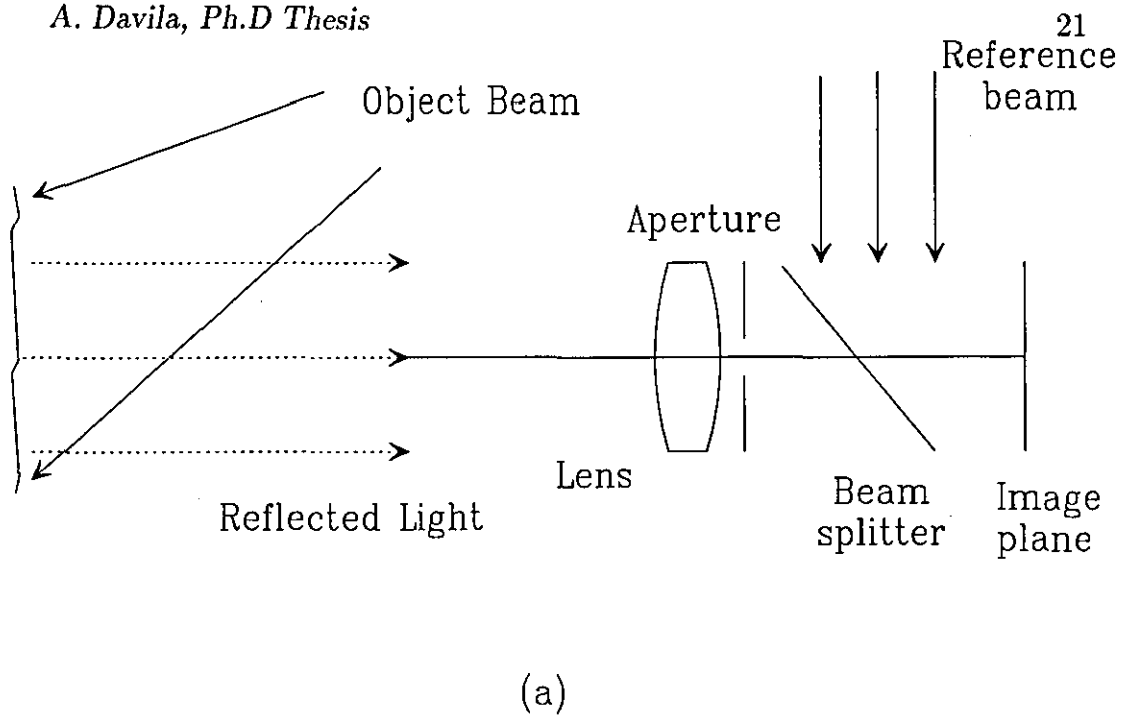


Figure 2.1: Diagram of: (a) Out of plane ESPI, (b) In plane ESPI.

where $A(x_1, y_1)$ and $A(x, y)$ are the complex amplitudes at the scattering plane and the observation plane respectively, related by the Fresnel-Kirchhoff integral. Using Eq. 2.1 is relatively simple to show that in the image plane, the average speckle size is given by

$$\sigma_0 = 1.21\lambda \frac{f}{2r} \quad (2.2)$$

where λ is the wavelength of light, f is the focal distance and \bar{r} is the radius of the optical system exit pupil.

The reference beam can be conceived in different geometrical arrangements for interference with the object speckle field. Besides, the reference beam can be designed with different intensities or wavefront shapes. This interference is possible only if the light arriving from the object has followed the same optical path as that of the light from the reference beam. Finally, the polarization effects and the changes in optical path due to turbulence are also important.

Once the intensity is registered in the image plane by the camera, it is stored and subtracted with the subsequent frames to finally provide the correlation fringe pattern.

By changing some components or altering the geometry of the optical setup or by changing illumination it is possible to obtain in-plane or shearing interferometers. Figure 2.1(b) shows the in-plane optical setup. Two beams of light at equal angles illuminate the target and produce insensitivity to out of plane components and to components at a perpendicular direction of the plane that contains the illuminating beam.

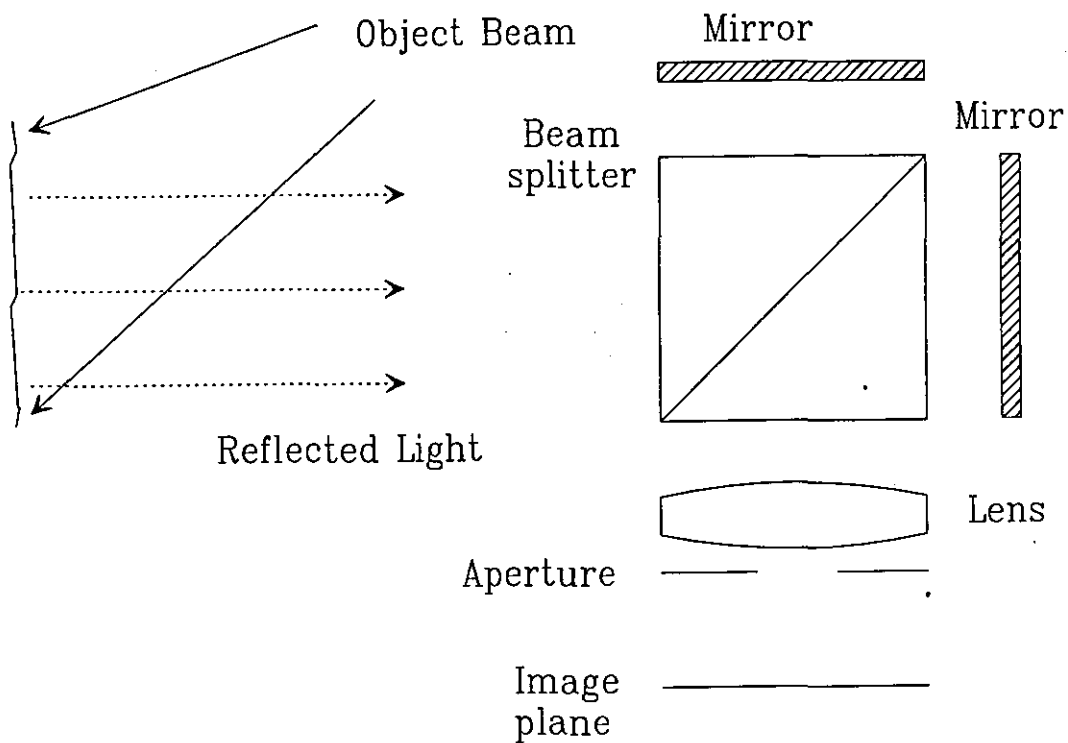


Figure 2.2: Diagram of a shearing ESPI.

The most versatile of the ESPI systems is the shearing interferometer [33]. This arrangement allows the measurements of the derivative of the out-of-plane component along a specific direction. Recently, in-plane capabilities have been also shown for this kind of interferometer [34]. Figure 2.2 shows a typical setup to produce shearing interferograms. The reflected light from the object is collected by a Michelson type interferometer giving as an output two wavefronts shifted with respect to each other along a preferred direction. As the shift is controlled by the tilt of one of the mirrors, displacement sensitivity can be varied over a long range.

2.2 Industrial Applications

At the present time, pulsed ESPI is mainly used as an aid to improved mechanical designs. A promising future for ESPI starts to emerge as optical and electronic components are becoming cheaper and more ESPI applications starts to emerge. However, an important limitation to its development arises from the level of expertise required to operate the devices; a specialized knowledge is necessary to obtain good results in the application of the technique.

The principal application of ESPI in engineering is mainly for measuring static displacement, stress and strain measurements and vibration analysis [6]. The main industries interested in the application of ESPI techniques are the automobile and aircraft industries. However, more industries can make use of these techniques for example, the electronics industry, civil engineering (bridges, dams, etc.). Other applications have been recently demon-

strated in geophysical rock deformation [35], the Ultrasonic design of cutting devices [36] for the food industry, underwater sound transmission [37], inspection of Power plants [38], artwork diagnostics [39] and medical study of bone deformation [40].

2.3 Problems with Current ESPI Devices

There are several technical problems associated with ESPI systems that make them unpopular. A common problem is the user interface that virtually is non-existent, so an expert is always required to deal with the problems of misalignment of the optical components embedded in the system. Friendly interfaces (push button operation) are required and an adequate presentation of displacement data is frequently necessary. It is a common experience to find that engineers do not want to see fringe patterns, in contrast a representation of displacement in a graphical format is widely accepted. Nowadays, some versatile user interfaces have been built to deal with these problems [41], however cost of production is still too high to make this technology more popular. Besides, as no calibration or traceability has been introduced for this systems using international standards, there is still uncertainty about the sensitivity achieved in measuring displacement.

Another technical problem of ESPI techniques is their limited speed in processing and display of displacement data. As a huge amount of data must be processed prior to displacement display, computing time restrains the techniques to lower than real-time speeds. Single point techniques avoid the huge amount of processing involved in a fringe pattern, but the electronic and op-

tics involved will be far from reality if they can be integrated in a single pixel of an image (except for a slow two-dimensional scanning). The main idea of this work is to extend the limits of displacement analysis into a whole field and time resolved integrated solution.

Stability requirement is another important inconvenience in the application of ESPI tests. This limits the techniques in their application to the testing of components over mechanically isolated tables. In a real industrial environment, there is only one alternative to isolate the undesired mechanical disturbances: by observing displacements in specific scales of time. The recent improvement of pulsed lasers has given to ESPI techniques the capability to analyze several scales of time and synchronize them to specific modes of oscillation or to transient events. However, as camera technology has evolved more slowly, the time limit is dictated by the acquisition rate of the camera. To extend the capability of analysis to small scales of time, several existing approaches and a novel one will be discussed later in section 2.7 and section 2.8 respectively.

Two problems of ESPI remain still unsolved: the first is that only a 2-D view of a three-dimensional object is analyzed, so a more complete description of the displacement will require to include all the surfaces of the object in a three-dimensional view. The second is its inability to explore inside materials under test. As light is reflected by the surface of the target, any internal structure can not be detected if no surface effect is caused.

2.4 Noise Reduction Techniques

Speckle noise is one of the principal degradations of the quality of the fringe patterns in ESPI. Correct phase values could be easily obtained if noiseless fringe patterns were produced (or at least similar in quality to HI patterns). However, as a consequence of the statistical nature of the speckle correlation process, noise is always present and its reduction is always necessary.

It has become a standard practice to use noise reduction algorithms from commercial packages of image processing; for instance, smoothing with specific neighbourhood filters, low-pass Fourier filters, normalization, etc. However, these methods have not yet proved to be sufficient for the subsequent phase extraction and unwrapping stages. As a series of computer techniques are used to obtain the final displacement, noise is transmitted through all the stages and degrades the displacement values. A more complete description of the relation between noise and the series of techniques used in ESPI will be presented in the first subsection of this section.

Nowadays the research in noise reduction seems to be distributed into many different disciplines. In the particular case of speckle noise, noise reduction can be achieved easily by the average of different random speckle fields (see subsection 2.4.2). However, when twin pulse ESPI interferograms are obtained in the analysis of transient phenomena the fast correlation process makes it extremely difficult to obtain more than one speckle field ².

²This is the case for transient phenomena analysis, in the case of periodic phenomena a noise reduction method based on the average of multiple different interferograms has been proposed recently [42]

The main studies in speckle noise reduction have been done by researchers in the following areas: Synthetic Aperture Radar [43, 44] ultrasound [45, 46], interferometry [47] and in imaging [48]. A great amount of the literature shows an abundance of articles in the SAR research area. Even though some of this research has been done for reducing speckle in images, some of the principles can be applied to the reduction of noisy fringes. It is the purpose of this work to test the performance of these ideas on ESPI fringes and to show the value of translating these techniques to ESPI applications [49, 50]. However, a detailed analysis of all the existent methods is beyond the scope of this thesis. In fact, only the most relevant methods of those found in the literature were tested [50].

Different methods have been applied to smooth ESPI fringes but have been only partially successful. Neighbourhood averaging using kernels of different sizes and weights has generated substantial interest but suffers the major difficulty of introducing blurring of important structural information in the image [51]. Gabor filters with a constant value for frequency and orientation have been used with some success to smooth only very simple patterns containing parallel equispaced fringes [52]. Noise suppression obtained by means of an adaptive filter developed to restore an ideal cosine distribution through the evaluation of the fringe direction has not proved to be sufficient to smooth ESPI fringes [53]. Methods based on the Fourier transform, such as low-pass filtering [51, 54] or spectral subtraction image-restoration, [15, 55] have proved to be very efficient in reducing speckle noise. However, Fourier methods do not preserve details of the object [50] and this is a severe limitation, as in practice test objects usually contain holes, cracks or shadows, or do not cover the whole image. Several approaches have been developed to

reduce speckle noise in Synthetic Aperture Radar (SAR) images [56, 57, 58]. Even though the basic assumption that speckle noise is multiplicative holds both in SAR and ESPI, it should be pointed out that the correlation process changes the statistical properties of speckle noise [59]. Also, SAR images have a high spatial content while most test objects and ESPI fringes have a low spatial content. Results of the application of SAR noise reduction methods to ESPI fringes were presented in a recent paper [50] where it was demonstrated that they reduce speckle noise while preserving image details.

The following sections start with a discussion of the effects caused by the speckle noise in the ESPI fringe processing methods used to obtain the displacement figures followed by a review of the standard methods for speckle noise reduction,

2.4.1 Noise Consequences in Displacement Measurement

Fringe pattern processing in ESPI techniques can be described as a series of methods linked together to produce phase difference values which represent the desired measurement. Speckle noise frequently persist in each method and can produce undesirable results in the final displacement values. Here, these methods are discussed using a schematic diagram as well as their relation with the noise and/or visibility. Figure 2.3 shows the diagram as a set of linked stages that can be used to describe the overall fringe processing strategy:

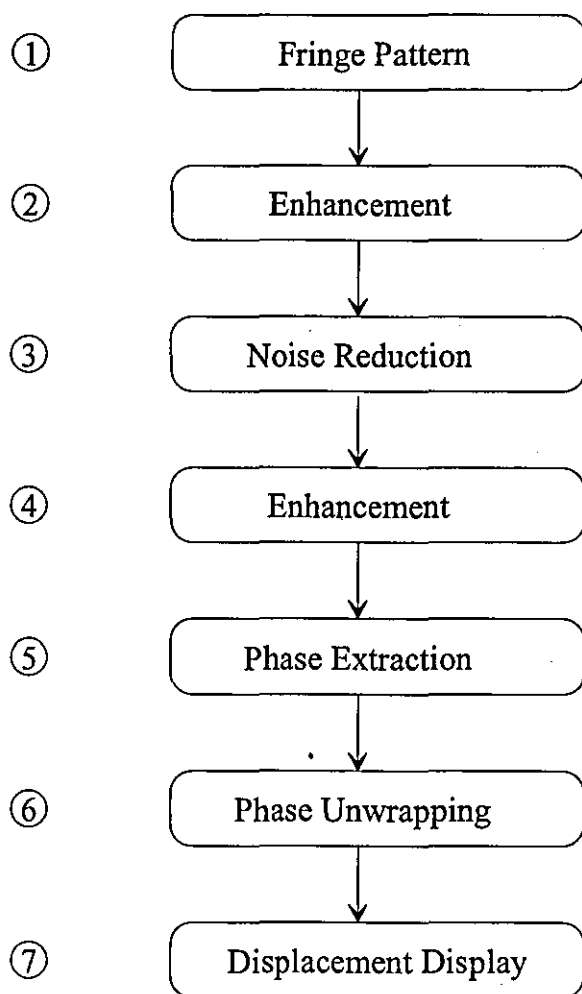


Figure 2.3: Fringe processing methodology.

The first stage of the ESPI process starts with a fringe pattern that is generated by the correlation of two speckle fields. When twin pulse lasers with a short interval of time between pulses are used, addition correlation produces the fringe pattern shown in the first stage. In this case the fringes are difficult to see and an enhancement (2nd stage in diagram) is necessary; this enhancement will be explained in more detail in the following section. On the other hand, if CW lasers are used, the two speckle fields can be stored separately and correlated by subtraction. Then the correlated fringes are of good quality but local shadowings and poor illumination conditions can cause a decrease in the fringe quality. If the speckle fields are stored before correlation, they can also be enhanced prior to correlation. Thus, in any case the second stage is always required.

The need of a third stage arises due to the incomplete correlation process (see section 3.5): instead of evaluating the correlation coefficient definition, a simple operation (absolute value difference, addition, etc.) is applied to the two random intensities obtained from the same position in the two speckle fields. This problem produces the noise that persists in the subsequent stages. As noise is caused by the incomplete correlation, the retrieval of a complete correlation is one of the aims in the search for noise reduction methods.

As some noise reduction methods produce a decrease in the visibility of the processed fringe patterns, a subsequent enhancement is necessary (stage 4). In most cases, a simple normalization of the gray levels scale or an equalization procedure [60] are sufficient for the subsequent stages.

One of the most important steps in the fringe processing methodology is the phase extraction method represented as the stage 5 in the diagram. This

method must be robust to cope with the residual noise left after the noise reduction stage. Some attempts have been made to reduce noise in phase extraction using iterative and phase stepping methods [61]. However, phase stepping is not possible if only a single interferogram is available.

In addition to these stages, the phase jumps that occur in the discontinuities of the phase map produced by the phase extraction methods should be unwrapped. In this context, stage 6 represents any phase unwrapping technique. As noise permeates through the previous stages, special attention has been given to robust unwrapping techniques that can handle this remaining noise [62]. Nowadays, very robust methods are capable of dealing with this noise [63].

Finally stage 7 represents the transformation between phase and displacement. This transformation is usually done using the unwrapped phase and a scale transformation that depends on the wavelength of the light.

As ESPI noise originates from the very nature of the speckle phenomena stage 3 seems indispensable while stages 5 and 6 can incorporate more noise reduction techniques to reduce the remaining noise at the lowest possible levels.

In section 2.6 the phase extraction methods will be reviewed. As will be pointed out in this section, phase extraction methods involve always a filter that is used to reduce noise. As a complement to the phase extraction techniques, a review of one of the most successful techniques for phase unwrapping [63] will be included in section 7.2.

As a requirement for standardization of ESPI techniques, a measure of the noise remaining after all the stages will be proposed in chapter 4.

2.4.2 Standard Techniques

ESPI relies on the fact that if a single wavelength of light is used, the point by point correlation of two consecutive speckle fields can show correlated and uncorrelated regions. The noise produced by the correlated and uncorrelated areas can be reduced by using a similar approach to that occurring in the natural formation of coherent images. In this process, the light reflected from a rough object produces an image that the eye perceives as constituted by speckle noise due to the small aperture of the iris. At least two methods exist to reduce this speckle noise:

- i. using a very large aperture in which case the speckle size becomes very small in comparison with the detector and is hence not resolved.
- ii. reducing the coherence of the source.

In the first method, the detector area integrates a large number of speckles. In the second, noise is reduced by the superposition of a broad range of speckle fields with different wavelengths (reduced temporal coherence) or by a superposition of speckle fields due to a reduction in spatial coherence. Then, it is easy to observe that a reduction in speckle noise can be achieved by superposition of different speckles. In ESPI, the usual correlation procedure is subtraction, so in this case the integration or superposition processes can be done using the subtracted correlated patterns.

As an example of superposition of subtraction correlated patterns, Fig. 2.4(a) and 2.4(b) show consecutively a single ESPI fringe pattern, and the result of adding 25 different speckle patterns correlated previously by subtraction in intensity basis. Previous work by Montgomery [9] has shown the importance of speckle averaging in ESPI applications. It can be shown [59] that speckle contrast (Eq.3.6) is reduced in accordance with the law

$$C = \frac{\sigma_I}{\langle I \rangle} = \frac{1}{\sqrt{N_0}} \quad (2.3)$$

where N_0 is the number of uncorrelated speckle patterns. It can be seen that speckle noise has been strongly reduced. The real disadvantage of this method comes from the inability to get as many speckle patterns as is necessary for the required reduction.

When there is only one speckle pattern, the most often used technique for noise reduction is the low-pass Fourier filter. As will be seen in the next three sections, it has the disadvantage of being a convolution filter in the spatial domain which introduces undesired intensities in the processed patterns.

As the noise present in the speckle patterns is of a non-linear nature, e.g. random behaviour, linear filters such as convolution filters integrate several speckles (equivalent to method *i*) with the additional disadvantage of reducing by consequence the resolution of the image. So the aim of the technique is to preserve resolution while noise is reduced in an efficient way. Next, several techniques for SAR are explored for their ability to reduce noise and in the following section a new algorithm to reduce speckle noise is presented that preserves resolution while noise is reduced.

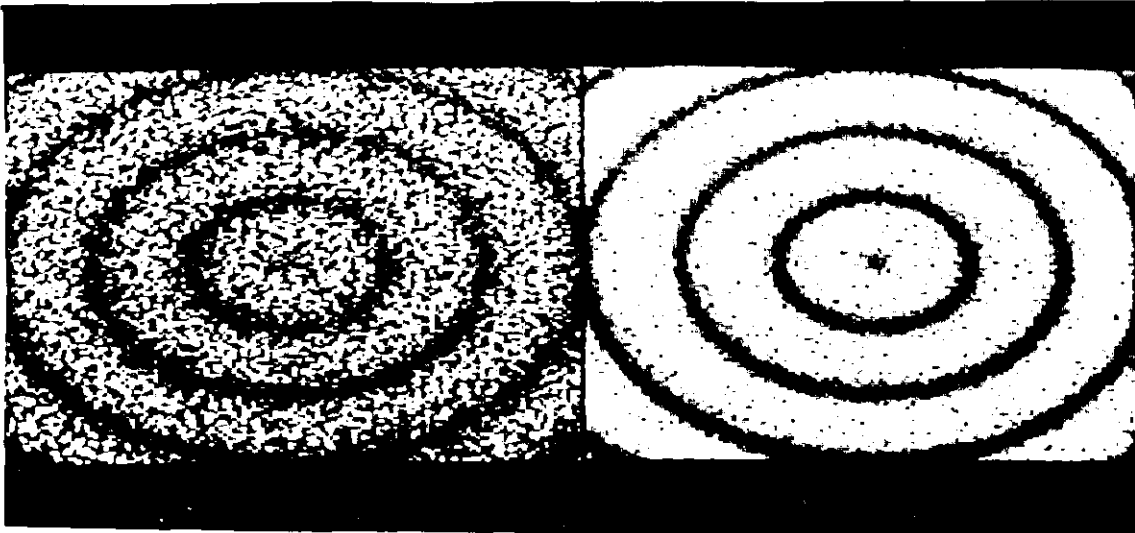


Figure 2.4: (a) Simulated ESPI fringe pattern, (b) Addition of 25 simulated ESPI fringe patterns with different random background using subtraction correlation.

2.5 Enhancement of Addition Fringe Patterns

Enhancement is usually confused with other techniques, the key to distinguish this technique from others is that enhancement does not reduce the content of noise but can improve the fringe quality by other means (e.g. change in contrast or visibility). When used in imaging applications the image appears with the same previous details but a better signal can be seen in regions of low contrast.

In the schematic diagram described in section 2.4.1, the role of enhancement was outlined in the ESPI fringe processing methodology. It was first shown

to be specially needed after aquisition of addition fringes or when shadows or any lack of uniform illumination was present in the ESPI process. Also it is an indispensable step to improve the contrast after the noise reduction methods, specially when a low contrast fringe pattern is produced. The final quality of the phase is then influenced by the subsequent application of enhancement and noise reduction techniques.

Enhancement can be achieved by different techniques [60] and usually it is achieved by normalization or is implicit in the filtering procedures for noise reduction.

A method to enhance addition fringes that is based on zero order removal and a contrast transformation is presented in the following section. This method will be used in experimental ESPI images in chapter 6. Also, in section 6.2 of the same chapter a method previously developed [12] for the enhancement of addition fringes will be reviewed.

2.5.1 Enhancement of Addition fringes by zero order removal

It is very well know that addition fringes present a very low contrast and are difficult to analyze. Previous workers [64, 30, 1] have suggested high-pass filtering and rectification in order to enhance addition fringes. Here, the combination of two techniques: zero order removal, and a grey level re-transformation are used to enhance computer generated addition fringes.

The resulting fringe patterns have a similar appearance to the subtraction ones showing the feasibility of the method.

The zero order removal technique is in essence a high-pass Fourier filter in which only the zero order frequency (DC) of the transformation is multiplied by zero and the remaining frequencies are not modified. The standard high-pass filter has the disadvantage of including frequencies positioned near to the zero order that can represent important fringe information.

In section 4.1.3 the approximate probability density function (histogram) was calculated using the computer model. From this distribution and from the image itself (Fig. 4.4) it is obvious that a constant term (DC) has appeared due to the addition correlation process. So a zero order removal can be the key for a proper enhancement. Figure 2.5 show the image and the histogram for a zero order removal of the addition fringes of image 4.4.

As it can be appreciated, the enhanced image is similar to its subtraction equivalent. However, a comparison of their histograms (figures 2.5(b) and 4.3) show a narrowing of the curve, decreasing the dynamic range of the grey level distribution. In section 6.1 this method will be applied to experimental images and a similar decreasing of the dynamic range will be observed. Also it can be seen that when the speckle size is smaller than the pixel size and several speckles are averaged (see figure 4.2(a)), the addition fringe pattern is not easily seen and the enhanced results can be very poor or null. So a desirable condition for the enhancement of addition fringes by zero order removal is that the speckle size must be greater than the pixel size. Another desirable condition is to maintain constant the intensity ratio between refer-

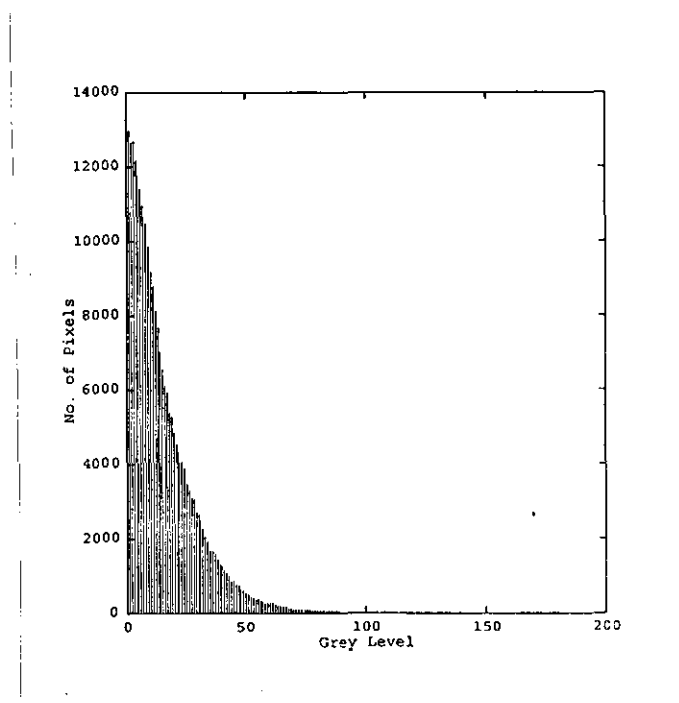


Figure 2.5: Zero order removal of addition fringes from an out of plane simulated ESPI: (a) Enhanced addition fringe pattern, (b) Histogram.

ence an object beam as far as possible, thus a very clean reference beam is needed.

2.6 Phase Extraction Methods

In this section, a brief revision of phase extraction techniques is presented. The techniques reviewed here are limited to those are applied to the study of transient phenomena using pulsed lasers in ESPI. The first section contains a review of the techniques for temporal phase stepping in which it is assumed that it is possible to perform temporal phase steps in the acquisition of the transient event. As just a single fringe pattern is available in pulsed fringe patterns, the second section includes a review of the Fourier transform method to extract phase from a single interferogram. The main disadvantage of this method is overcome by using the phase extraction technique described in the third subsection of this section.

2.6.1 Phase Stepping

Our particular application of pulsed lasers limit the phase shifting techniques to the so called quasi-heterodyne techniques that were developed from heterodyne techniques [65]. Nowadays there are a large number of ways to calculate the phase values depending of the amount of phase shift required for the phase steps, the number of steps and the precision required. With certain exceptions [66], almost all the phase shifting techniques assume noiseless fringe patterns as the starting data for processing.

<i>Phase Equal to Arctangent of</i>	<i>S</i>	<i>F</i>	<i>Phase Shifts</i>
$\frac{1+\sin(\gamma)}{1-\cos(\gamma)}$	1	2	$\frac{\pi}{2}$
$\sqrt{3} \frac{I_{\pi/4} - I_{5\pi/4}}{2I_{3\pi/4} - I_{\pi/4} - I_{5\pi/4}}$	2	3	$\frac{\pi}{4}, \frac{3\pi}{4}, \frac{5\pi}{4}$
$\tan\left(\frac{\gamma}{2}\right) \frac{(I_{-3\gamma/2} - I_{+3\gamma/2}) + (I_{-\gamma/2} - I_{+\gamma/2})}{(I_{-\gamma/2} + I_{+\gamma/2}) - (I_{3\gamma/2} + I_{+3\gamma/2})}$	3	4	$\pm \frac{\gamma}{2}, \pm \frac{3\gamma}{2}$
$\frac{I_{3\pi/2} - I_{\pi/2}}{I_0 - I_{\pi}}$	3	4	$0, \frac{\pi}{2}, \pi, \frac{3\pi}{2}$
$\frac{2(I_{-\pi/2} - I_{+\pi/2})}{2I_0 - I_{\pi} - I_{-\pi}}$	4	5	$-\pi, -\frac{\pi}{2}, 0, +\frac{\pi}{2}, +\pi$
$\frac{I_{-3\pi/2} - 3I_{-\pi/2} + 3I_{+\pi/2} - I_{+3\pi/2}}{2(-I_{-\pi} + 2I_0 - I_{\pi})}$	6	7	$-\frac{3\pi}{2}, -\pi, -\frac{\pi}{2}, 0, \frac{\pi}{2}, \pi, +\frac{3\pi}{2}$

Table 2.1: Most common phase stepping techniques, S and F are the number of steps and frames respectively.

Table 2.1 shows in detail the equations for the calculation of phase from the most common techniques for phase stepping [67, 65, 68].

In this table the difference of intensity values are used to calculate the phase. For ESPI an alternative approach is the difference-of-phase method [69] in which two phase maps are first calculated from three speckle fields for each map and then correlated by subtraction. However, the additional processing does not give any real advantage.

All these temporal phase stepping techniques require a number of frames and steps which can consume various time. When gathering the frame a period of equilibrium is needed for the object and possibly some time is spend by the aquisition device (e.g. Camera). More time can be also spend in the phase steps, which are usually performed by moving a mirror controlled by a piezo-electric.

For transient events there is not time in which the object stays at equilibrium, so it is necessary to look at spatial separation of phase information.

In double pulse ESPI a single addition fringe pattern is possible to obtain if the time of acquisition is shorter than the TV camera field rate. The following section present an alternative to the phase extraction using a single fringe pattern. As will be shown the main drawback of this technique can be avoided if a technique described in the subsequent section is used.

2.6.2 Fourier Transform

When the intensity fringe pattern is transformed to the frequency domain, more phase extraction techniques are possible.

The phase distribution of a single ESPI interferogram can be calculated using the Fourier transform method proposed by Kreis [15] for the analysis of holographic interferograms. If a cosinusoidal fringe pattern

$$I(x, y) = a(x, y) + b(x, y) \cos \bar{\alpha}(x, y) \quad (2.4)$$

is re-expressed as

$$I(x, y) = a(x, y) + c(x, y) + c^*(x, y) \quad (2.5)$$

where $c(x, y) = \frac{1}{2} b(x, y) \exp[j \bar{\alpha}(x, y)]$, then it can be shown that the Fourier transform of Eq. 2.5 will have three components in the spatial frequency

domain, the zero frequency peak and two components which carry the phase information of the fringes:

$$I(u, v) = \mathcal{A}(u, v) + \mathcal{C}(u, v) + \mathcal{C}^*(u, v) \quad (2.6)$$

Then by bandpass filtering the amplitude spectrum in the $+u$ and $+v$ half planes, the zero frequency peak $\mathcal{A}(u, v)$ and the negative spatial frequency component $\mathcal{C}^*(u, v)$ are filtered out. As the remaining spectrum $\mathcal{C}(u, v)$ is no longer symmetrical, its inverse Fourier transform yields a real part $Re\{c(x, y)\}$ and an imaginary part $Im\{c(x, y)\}$. Then, the wrapped phase $\phi(x, y)$ between $-\pi$ and $+\pi$ can be calculated pointwise by

$$\phi(x, y) = \arctan \frac{Im\{c(x, y)\}}{Re\{c(x, y)\}} \quad (2.7)$$

After the Fourier inverse transformation two phase distributions are obtained, one for each bandpass filter. As each mask allows positive and negative frequencies to pass in one direction but only positive in the perpendicular one, depending on the fringe pattern there can appear zones where the sign of the phase is inverted.

The loci of sign inversion can be determined interactively by the user by comparing both phase distributions. Unfortunately, some fringe patterns do not show a rectilinear sign inversion as shown in figure 2.6(a)-(c) where the user must choose interactively an irregular curve for the sign inversion. Once the sign of the phase distribution is corrected, the continuous phase can be finally evaluated by using an unwrapping algorithm. However, as no *a priori* knowledge is available for the zone that must be inverted the results



(a)



(b)



(c)

Figure 2.6: (a) Fringe pattern. (b) and (c) Sign inversion after the Fourier transform method applied along the horizontal and vertical directions respectively.

of the unwrapped phase could contain an erroneous sign. Also any automatic analysis is not possible due to the interaction with the user.

2.6.3 Carrier Fringes

A sign corrected phase map can be obtained if a *a priori* knowledge is introduced in the fringe pattern. This knowledge can be expressed as a constant phase change over the whole fringe pattern. The carrier phase method has been extensively used since the Fifties in electronic communications systems [70]. Several names has been associated with this technique as quadrature demodulation (in electronics), spatial synchronous detection (SSD) [71] and space heterodyne demodulation of fringe patterns or direct-measuring interferometry [72].

In order to introduce a constant phase change along a single direction, the optical wavefront must first be interfered with a plane reference wavefront expressed by

$$U_0(x) = \exp^{-i\bar{k}\phi_0 x}, \quad (2.8)$$

where $\bar{k} = 2\pi/\lambda$. Assuming that the original wavefront has a phase $\bar{\phi}(x, y)$ the interference pattern will produce an intensity fringe pattern of the form

$$I(x, y) = \left(\exp^{i\bar{k}\bar{\phi}(x, y)} + \exp^{-i\bar{k}\phi_0 x} \right) \left(\exp^{-i\bar{k}\bar{\phi}(x, y)} + \exp^{i\bar{k}\phi_0 x} \right) \quad (2.9)$$

$$= 2 + \exp^{-i\bar{k}\bar{\phi}(x, y) - i\bar{k}\phi_0 x} + \exp^{i\bar{k}\bar{\phi}(x, y) + i\bar{k}\phi_0 x}. \quad (2.10)$$

This equation gives a set of equispaced fringes along the x direction when $\bar{\phi}(x, y) = 0$. When this interference pattern is analyzed in frequency space it can be seen that two symmetrical phase terms are formed with respect to the zero order with a separation of $2\phi_0$ among them. A direct analogy can be seen from the hologram image formation. In which the process of reconstruction by illuminating with the same reference beam can reproduce the phase of the object and the other associated terms. In a similar way, a multiplication of 2.10 by equation 2.8 will give

$$I(x, y) = 2 \exp^{-ik\phi_0 x} + \exp^{-ik\bar{\phi}(x, y) - i2k\phi_0 x} + \exp^{ik\bar{\phi}(x, y)} \quad (2.11)$$

in which the last term contains the isolated phase term. Then if a low-pass Fourier filter is applied to this equation the two first terms can be eliminated, the remaining term will thus contain only the optical path difference $\bar{\phi}$. Then, the phase difference can be extracted by using the real and imaginary components of the filtered result as

$$\psi = \arctan \left[\frac{\text{Im}(\bar{I}_a(x, y))}{\text{Re}(\bar{I}_a(x, y))} \right] \quad (2.12)$$

where \bar{I}_a is the low-pass filtered version of I .

Figure 2.7(a) shows a simulated out of plane ESPI fringe pattern correlated by subtraction using Eqs. 4.11 and 4.1 in which $\bar{k}\bar{\phi}(x, y) = \Delta\alpha$ was represented as a spherical optical path displacement and $\bar{k}\varphi = \Delta\phi_0$ was such that 21 carrier fringes were displayed along the horizontal direction. Figure 2.7(b) shows the power spectrum of 2.7(a) where the terms of Eq. 2.11

can be identified: The annular structure is the representation of the spherical displacement centered around the carrier frequency. Finally, figure 2.7(c) shows the resulting phase map after using Eq. 2.11, applying a low-pass Fourier filter and calculating Eq. 2.12.

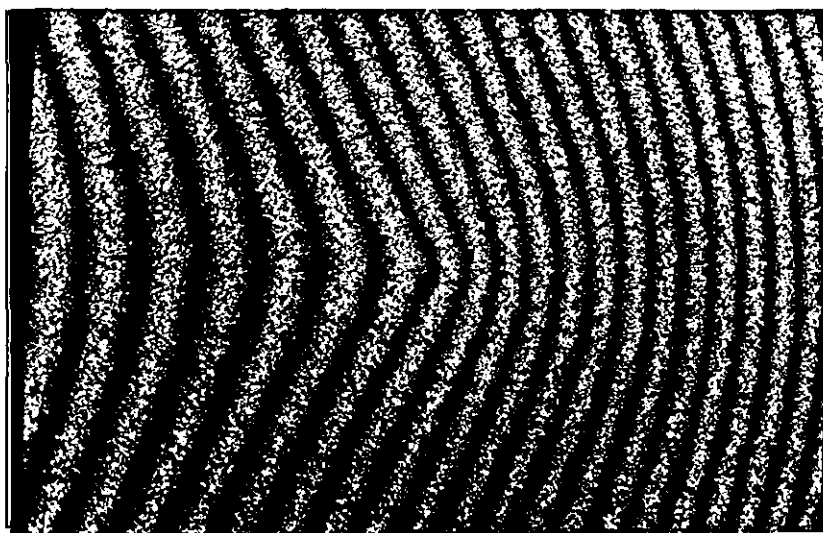
The main advantage of this phase extraction technique is that it can determine the phase map without sign ambiguity from a single fringe pattern. It must be noticed however, that a different sign in the carrier frequency would produce an inversion of the phase values.

2.7 Whole Field Transient Event Detection

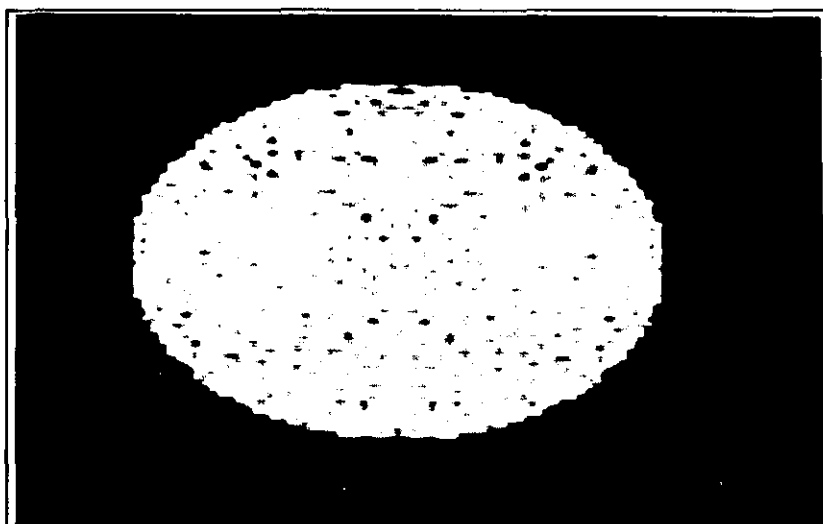
This section presents a review of two optical techniques suitable for out-of-plane ESPI transient event analysis. This techniques will be compared in chapter 8 with the author's solution for whole field transient event detection.

The first subsection reviews an out-of-plane ESPI technique that uses three cameras to grab three phase stepped speckle fields. Even that this technique has been only used for CW applications, it is included here due to its potential as a technique suitable for transient ESPI applications.

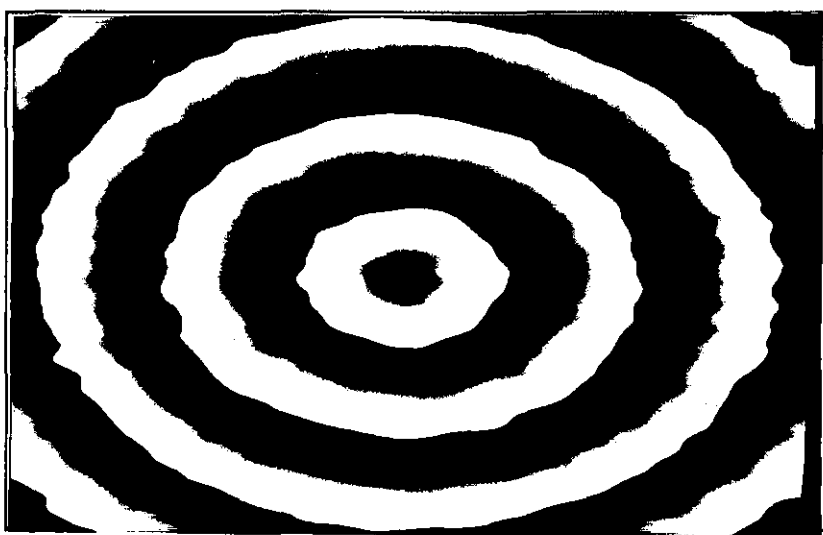
The second subsection reviews an out-of-plane ESPI technique in which the capabilities of an interlaced camera allows the capture of transient events of the order of $100\mu\text{s}$. As ruby lasers were used for this technique, real-time repeatability of double pulses is not possible.



(a)



(b)



(c)

Figure 2.7: (a) Simulated ESPI fringe pattern correlated by subtraction with 21 carrier fringes and a spherical displacement. (b) Power spectrum of the fringe pattern. (c) Phase map obtained from 2.7(a).

2.7.1 Multicamera Phase Stepping

The approach reviewed here is suitable for studying dynamic processes in real-time by TV holography. Its multi-camera optical configuration enables simultaneous recording of three phase-stepped fringe patterns [73]. This system offers the advantage of being practically insensitive for time-dependent external perturbations. However, the optical setup is more complicated and a special calibration procedure must be used to tune the modulation intensity of one of the cameras to the other two. As a result, the system accuracy is reduced relative to that of a single-camera system.

The optical configuration is presented in figure 2.8. The three phase steps are introduced by the principle of polarization phase-shifting (PPS) [74]. This principle relies in the combination of two circular polarizations by means of a polarizer. Both circular polarizations are generated by transforming two plane perpendicular polarizations by means of a quarter-wave plate. Then, the angle of the combining polarizer (analyzer) determines the phase between the two perpendicular polarizations. Using this principle, the multicamera configuration presents the combination of the mentioned elements in front of three cameras shown in the diagram. The two plane perpendicular polarizations are constituted by the reference beam and the object beam. A plane polarization is selected first from the light reflected by the object using a specially designed combination element. This polarized light is transmitted and combined with a perpendicular light coming from the reference beam. Then these two perpendicular polarizations are made to interfere using the PPS principle.

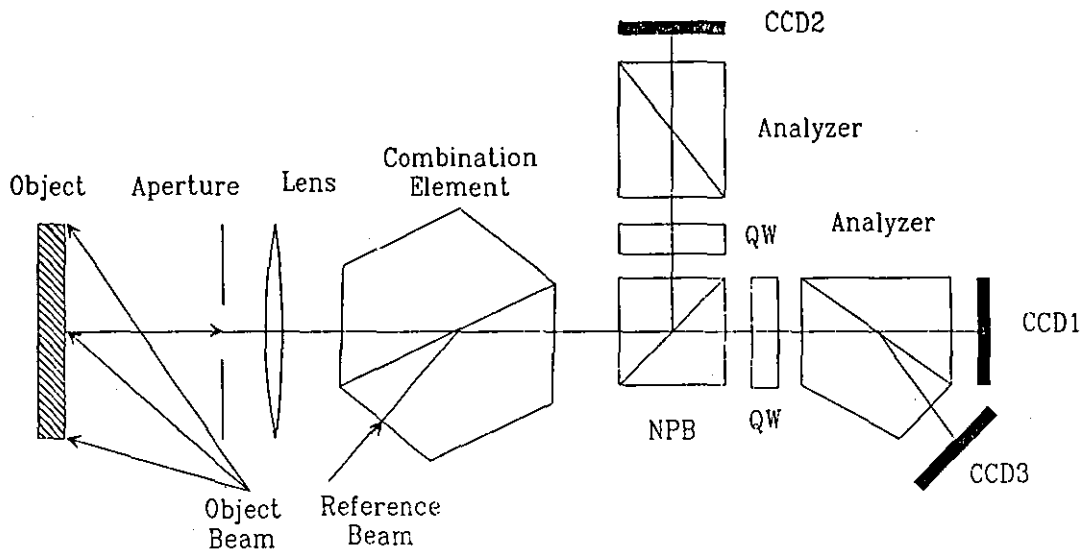


Figure 2.8: Diagram of the multi-camera optical configuration to produce three phase stepped speckle fields.

Although this system is capable to operation at the camera speed, it present serious disadvantages in the alignment of the components, especially of the cameras. The accuracy in the plane of the CCD must be of approximately 1/10 of the speckle size. In the following two sections it will be shown that it is possible to obtain similar phase maps results with a single camera by using spatial phase shifting techniques.

2.7.2 Spatial Phase-Shifting Method

The out-of-plane system reviewed in this section makes use of a tilted reference beam that remains fixed between two consecutive exposures of the double pulsed laser [32, 75]. The phase difference of the reference beam with respect to the object beam suffers a delay in time proportional to the inclination of the reference beam. As this delay is proportional to the projected distance in the image plane, a phase change is recorded spatially in the speckled field.

Figure 2.9 show a schematic diagram of the system in which the angle θ shows the inclination of the reference beam. As this figure shows, the arrangement is the same than the original out-of-plane ESPI (Fig. 2.1(a)) except for the introduced tilt in the reference beam.

As this method relies in the local phase change introduced in the direction of the tilt, decorrelation effects can be obtained between adjacent pixels if a small speckle size is used. To avoid this decorrelation, a speckle size larger than a pixel is used in order to include several adjacent pixels. As this enlargement is needed in a single direction, a rectangular aperture can be

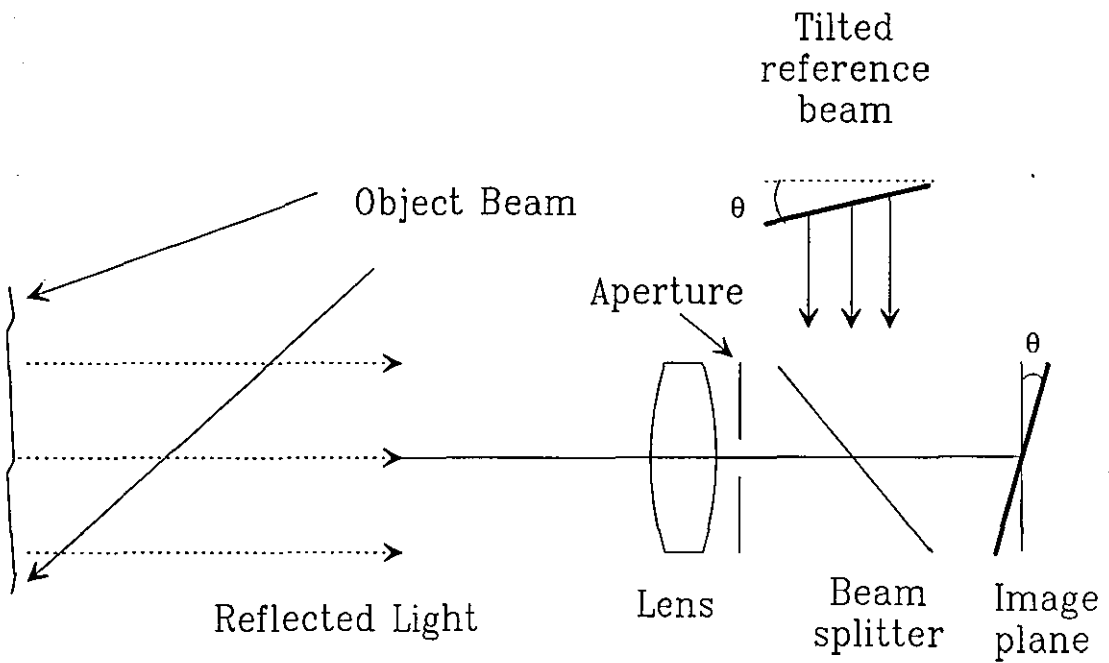


Figure 2.9: Diagram of an out-of-plane ESPI configuration to produce three phase stepped speckle fields by the spatial phase-shifting method.

used to preserve a smaller speckle size in the perpendicular direction of the introduced tilt. A representation of these enlarged speckles sizes is shown in figure 2.10 for circular and rectangular speckles sizes.

In practice it is often necessary to use speckle sizes even larger than the calculated size. This arises due to the fact that an even region with nearly constant correlation is needed by this method. As it is very well known, the autocorrelation function of the intensity fluctuation of two points on a speckle pattern reduces to the Airy disc formula [76]. Then it is easily seen that a larger speckle size is more convenient to preserve correlation. In Section 3.2 it was shown that if a coherent background is interfered with the speckle field a larger speckle size is formed. This is the case of the out-of-plane ESPI so the needed enlargement of the speckle size can be compensated to certain extent.

Then if correlation is preserved in three adjacent pixels, a shift of a speckle field with respect to the other before correlation gives a means to change the previously associated phase (by the reference beam) of each pixel. Consequently, three phase steps can be obtained as

$$\begin{aligned}
 g(i, j)_0 &= | \bar{I}(i, j, \Delta\alpha = 0) - \bar{I}(i, j, \Delta\alpha) | \\
 g(i, j)_{-\pi/2} &= | \bar{I}(i, j - 1, \Delta\alpha = 0) - \bar{I}(i, j, \Delta\alpha) | \\
 g(i, j)_{+\pi/2} &= | \bar{I}(i, j + 1, \Delta\alpha = 0) - \bar{I}(i, j, \Delta\alpha) |
 \end{aligned} \tag{2.13}$$

where \bar{I} is the sampled intensity obtained from

$$\hat{I}_t(i, j) = \| Re^{i\hat{\alpha}j} + \mathcal{F}^{-1} \left(H(u, v) \mathcal{F} \left[e^{i\Delta\alpha} \hat{U}(\hat{n}, \hat{n}) \right] \right) \|^2 \tag{2.14}$$

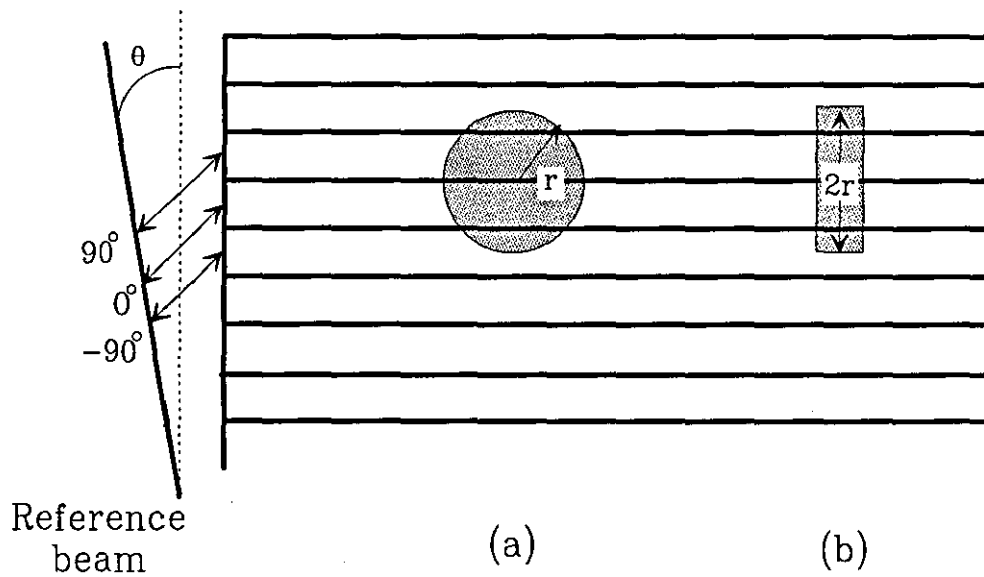


Figure 2.10: Camera representation with (a) approximate circular speckle size, and (b) approximate rectangular speckle size. The shaded speckle areas represent the preservation of a nearly constant correlation.

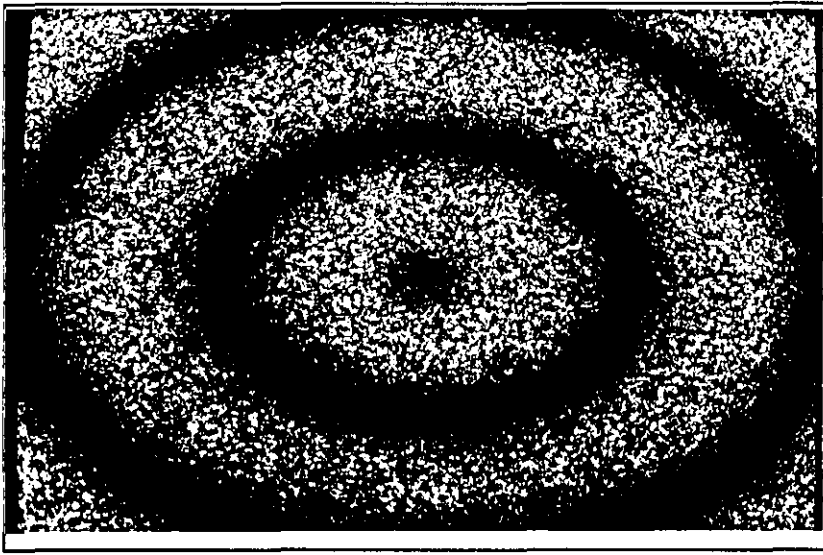
that is again equation 4.1 except that φ has been replaced by $\hat{\alpha}j$ were $\hat{\alpha} = \pi/2$ for 90° phase steeping.

A computer simulation of this process was implemented by the author. to corroborate the experimental results obtained by this spatial phase-shifting method [3]. Figure 2.11(a)-(c) shows the calculated fringe patterns using Eqs. 2.13. It can be seen that figures 2.11(b) and 2.11(c) have lower contrast due to the decreased correlation of the adjacent pixels with respect to the obtained in the central pixel.

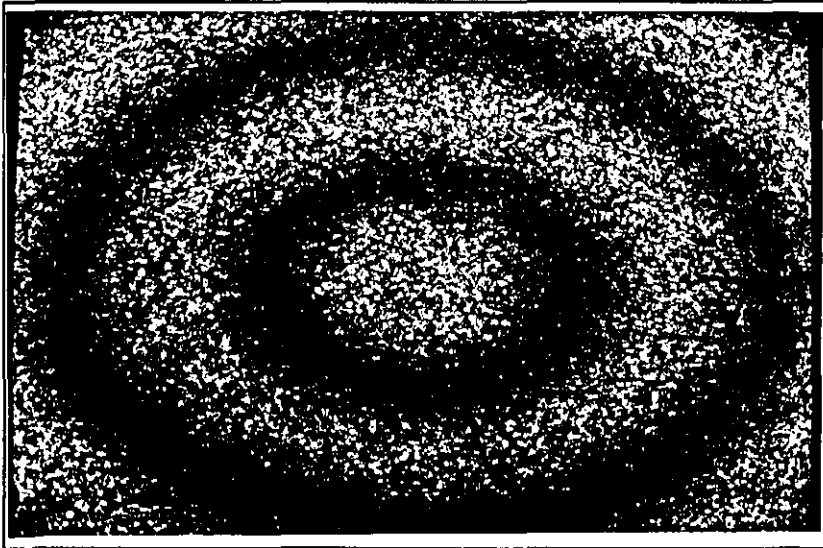
The main limitation of this technique is due to the necessity of two speckles fields. As each speckle field must be stored for posterior processing, the time spend on transferring the speckles fields introduces a time delay. If an interline transfer camera is used, this time delay can be as short as $\approx 5\mu s$, but the electronics associated with this cameras can increase the delay to $30\mu s$ [3]. Despite these limited capabilities, the minimum time delay reported in the experimental results is of $50\mu s$.

Another important limitation is the decrease of light intensity due to the small apertures needed in the generation of larger speckle sizes. This scenario is even worse when interlaced cameras are used. In this case only the charges of the elements of the odd or even lines can be transferred each time. Therefore only half of the vertical resolution is possible [75] and a larger speckle size is necessary decreasing even more the intensity arriving to the CCD camera.

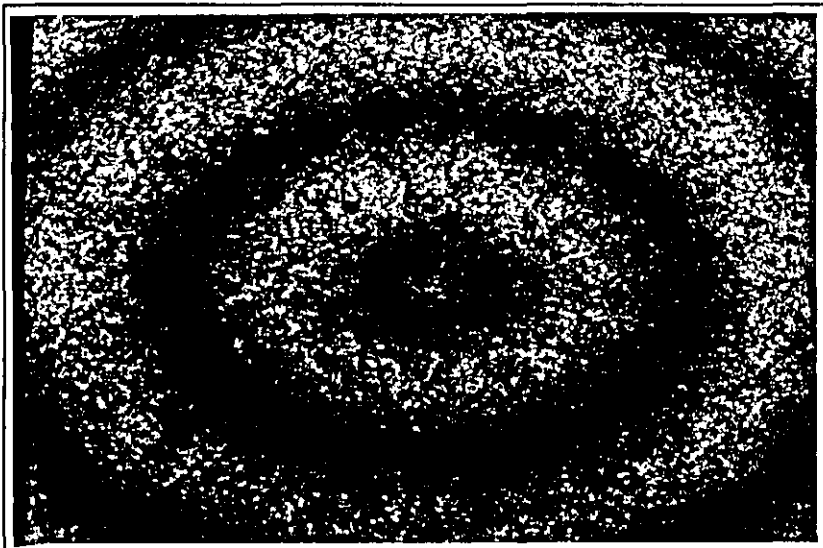
This technique has been only tested using ruby lasers. Thus the associated drawback of non-continous supply of images due to slow recovery time ($\approx 10s$)



(a)



(b)



(c)

Figure 2.11: Three phase stepped fringe patterns obtained by a simulation of the spatial phase-shifting technique with phase steps of: (a) 0, (b) $-\pi/2$ and (c) $\pi/2$.

of the laser mentioned in section 1.2 limits this particular application to lower than real-time speeds. The real-time performance capability obtained by using a Nd:YAG twin pulse laser in this technique still remains to be explored.

Chapter 3

Phase Encoded Displacement Measurement by Speckle Correlation

Light can be used as the vector to carry information about displacement. The fringe pattern observed when two smooth wavefronts interfere, transforms the optical path change (displacement) into a change of the intensity in the resulting fringe patterns. When more than one interfering beam is used the situation is more complex, specially when the speckle phenomena appears. In this case, the changes in optical path transform the speckle field in a complex way; just by local correlation procedures it is possible to obtain a global view of a similar but noisy fringe pattern. Those noisy fringes show also the effects of the displacement generated between them.

The purpose of this section is to provide the basic theory of speckle generation

and to show some particular changes in the probability distribution functions when interference, sampling and correlation processes take place. Knowing the statistical distribution of the noise is helpful for applying suitable noise reduction algorithms [77]. As the first step in this section, the basics of speckle theory are included while the effects of interference, correlation and sampling on the probability density functions (PDFs) are analyzed.

3.1 Speckle Phenomena and Interference

The complicated structure and randomly varying intensity of the speckle pattern has been described first by Newton [78] in 1730 and later (1877) by Exner [79]. From these first observations the phenomenon has been extensively studied and the advent of the laser drew even more attention to its research [80, 76].

Speckle patterns are formed by the multiple interference of coherent (or partially coherent) light that has been scattered by some material media. In most of the surfaces found in engineering structures the irregularities of the surface produce optical path fluctuations larger than the wavelength of the light. When the number of scatterers is very large and no depolarization effects are introduced, the speckle patterns are called normal [81]. The “normal” modifier for speckle will be dropped in the remaining sections of this thesis, so should be assumed implicitly.

A detailed theoretical investigation of the speckle phenomenon can be found

in refs.[82, 83]. So only a brief account of the main points related to the work are given here.

Assuming that the speckle pattern is normal, the proposed model must obey the first order statistics of normal speckle patterns:

- i. The amplitudes, $U(x, y)$ and phases, $\Psi(x, y)$ of the resulting wavefront must be statistically independent of each other.
- ii. The phases, $\Psi(x, y)$ are uniformly distributed in the interval $(-\pi, \pi)$.

From these assumptions a $N \times N$ sampled two dimensional complex object can be represented as

$$\hat{U}(\hat{m}, \hat{n}) = e^{i\Psi(\hat{m}, \hat{n})} \quad (3.1)$$

where \hat{m}, \hat{n} are integers and the amplitude $U(\hat{m}, \hat{n})$ is assumed to be unity. In order to avoid the speckle patterns carrying information on the properties of the diffusing surface, the surface structure should not be resolved with the imaging system (see for example Allen and Jones [84]). To get this effect on a simulation, it is necessary to introduce a Fourier low pass filter to the \hat{U} distribution.

Furthermore, the same low pass filter defines the diameter of the subjective speckle size calculated according to the following formula:

$$\hat{\sigma}_0 \approx \frac{N}{r} \quad r < \frac{N}{2} \quad (3.2)$$

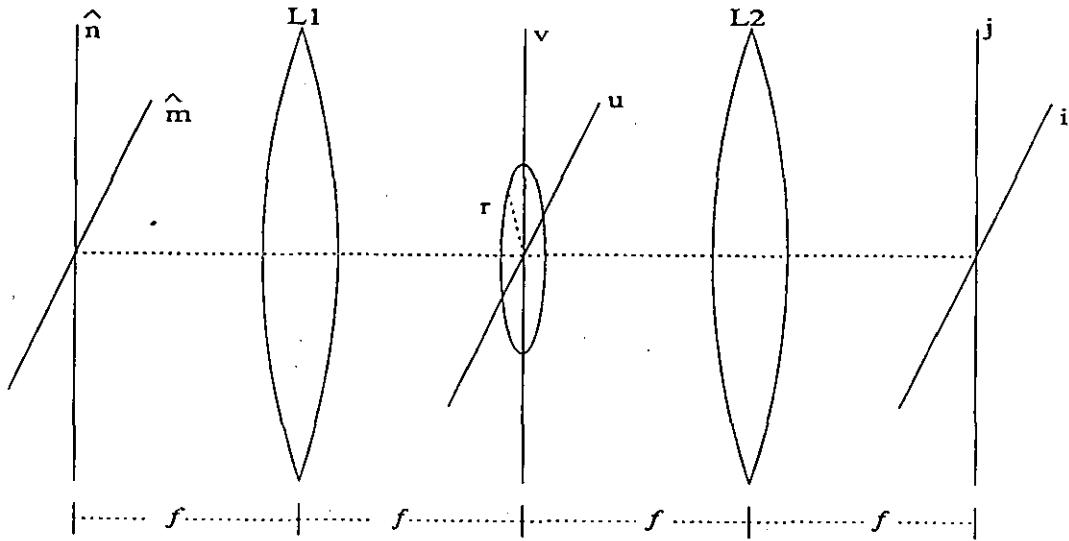


Figure 3.1: An equivalent 4f Fourier optical setup to generate the speckle distribution.

Where N is the number of rows of pixels in a $N \times N$ complex image and $r = (u^2 + v^2)^{1/2}$ is the radius of the circular low pass filter in the (u, v) Fourier plane.

An equivalent optical setup can be devised to accomplish the same mathematical task i.e. the 4f Fourier optical filtering setup, shown in Fig. 3.1 where the coordinate notation can be observed.

In this case the complex intensity is generated at the input plane (\hat{m}, \hat{n}) by means of a random phase screen. Next, the lens L1 produces the Fourier transform at plane (u, v) where a low pass filter of radius r is applied. Finally lens L2 produces the direct Fourier transformation and gives at plane (i, j) the resultant speckle pattern.

In this approach the intensity of the simulated speckle pattern can be obtained by the following expression:

$$I(i, j) = \|\mathcal{F}^{-1} (H(u, v)\mathcal{F} [\hat{U}(\hat{m}, \hat{n})])\|^2 \quad (3.3)$$

where $H(u, v)$ is the low pass filter and \mathcal{F} is the Fourier Transform as usual [85].

The flow chart presented in Fig. 3.2 describes in more detail the necessary steps of a computer algorithm to generate a simulated speckle pattern. In the first stage a $N \times N$ complex matrix is generated. Next, Eq. 3.1 is used to calculate the real and imaginary parts, in this stage a random number generator with uniform distribution must be used to generate the random phases. The resulting values are thus inserted in the real and imaginary parts of the complex matrix. The second stage is used to perform the fast Fourier transform of the matrix. Then, a low pass Fourier filter is applied to the resulting data followed by an inverse Fourier transformation. Finally the intensity distribution is calculated by the square modulus of the resulting complex amplitudes.

Fig. 3.3 Shows the sampled probability density function of the speckle generated image using a Fourier low pass filter of radius 64 pixels for an image of 512x512 pixels, that produces according to Eq.3.2 a speckle size of 8 pixels. Fig. 3.3 also shows the expected negative exponential curve in dotted lines given by [82]

$$p(I) < I > = e^{-I/\langle I \rangle} \quad (3.4)$$

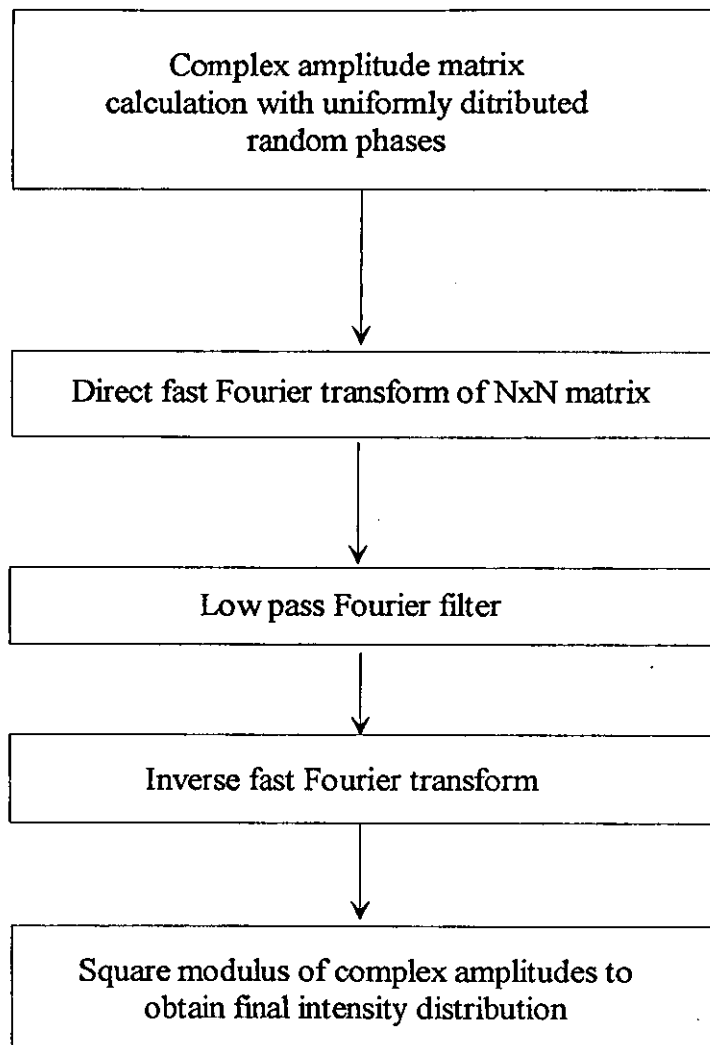


Figure 3.2: Flow chart to describe a computer algorithm to generate speckle patterns.

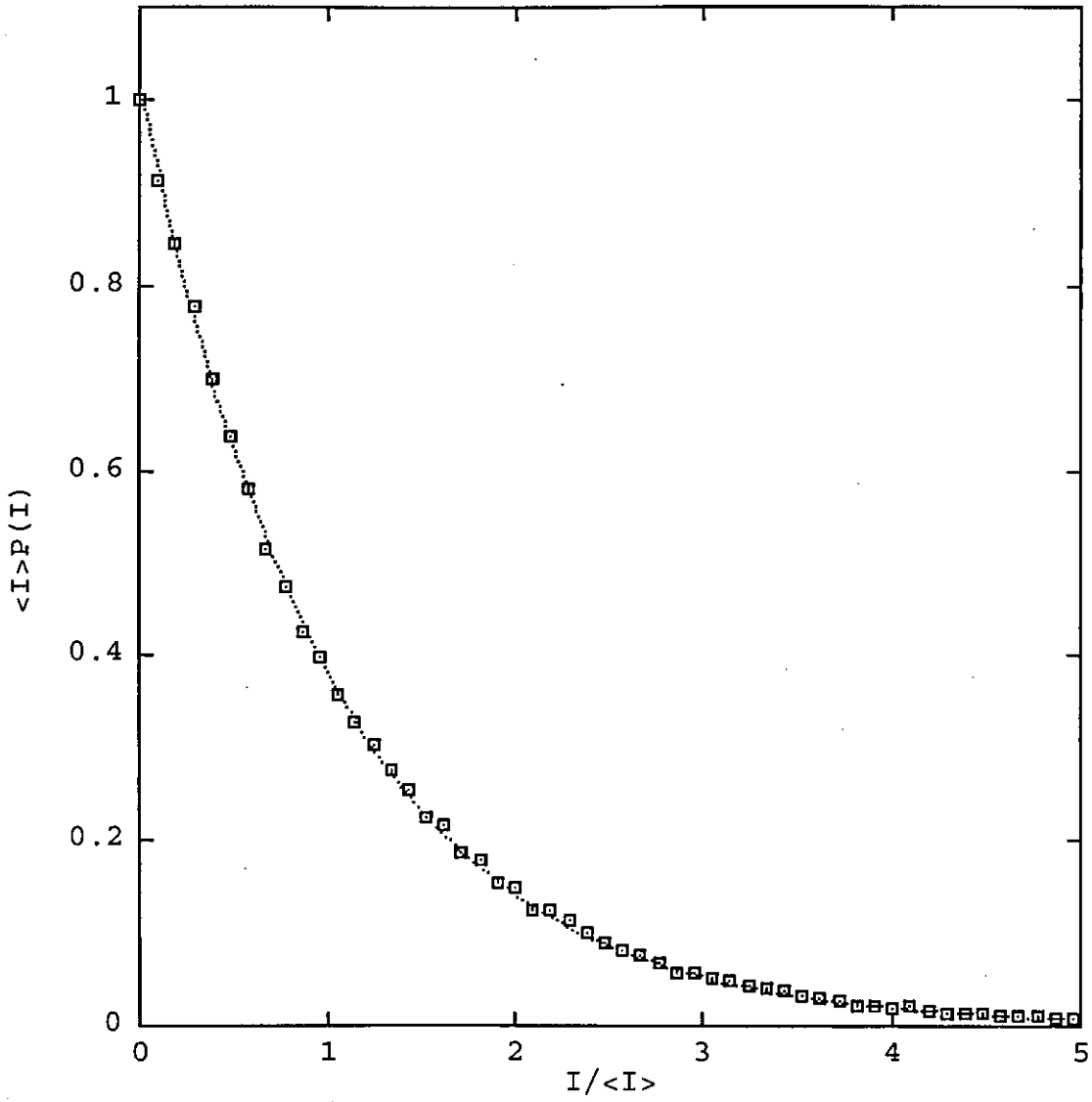


Figure 3.3: Probability density function of the speckle generated image with 512x512 pixels and an average speckle size $\hat{\sigma}_0$ of 8x8 pixels; the dotted curve is the expected negative exponential distribution.

defined for $I > 0$ and $p(I) = 0$ otherwise, where $\langle I \rangle$ is the mean intensity. The moments of this distribution are given by the relation

$$\langle I^n \rangle = n! \langle I \rangle^n, \quad (3.5)$$

from which it is easy to show that

$$\frac{\sigma_I}{\langle I \rangle} = \frac{[\langle I^2 \rangle - \langle I \rangle^2]^{1/2}}{\langle I \rangle} = 1, \quad (3.6)$$

where σ_I is the standard deviation of intensity. The quantity $\sigma / \langle I \rangle$ is called the speckle contrast. This quantity changes due to the correlation and sampling processes that produce the ESPI patterns. This quantity has been used by Crimmins [57] as a measure of the amount of speckle noise present in speckled images. However, its use in fringe patterns will indicate if the noise is reduced, but it does not determine if the processed pattern approaches an ideal fringe pattern. That is why, in section 4.2 better assessments terms will be proposed.

A similar approach for the computer generation of speckle patterns has been published before [86, 87], for double exposure speckle photography and for testing of digital filtering techniques.

3.2 Coherent combination of Speckle and Uniform Fields

In addition to the speckle phenomenon, out of plane ESPI systems combine the speckle field with a uniform reference field. As a consequence, the usual Probability Density Function (PDF) for speckle Eq. 3.4 is modified. The approximate density function using the first-order statistics of the sum of a speckle pattern and a coherent background is given by [88]:

$$p_I(I) < I_N > = \exp\left(-\frac{I + I_s}{< I_N >}\right) I_0\left(2\frac{\sqrt{II_s}}{< I_N >}\right), \quad I \geq 0 \quad (3.7)$$

where $I_0(\dots)$ is a modified Bessel function of the first kind, zero order, $< I_N >$ is the intensity average of the speckle field and I_s is the intensity of the coherent background. In this case the speckle is assumed to be normal and the coherent background is interfering at an angle of zero degrees so that just the real part is considered.

When compared with the speckle observed without an added reference field, the observed speckle size with added reference field increases: the size of the granular structure seems to be larger. Although Ennos [89] attributes this difference as a doubling of the speckle size, an analysis of the power spectrum intensity distribution shows that the real speckle size is composed of two speckles sizes. Figure 3.4 shows this effect where the Fourier transform of an intensity speckle field with an added reference field is presented.

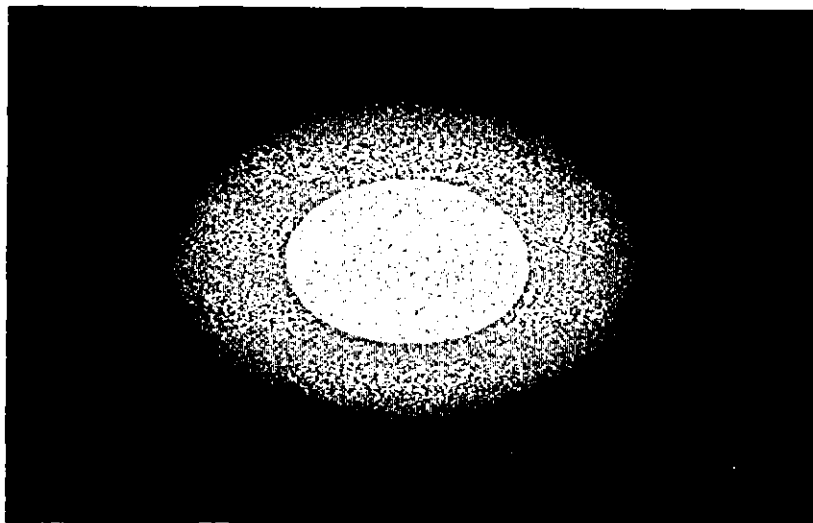


Figure 3.4: Fourier transform of the intensity resulting from the addition of a speckle field plus a reference beam of twice its mean amplitude.

3.3 Coherent combination of Speckle Fields

The addition of speckle patterns on an amplitude basis does not change the statistics of intensity (Eq. 3.4), aside from a scaling constant [90].

In shearing ESPI and in-plane systems a combination between two speckle fields in amplitude is used. Hence, the exponential statistics remain the same aside from a scaling constant.

3.4 Addition of Fields in Intensity Basis

Addition is the usual operation made by the superposition of twin pulses on a CCD camera. If the phase changes between the speckle fields produce com-

pletely different speckle fields, then the resultant PDF of the addition of fields (in intensity basis) is the convolution of their respective PDFs. However, this operation is only valid if the speckle fields are completely uncorrelated. On the other hand if correlation is maximum (e.g. both patterns are identical) the resultant PDF should be the same aside from a scaling constant. In this section the author will assume uncorrelated patterns, for a detailed analysis see [91].

There are several ESPI setups having different PDFs. The simplest case, which is the addition of two exponentially distributed speckle fields, comes from the use of a shearing interferometer. In this case the resultant PDF for the addition in intensity basis can be found using Eq. 3.4 as:

$$p_A(I) = p(I) \odot p(I) \quad (3.8)$$

Performing the indicated convolution, it is easy to show [85] that

$$p_A(I) \langle I \rangle = \frac{I p(I)}{\langle I \rangle} \quad (3.9)$$

When twin pulsed lasers are used with out-of-plane ESPI, the addition correlation patterns are the result of an addition in intensity basis of a speckle field and a reference beam combined in amplitude basis. Neglecting the sampling effect on the PDF the following expression for the resulting PDF can be calculated using Eq. 3.7 as

$$p_B(I) = p_I(I) \odot p_I(I) \quad (3.10)$$

Although no solution has been found in the literature survey for this special case of coherent combination of speckle and uniform fields, the approximated PDF can be calculated using the computational model of section 4.1.

Other authors [89] refer to the combination of speckle fields in intensity basis as “incoherent” combination, however to maintain simplicity this terminology will be discarded in the following work.

3.5 Correlation

ESPI patterns are usually obtained in CW applications by the subtraction of two intensity speckle fields. This operation takes advantage of the variations of local correlation between the intensity fields. The points with highest correlation will appear black due to the subtraction, whereas those with low correlation will exhibit a random variation.

The expression for the correlation coefficient for two random variables I_1 and I_2 is defined as

$$\rho = \frac{\langle I_1 I_2 \rangle - \langle I_1 \rangle \langle I_2 \rangle}{\sigma_{I_1} \sigma_{I_2}} \quad (3.11)$$

where $\sigma_{I_1} = (\langle I_1^2 \rangle - \langle I_1 \rangle^2)^{1/2}$, and $\sigma_{I_2} = (\langle I_2^2 \rangle - \langle I_2 \rangle^2)^{1/2}$. I_1 and I_2 are values of the random intensity inside the speckle size, and a change in phase has occurred between the speckle fields.

The noisy nature of the subtraction of two intensity speckle fields arises on

one hand due to the substitution of the correlation coefficient by a simple operation (absolute value difference, addition etc.), and on the other due to an incomplete correlation: it is not possible to calculate the mean values of the random variables with just a few (two) samples. That is why the most successful noise reduction algorithms use several intensity speckle fields, otherwise the lack of information produces noisy results in the fringe patterns.

According to the experimental results of Pedrini [3] correlation can be preserved locally by an area defined by the speckle size, so a better correlation coefficient can be obtained using more than one random intensity in the speckle area.

It is worth pointing out that correlation is not the only cause of the speckled patterns obtained with ESPI. There is always associated with it a modulation of the correlation due to the object shape and shadows produced by the illuminating beam. However, in the following sections of this chapter we will assume a uniform illumination and a whole field object (ie. frame is filled with no background).

Chapter 4

Fringe Quality Assessment

As a starting point at the beginning of this chapter, a computer simulation of three ESPI systems is included to provide reliable fringe patterns for the quality testing of the processed fringe patterns. In this simulation the errors introduced by the physical ESPI no longer exist. Hence, a detailed analysis of the fringe patterns is possible. Also, some particular changes in the probability distributions functions when interference, sampling and correlation processes take place are analyzed. Knowing the statistical distribution of the noise can be helpful for applying suitable noise reduction algorithms [77].

In order to analyze the reliability of the simulated fringe patterns, section 4.2 presents a new method for fringe pattern quality assessment and a review of the existing techniques for such assessment.

4.1 Simulation of ESPI fringe patterns

ESPI comprises the three main phenomena: interference, sampling and correlation. The interference phenomena can be divided into the random interference generated by the scattering in the object surface and the interference generated by the optical setup. Sampling is performed by the camera detector array, while the correlation process can be obtained by electronic or digital devices. Next, each phenomena is discussed in order to provide the basics of the ESPI computer model.

4.1.1 Interference

ESPI can be made with a large number of optical setups. However, in this subsection a simulation of the out-of-plane, in-plane and shearing correlation interferometers [6] is presented. For the out-of-plane the displacement and the reference beam terms can be easily introduced in Eq. 3.3 to get the intensity of the ESPI as

$$\hat{I}(i, j) = \| R e^{i\varphi} + \mathcal{F}^{-1} \left(H(u, v) \mathcal{F} \left[e^{i\Delta\alpha} \hat{U}(\hat{m}, \hat{n}) \right] \right) \|^2 \quad (4.1)$$

where $\Delta\alpha$ is the phase introduced by the deformation and R and φ are respectively the amplitude and phase of the reference beam.

For the in-plane interferometer the illumination and the in-plane displacement for the \hat{m} direction can be introduced to get

$$\hat{I}(i, j) = \|\mathcal{F}^{-1} \left(H(u, v) \mathcal{F} \left[\left(e^{i\zeta} + e^{-i\zeta} \right) e^{i\Delta\alpha(\hat{m}, \hat{n})} \hat{U}(\hat{m}, \hat{n}) \right] \right)\|^2 \quad (4.2)$$

where $(e^{i\zeta} + e^{-i\zeta})$ represent the symmetrical illumination and $\Delta\alpha$ is the phase change introduced by the in-plane displacement.

Finally for the shearing interferometer the expression is

$$\hat{I}(i, j) = \|S^-(i, j) + S^+(i, j)\|^2 \quad (4.3)$$

where the amplitude fields are

$$S^-(i, j) = \mathcal{F}^{-1} \left(H(u, v) \mathcal{F} \left[e^{i\Delta\alpha(\hat{m} - \hat{m}_0/2, \hat{n})} \hat{U}(\hat{m} - \hat{m}_0/2, \hat{n}) \right] \right) \quad (4.4)$$

and

$$S^+(i, j) = \mathcal{F}^{-1} \left(H(u, v) \mathcal{F} \left[e^{i\Delta\alpha(\hat{m} + \hat{m}_0/2, \hat{n})} \hat{U}(\hat{m} + \hat{m}_0/2, \hat{n}) \right] \right). \quad (4.5)$$

Here the amount of shear introduced between the two speckle fields is expressed by \hat{m}_0 .

The usual approach for expressing the interference pattern of the ESPI [6] is oversimplified and does not take into account the speckle size as well as the sampling effect. These new approaches include both and allow the study of the statistics involved.

4.1.2 Sampling Consequences

The sampling effect can be divided into three cases: (a) When the sampling area (located on the pixel) integrates more than one speckle, (b) when it is approximately equal to the speckle size, and finally (c) when the speckle size is greater than this area. The described theory has been developed for this last case (assuming that the sampling over the speckle size is very large). But in each case the PDF shows complicated changes according to the relation between the speckle size and the sampling area. Here, using the computer model, an analysis of the resulting PDFs for the three cases is presented.

To obtain the simulation, a sampling of the intensity of the fully developed speckle pattern is necessary. This is realized in the same way that a CCD camera performs in practice. The effect of speckle sampling has been studied and characterized, producing a change in the probability density distribution toward the shape of a Gaussian distribution [92].

To obtain a fully resolved speckle will require an infinite number of sampling points inside the speckle size. In this simulation, an approximation was obtained by generating first a 512×512 pixels complex image $\hat{U}(i, j)$ under the assumptions discussed in section 3.1. Next, this was transformed using a 2 dimensional FFT and then filtered with a low-pass filter of radius $r = 64$ pixels and then inverse Fourier transformed. At this stage the reference beam was added with two times ($R = 2$) the mean amplitude of the object beam. The speckle size $\hat{\sigma}_0$ of the object intensity I was of 8 pixels. Previous to the calculation of \hat{I} a reduction in magnification by a factor of 4 was made, obtaining an equivalent speckle size of 2 pixels and an image of size 128×128 .

Fig. 4.1 shows two curves, each representing the probability density distribution of the sampled speckle images for: (a) sampled speckle without reference beam (notice the departure of the exponential behaviour shown in Fig. 3.3 due just to sampling), (b) Sampled speckle with reference beam of two times the amplitude of the mean object amplitude, notice that the reference beam produces a strong departure from the exponential shape approaching a Gaussian shaped curve.

Fig. 4.2 shows the three cases of sampling a speckle distribution plus a coherent background: (a) speckle size less than the pixel area, (b) speckle size approximately equal to the pixel area, and (c) speckle size greater than the pixel area.

The shape of the PDF will determine the *a priori* knowledge for the design of any noise reduction scheme. As the next section will show, this knowledge can also be modified by the kind of correlation between the two speckle fields.

4.1.3 Correlation

The subtraction operation is usually substituted by the absolute value difference and thus better quality in fringes are obtained. This transformation also gives better visual contrast.

Difference is a convenient way to show the correlation. However, in fast dynamic events the use of twin pulse lasers produces usually an addition of two intensity speckle fields. However, addition correlation gives even more

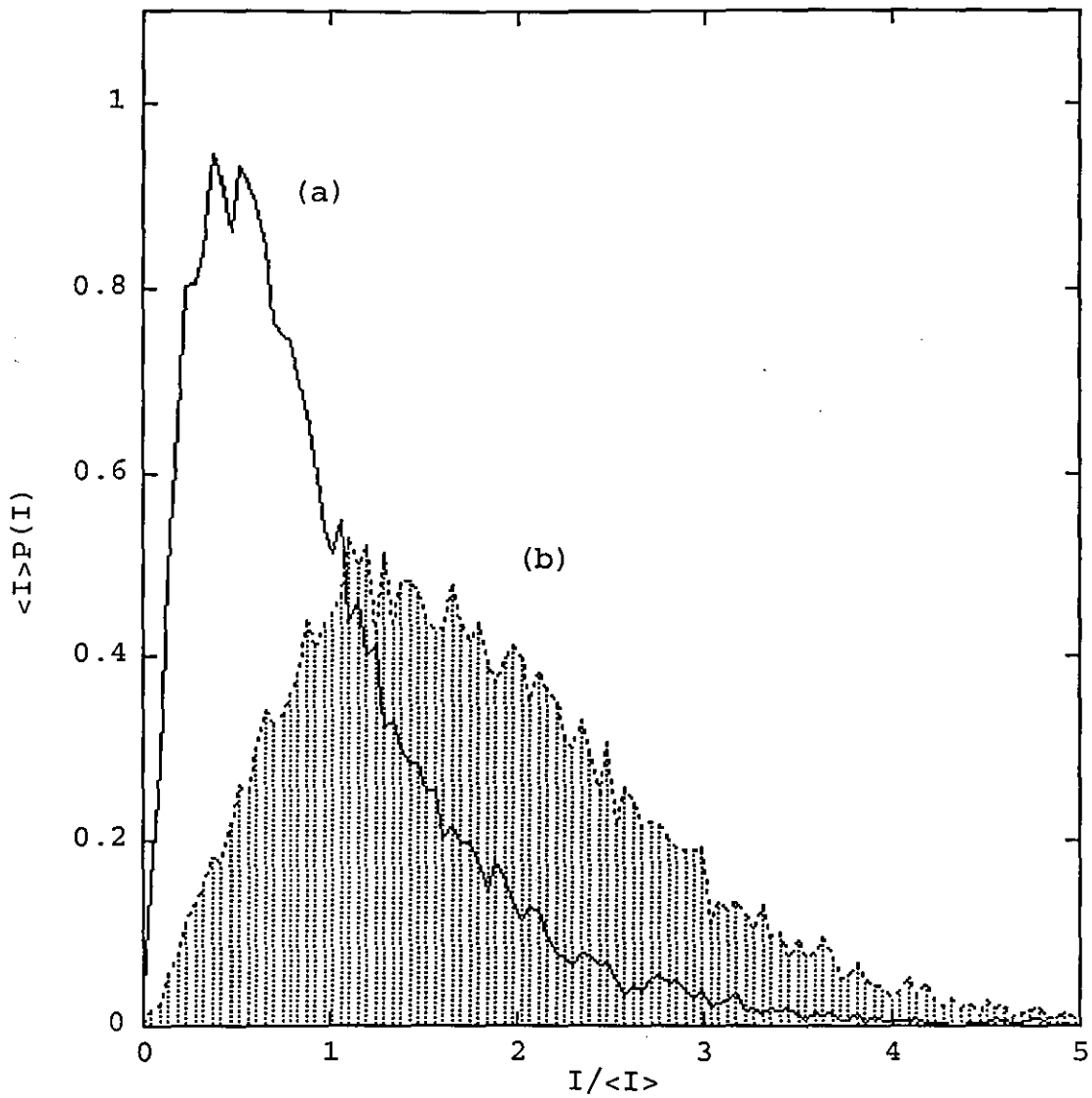


Figure 4.1: Probability density functions of: (a) sampled speckle without reference beam. (b) sampled speckle with reference beam added of two times the mean object amplitude.

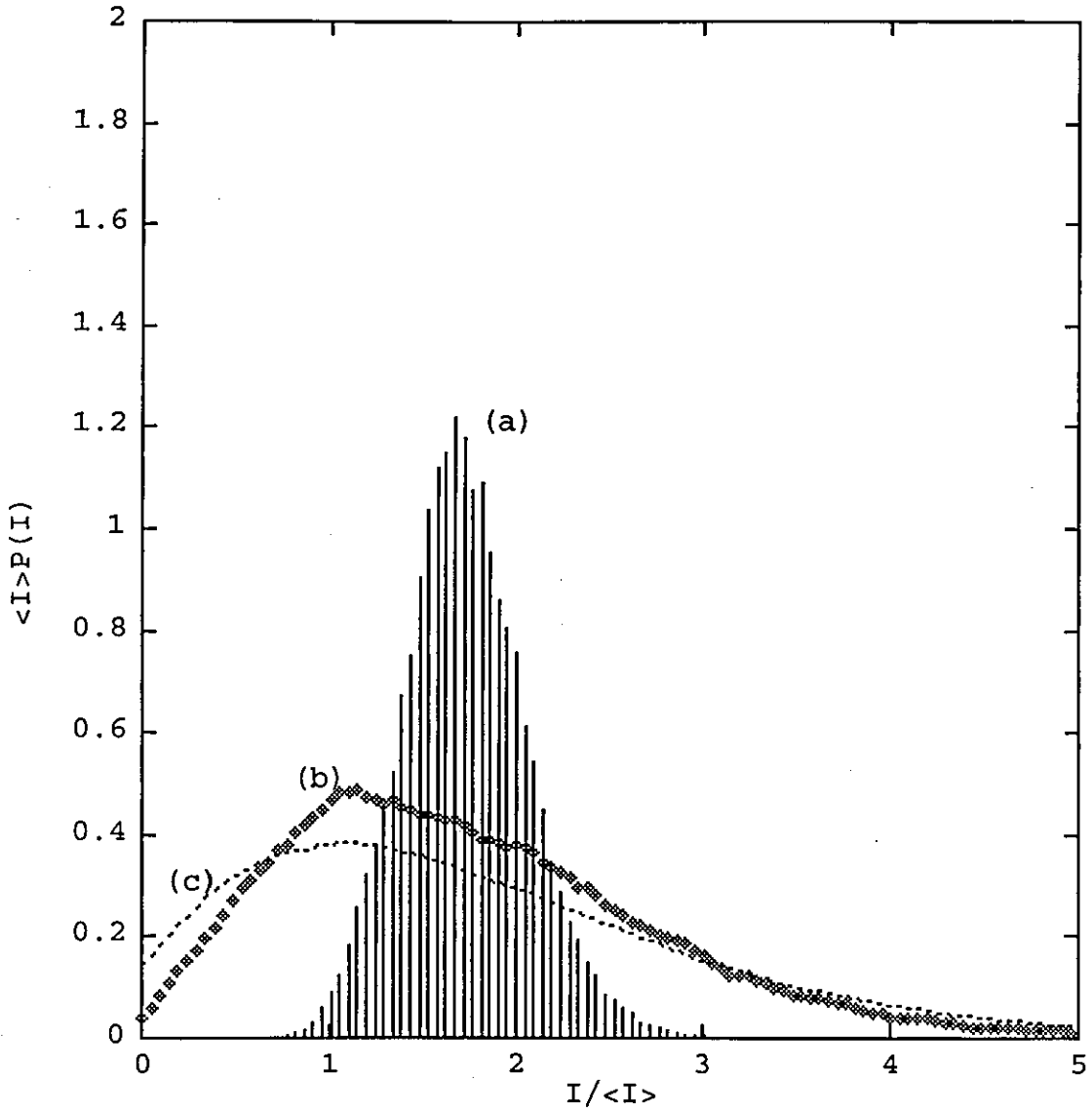


Figure 4.2: Sampling effect on the approximate PDF when the speckle size is: (a) less than the pixel area; (b) approximately equal to the pixel area; and (c) greater than the pixel area.

noisy fringe patterns than subtraction and further processes are needed to enhance the fringes.

Figure 4.3 shows the fringe pattern and histogram of a subtraction of two speckle intensity fields, their PDF is a consequence of the statistics of the speckle intensity fields subject to the subtraction correlation operation. Figure 4.4 shows and addition pattern and its histogram.

4.2 Assessment of Speckle Noise Reduction

Speckle noise removal can be achieved by using various image restoration techniques, in which their common output are smoothed images. In contrast, a clean, undistorted fringe pattern is needed for the subsequent calculation of ESPI phase or displacement measurement. Therefore, a measure of closeness to the clean fringe pattern is extremely important. This measure can be suggested by several formulac. Here, two parameters are proposed for a quantitative evaluation of filter performance: fidelity and speckle index. By using these parameters and the computer generated ESPI fringe patterns, in this thesis a methodology is proposed and used for the evaluation of filter performance in ESPI displacement measurement.

Fidelity parameter -an assessment term previously used in the optical design area- has been proposed by the author as a measure for the closeness of a filtered fringe pattern to its corresponding ideal. Speckle index is a local measure based on the speckle contrast that gives an indication of how effectively the noise has been removed. The observation of the figures obtained

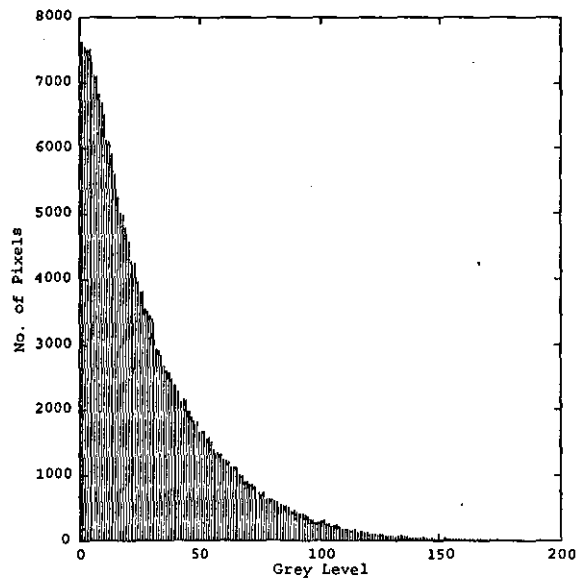
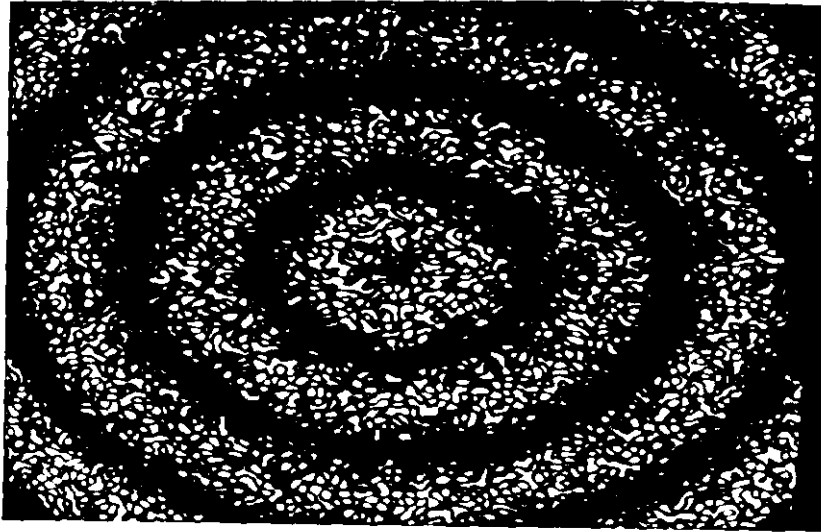


Figure 4.3: Fringe Pattern and its histogram of a subtraction of two intensity speckle fields.

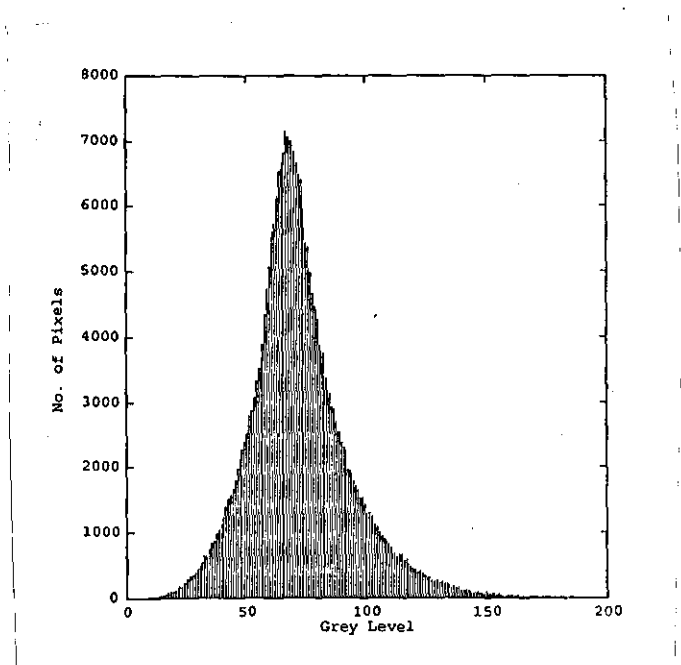


Figure 4.4: Fringe Patterns and its histograms of an Addition of two intensity speckle fields.

from both parameters allows the effective assessment of speckle noise removal techniques.

Assessment methods can give a series of terms to measure the quality of the images. In speckle corrupted images, several measures of the quality of the restoration have been suggested for the case in which the original image is unknown [57, 93]. However, in the case of ESPI computer generated fringes, the fringes without noise can be easily calculated using the phase $\Delta\alpha$ introduced in the displacement by

$$\hat{f}(i, j) = \sin^2\left(\frac{\Delta\alpha}{2}\right) \quad (4.6)$$

Linfoot [94] has suggested several quality parameters for the assessment of optical designs which make use of the uncorrupted image \hat{f} and a corrupted image g :

Image fidelity:

$$\Phi = 1 - \int \int_{-\infty}^{\infty} (f - g)^2 dx dy / \int \int_{-\infty}^{\infty} f^2 dx dy \quad (4.7)$$

Relative structural content:

$$T = \int \int_{-\infty}^{\infty} g^2 dx dy / \int \int_{-\infty}^{\infty} f^2 dx dy \quad (4.8)$$

And

Correlation quality:

$$Q = \int \int_{-\infty}^{\infty} fg dx dy / \int \int_{-\infty}^{\infty} f^2 dx dy \quad (4.9)$$

from where the relation $T + \Phi = 2Q$ can be easily demonstrated.

The author has used the term called image fidelity $\bar{\Phi}$ re-expressed in the discrete case as:

$$\bar{\Phi} = 1 - \frac{\sum_{i=0}^{N-1} \sum_{j=0}^{N-1} (f(i, j) - g(i, j))^2}{\sum_{i=0}^{N-1} \sum_{j=0}^{N-1} f(i, j)^2} \quad (4.10)$$

where \hat{f} and g are respectively the uncorrupted and speckle-corrupted fringe patterns.

This parameter can be used successfully when very similar fringe patterns are compared and any normalization does not introduce significant changes. When noisy fringe patterns are compared against the ideal images a slight adjustment should be made: an equalization of the mean and standard deviation of both images.

For comparison purposes, the ESPI fringes (g) are expressed by

$$g(i, j) = | \bar{I}(i, j, \Delta\alpha = 0) - \bar{I}(i, j, \Delta\alpha) | \quad (4.11)$$

where the bar represents the sampling of the simulated ESPI fringe patterns previously filtered by any noise reduction algorithm.

The comparison becomes complete when the fidelity in the frequency, spatial and phase domains is analyzed. However in this last, the influence of any application of phase unwrapping methods should be taken into account.

To quantify the local smoothness of filtered fringe patterns, a second parameter was used. Speckle noise is usually multiplicative in nature, however

Tur [95] and others have shown this depends on the spatial frequency content of the scene and whether higher frequencies are fully resolved by the optical system. As this speckle noise can be reduced by the addition of multiple correlations (See section 2.4.2), the global average of the local speckle contrast of an image can be a measure of the noise removal. For this reason, a parameter s called Speckle Index was used[57]. This parameter is evaluated as the sum of the ratios of the local standard deviation σ_{ij} to its mean \bar{I}_{ij} for 3x3 windows using

$$s = \frac{1}{N^2} \sum_{i,k=1}^N \frac{\sigma_{ij}}{\bar{I}_{ij}} \quad (4.12)$$

where N denotes the image dimension and

$$\sigma_{ij} = \sum_{k,l=-1}^1 (I_{i-k,j-l} - \bar{I}_{ij})^2 \quad (4.13)$$

$$\bar{I}_{ij} = \frac{1}{9} \sum_{k,l=-1}^1 I_{i-k,j-l} \quad (4.14)$$

The Speckle Index can be regarded as an average reciprocal signal to noise ratio where the signal is the mean value and the noise is the standard deviation. Therefore, a low Speckle Index will be regarded as an indication of local smoothness of the fringe pattern. It should also be remarked that evaluation of the Speckle Index depends on the window size. So, for the assessment of the filter performance and comparison with other techniques, a 3x3 window was used throughout.

Chapter 5

Noise Reduction Techniques

The first section of this chapter presents a discussion of the techniques developed for Synthetic Aperture Radar (SAR). In the second section, a spectral subtraction filter is presented. Section third introduces a novel filter for noise reduction that shows the ability to smooth speckle while preserving dark zones in the fringe patterns. Each implemented technique is assessed by using the computer model previously developed in section 4.1. Finally, the last section presents a brief summary and comparison of the noise reduction methods discussed in this chapter.

5.1 Synthetic Aperture Radar Techniques

The classification of ESPI fringe smoothing methods can be made using their basic global assumptions: multiplicative noise, *a priori* information or using

some kind of local operations: averaging, Fourier filtering, local variance, geometric, adaptive (see [55, 96, 57]) etc. Most of the SAR techniques are implemented using local based operations - see for example [56, 97, 98, 99, 100] - to the author's knowledge only two review articles exist in this area [101, 102].

Speckle noise reduction methods in SAR have been developed assuming a direct analogy between their fundamental processes and the laser-illuminated speckle generation. Speckle noise in ESPI correlation fringe patterns is different to that generated from radar speckle fields due to the intermediate correlation process which changes the statistical properties [103]. Consequently, SAR speckle noise reduction techniques which depend on the image statistics will produce different results if they are applied to ESPI fringe patterns.

The particular statistical properties of ESPI fringe patterns are generated by the correlation of two speckle fields, each one modulated by the imaged, coherent light reflected/scattered off the object surface. Two processes occur simultaneously: those of imaging and correlation. Whilst imaging may be said to carry information about the object shape, correlation produces the fringes (due to surface distortion) which appear superimposed over the object. The resulting fringe pattern is then modulated in visibility by the object's scattering and reflecting properties.

SAR noise reduction methods have been designed to enhance the imaging of remote scenery sensing and are well documented [44, 43]. There are two basic assumptions used in these techniques: (i) that the speckle noise is multiplicative and (ii) that objects have a high spatial frequency content. In

ESPI the first assumption also holds ¹ in most cases while the second can only hold for some special cases, i.e. most engineering objects under test have a low spatial frequency content. Even so, spatial frequencies associated with the fringe pattern can be high, depending on the local gradient of the measurand. The processes that relate both techniques are therefore quite similar and a direct analogy may be drawn between the treatment of noise in SAR and ESPI images.

Among the variety of speckle noise reduction methods which have been developed for SAR, the initial aim has been to explore those easiest to implement; i.e. the adaptive methods and those which use local statistics. For this reason, the preliminary selection for this work included the geometric filter developed by Crimmins [57], the adaptive filter developed by Frost [56] and the sigma filter developed by Lee [100]. A brief review of the basic theory behind these techniques is given next.

The Frost method was developed using a minimum mean square error (MMSE) filter, assuming multiplicative noise. In its design, the filter is adapted using the local mean and standard deviation. The final impulse response is expressed by

$$h(t) = \hat{A}\hat{\beta} \exp(-\hat{\beta}|t|) \quad (5.1)$$

¹The validity of this assumption depends on the spatial details of the object under test. It has been shown [95] that the assumption of multiplicative noise is not valid if the objects contain spatial details which cannot be resolved by the coherent system.

where \hat{A} is a normalizing constant and $\hat{\beta}$ is adapted with respect to the image characteristics and expressed as

$$\hat{\beta} \approx \frac{\sigma_{I_0}}{\bar{I}_t} \quad (5.2)$$

where σ_{I_0} is the local standard deviation defined as

$$\sigma_{I_0} = \sqrt{\bar{I}^2 - (\bar{I})^2} \quad (5.3)$$

and \bar{I}_t is the expected value of the image intensity in a neighbourhood.

To obtain the filter result at location (x_0, y_0) the parameters \bar{I}_t , σ_{I_0} and $\hat{\beta}$ are calculated in a local neighbourhood centred at (x_0, y_0) . Next, they are used to obtain the weighted average of Eq. 5.1 at this location.

The method developed by Lee is based on the sigma probability of a Gaussian distribution. The intensity at the point (x_0, y_0) is considered as the *a priori* mean of the random distribution. Knowing that there is a 95.5% chance that the random samples fall between the two-sigma intensity range $(I_{x_0 y_0} - 2I_{x_0 y_0} \sigma_{I_0}, I_{x_0 y_0} + 2I_{x_0 y_0} \sigma_{I_0})$ of the mean, the following expression for the intensity is calculated in a $(2n + 1) \times (2m + 1)$ window:

$$\hat{I}_{x_0 y_0} = \frac{\sum_{k=x_0-n}^{x_0+n} \sum_{l=y_0-m}^{y_0+m} \delta_{k,l} I_{k,l}}{\sum_{k=x_0-n}^{x_0+n} \sum_{l=y_0-m}^{y_0+m} \delta_{k,l}} \quad (5.4)$$

where δ is one in the two-sigma range and zero otherwise. The spot noise is reduced by a threshold K in the number of pixels within the two sigma

range: if the number of pixels in the two sigma range is less than or equal to K , the four-neighbour average will replace the two-sigma average as the smoothed value of the image intensity.

A different approach to reduce speckle noise has been proposed by Crimmins. The final intensity is calculated by a non-linear combination of the pixels in a neighborhood based on geometric assumptions. A complementary hulling algorithm is used on a binary representation of the image gray levels (the term complementary comes from the fact that the convex hulling algorithm is applied alternately to the gray value profile and to its complement). The whole process can be described in the following algorithm.

- i. A 2-D binary representation of the gray levels located in a column (vertical direction) of the image is made. Here, the gray levels represent a binary graph of zeros over a background of ones.
- ii. An umbra is created in the following way: below the graph all remaining pixels are made zero, otherwise the pixels are one.
- iii. Now one iterative step of the complementary hulling algorithm is applied to the umbra.
- iv. When all the columns are processed, the same procedure is applied to the diagonal and horizontal directions.

This process decreases the narrow peak values while tending to preserve broader details. A more complete description can be found in the original paper [57].

ESPI fringes can be made with a large number of optical setups. Here, the simulation is limited to the out-of-plane displacement sensitive correlation interferometer. A simulated ESPI fringe image (Fig. 5.1(a)) was generated as a set of parallel, straight fringes with varying spacing and visibility along the horizontal and vertical directions, respectively. This image was used as a test vehicle for subsequent comparison of filter performance. The fringe pattern was calculated using Eq. 4.11.

The performance of the SAR noise reduction algorithms described previously, when applied to the computer simulated ESPI fringe pattern shown in Fig. 5.1(a), is summarized in Table 5.1. The performance of a conventional Fourier low-pass filter is also provided for comparison.

The sigma filter developed by Lee was sequentially applied for a 3x3 window and a value $K=1$ was used to remove isolated spot noise. As the processed images still showed some residual spot noise, a median filter with a 3x3 window was applied to the last iterated image. The adaptive filter developed by Frost was applied only once for windows of different sizes. The local statistics were gathered using a window of the same size as that used to perform the weighted average of data.

Several interesting observations emerge from the results in Table 5.1. Firstly, it is seen that the sigma filter developed by Lee gives higher Fidelity (f) values as the number of iterations increases. The Speckle Index (s), which is proportional to the residual speckle noise content of each filtered image, is also reduced when the number of iterations is increased. Fig. 5.1(b) shows the result of applying the Lee algorithm 3 times to the computer simulated ESPI fringes. The image shows that speckle noise has been suppressed sig-

Method	Iterations	Window size	$\bar{\Phi}$	s
Lee	1	3x3	0.77	0.28
Lee	2	3x3	0.81	0.22
Lee	3	3x3	0.82	0.19
Frost	1	3x3	0.75	0.24
Frost	1	7x7	0.74	0.20
Frost	1	15x15	0.64	0.14
Crimmins	1	-	0.63	0.14
Crimmins	2	-	0.65	0.07
Crimmins	3	-	0.65	0.05
Fourier filter	-	-	0.76	0.19
Original image	-	-	1.00	0.52

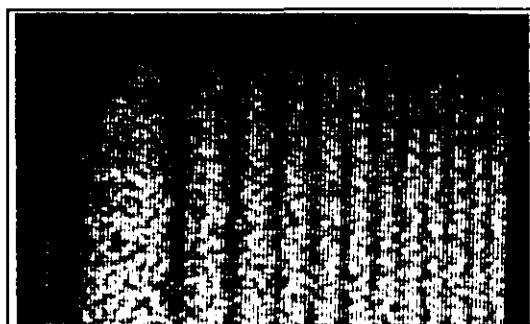
Table 5.1: Results of analysis in the computer simulated fringe pattern.

nificantly while preserving the fringe information. However, some blurring can be observed towards the right-hand side of the image where the fringe frequency increases.

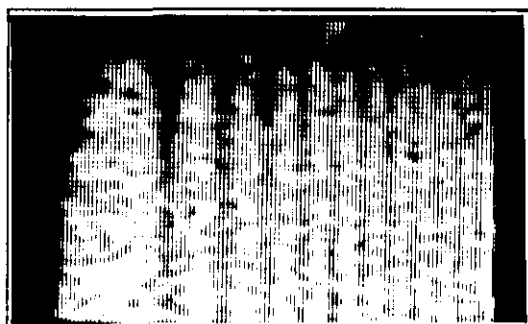
The behaviour of the adaptive filter developed by Frost can also be determined from Table 5.1. It is seen that the residual speckle noise content decreases when the window to perform the weighted average of data increases in size, but the Fidelity shows an opposite behaviour. The filtered image obtained with a 15x15 window is shown in Fig. 5.1(c). Comparing this image with that of Fig. 5.1(b), it is seen that the Frost method provides superior results in terms of noise reduction. However, this method is more sensitive to blurring, especially in areas of low fringe visibility (top) and high spatial frequency (right-hand side).

Another important observation is that the Fidelity and Speckle Index values obtained by the application of both SAR noise reduction algorithms are not significantly different from those determined using low-pass Fourier filtering (Fig. 5.1(e)). However, by comparing Fig. 5.1(e) with Figs. 5.1(b) and 5.1(c) it can be observed that the low-pass Fourier filter produces an image which better preserves areas of low fringe visibility and high spatial frequency.

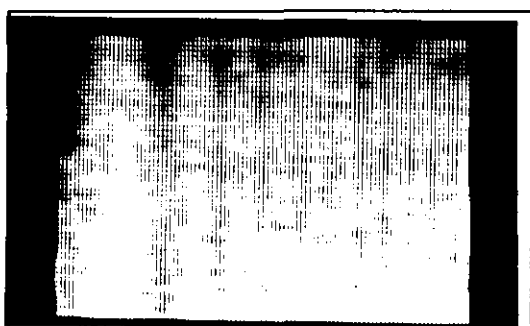
Examination of the figures in Table 5.1 associated with the Crimmins filter show an apparent contradiction: a decrease in Speckle Index and in Fidelity. However, this behaviour can be interpreted as an overwhelming smoothing as is shown in a comparison of the image in Fig. 5.1(d) obtained after the third iteration of the filter with the image in Fig. 5.1(a). High frequency fringes are seen to vanish in the low contrast range (top right corner).



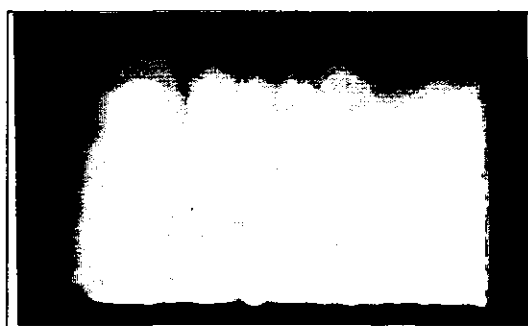
(a)



(b)



(c)



(d)

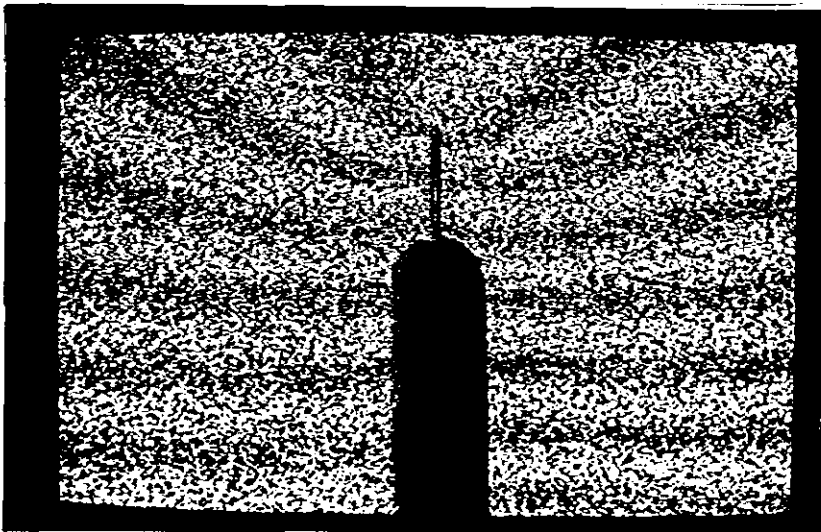


(e)

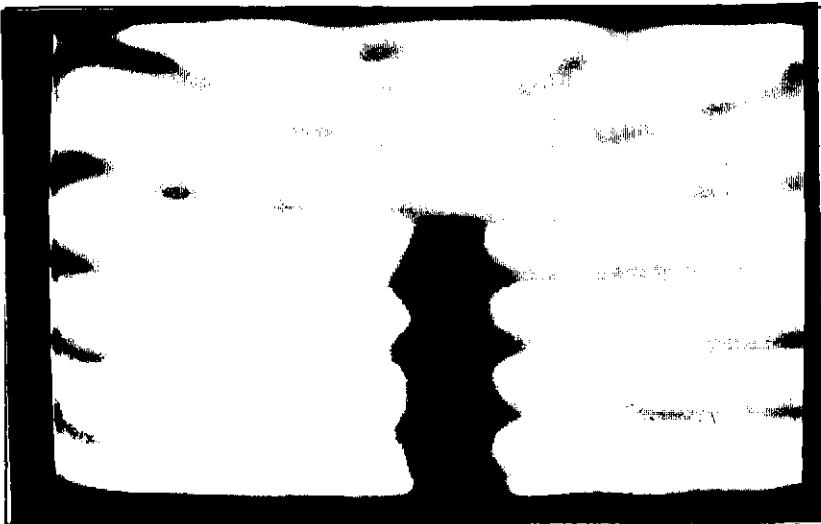
Figure 5.1: (a) Original image, (b) Lee method for 3 iterations, (c) Frost method for a 15x15 window, (d) Crimmins method for 3 iterations, (e) Low-pass Fourier filtering.

Even though the conventional low-pass Fourier filter is still seen as a good noise reduction technique, a completely different situation appears when test objects which contain holes, cracks or shadows, or do not cover the whole image are processed. This result can be illustrated by processing the fringe pattern experimentally generated by a cracked specimen submitted to a tensile load, shown in Fig. 5.2(a). The processed image obtained by means of the low-pass Fourier filter is shown in Fig. 5.2(b). Even though it is seen that the Fourier technique produces an adequate reduction of the speckle noise, it is clearly observed that it does not preserve the image characteristics. The crack has disappeared and the slot becomes smaller in width. Moreover, nonzero data appears over the slot region which will introduce errors when the filtered fringe pattern is used to evaluate the phase distribution. In terms of an engineering application the resulting loss of the crack produces a misleading spatial localization of the object under test: it is important to be able to deduce the spatial relationship between the measurement encoded in the fringe pattern (e.g. strain) to some feature of the specimen (i.e. the propagating crack tip).

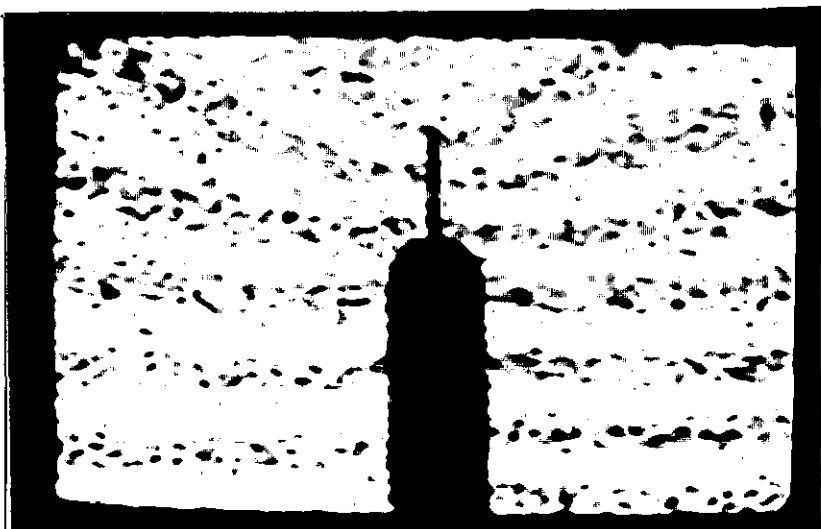
By contrast, Fig. 5.2(c) shows the same image processed with 3 iterations of the Lee filter using a 7×7 window. Here, the structure of the image is well preserved and the localized discontinuities around the crack region may be seen clearly, as may the dark background of the specimen slot. After deducing the phase of the filtered fringes, strain concentrations in the neighbourhood of the crack tip enable quantitative evaluation of the specimen's material characteristics, which would not have been possible using the data of Fig. 5.2(b).



(a)



(b)



(c)

Figure 5.2: (a) Original fringe pattern, (b) Low-pass Fourier filtering, (c) Lee method for 3 iterations with a 7×7 window.

Figure 5.3 shows a detailed description of the Lee method. First, a window of size $(2n + 1) \times (2m + 1)$ is used to collect the pixel intensities in the neighbourhood of a central pixel x_0, y_0 and for calculation of the local standard deviation σ_{I_0} . In the second stage the intensity range is calculated by defining the lower limit as $I_{x_0y_0} - 2I_{x_0y_0}\sigma_{I_0}$ and the upper limit as $I_{x_0y_0} + 2I_{x_0y_0}\sigma_{I_0}$. After this stage a count of pixels and a sum of the intensities that fall within this range is performed. Stage 4 reduces spot noise by replacing the $2\sigma_{I_0}$ range by a four-neighbour average if the count of pixels in the $2\sigma_{I_0}$ range is less or equal to a number K . Stage 5 is used to calculate a $2\sigma_{I_0}$ average (Eq. 5.4) using the summed intensities from stage 3. The whole process must be then calculated for each pixel of the image as represented at stage 6. As this procedure is iterated, in each iteration a stronger smoothing effect is observed. However spot noise might be present after processing, thus a median filter is applied to remove the residual noise.

In practice the Lee method has three main parameters to be adjusted for a particular speckled image: window size, threshold K and number of iterations. The selection of this parameters depend on the speckled input image. For fringe patterns the window size is assumed to be inversely proportional to the fringe density: as more fringes are observed, the window size is reduced and if few fringes are observed, the window size can be increased to obtain a highly smoothed final image. In order to remove the spot noise the parameter K is chosen proportional to the window size. Finally, the number of iterations are increased to obtain a better smoothing effect in the final image.

It should be therefore noted that filtered results shown in figures 5.1 and

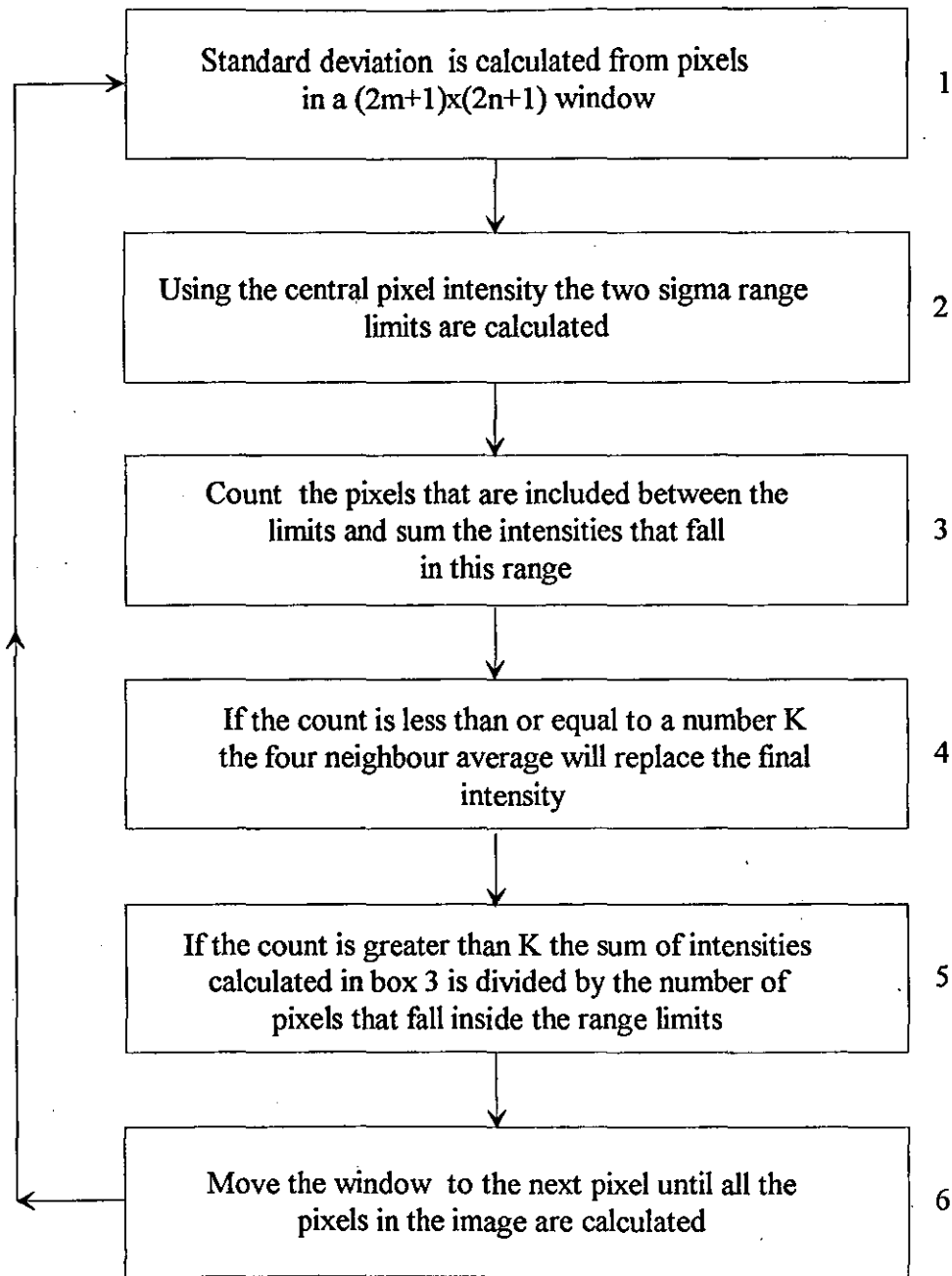


Figure 5.3: Flow chart description of the Lee method of speckle noise reduction

Method	Iterations	Window size	s
Lee	3	7x7	0.07
Fourier filter	-	-	0.07
Crimmins filter	5	-	0.06
Original image	-	-	0.70

Table 5.2: Results of analysis in the experimental fringe pattern.

5.2 have been obtained using filter parameters which are strictly image specific. It is not valid in this case to compare such images with identical filter parameters.

Table 5.2 lists the Speckle Index calculated from the image shown in Fig. 5.2. It may be seen that the Lee method yields a comparable Speckle Index to that of the low-pass Fourier filter. Although the Crimmins filter gives lower values of Speckle Index, this measure is not enough to assess the performance of the filter as shown in the previous figures of Table 5.1. The Frost filter was not included in the experimental test due to its inadequate performance in terms of $\bar{\Phi}$ and s .

Other, more powerful SAR techniques promise good performance in the noise reduction of speckle. In particular if four independent speckle correlated patterns are possible, then the weighted filter described by Martin [104] would be a very good alternative. This filter is based in a modification of the Lee filter in which each pixel within the window is incorporated into a weighted average replacement for the central pixel, each weight chosen according to a local estimation of a Gaussian PDF. In this case, the four independent

patterns can be obtained by the use of the adjacent pixels in the area of the speckle size, while preserving the condition of one speckle per pixel. As this means a decrease in resolution, the acquisition device must have 4 times the number of pixels to compensate the loss in resolution. Another possible alternative is by the use of four cameras to observe the same object, the problem is then that those systems are very sensitive to misalignments.

5.2 Spectral Subtraction Image Restoration

In this section noise is reduced by applying a spectral subtraction image restoration (SSIR) method. Experimental results which illustrate the performance of this approach are presented.

The purpose of this method is to reduce the speckle noise present in the addition fringes using an image restoration filter. The problem of restoring an image degraded by noise has been extensively studied in the literature. One method which has been successful in reducing random additive noise in synthetic aperture radar signals is the spectral subtraction technique developed by Lim [105]. This technique has proved to be effective for enhancing images degraded by computer simulated speckle noise without introducing appreciable blurring [54].

A variation of this technique has been adopted by the author for ESPI. The speckle noise component is given by a speckle field I_2 previous to correlation. Using this new notation the fringe pattern can be represented also after correlation as I_{12} . The estimation of the irradiance $I(x, y)$ of the restored image

is relatively simple and begins by evaluating its discrete Fourier transform $I(u, v)$. This transform is computed by subtracting the power spectrum of the noise component from that of the enhanced addition fringes. For this purpose, the following expression is computed

$$I(u, v) = \left(|\mathcal{F}(I_{12})|^2 - \hat{k} |\mathcal{F}(I_2)|^2 \right) \exp(i\hat{\theta}) \quad (5.5)$$

for $|\mathcal{F}(I_{12})|^2 \geq \hat{k} |\mathcal{F}(I_2)|^2$ and 0 otherwise where $\mathcal{F}(I_{12})$ and $\mathcal{F}(I_2)$ are the discrete Fourier transforms of the enhanced addition fringes and the reference speckle interferogram, respectively, and $\hat{\theta}$ is the phase of $\mathcal{F}(I_{12})$. Constant \hat{k} must be chosen as a compromise between noise reduction and image distortion. Irradiance $I(x, y)$ of the restored fringe pattern is obtained afterward by inverse Fourier transforming Eq. 5.5.

In Speckle-corrupted images, a measure of the quality of any applied restoration has been suggested for the case in which the noise-uncorrupted image is unknown [57]. However, for computer generated images, the image of the fringes without noise can be generated by using the phase introduced in the deformation process. In this case, the quality obtained in the restoration process was measured using the image fidelity parameter (Eq. 4.7) and the speckle pattern correlation fringes without noise have been calculated using Eq. 4.6.

The comparison becomes complete when the fidelity in the frequency and the spatial domains is compared. However, only in the case of straight fringes

is the spatial fidelity a good measure of the performance of the spectral restoration method.

Fig. 5.4 shows several plots of the image fidelity in the spatial domain, against the constant \hat{k} of eq. 5.5 for a pattern with $2m$ correlated fringes where m is an integer. As can be seen from these graphs, the optimal value of \hat{k} to obtain the best result occurs at the first point of inflection of the curve. The second inflection point can occur anywhere, and is due to the convolution of the signal with the noise in the frequency domain.

To test the performance of the SSIR method on curved fringes, the phase of the deformation $\Delta\alpha$ in the x direction was generated according to

$$\Delta\alpha = (C_1\rho^2 + C_2x)2\pi/\lambda \quad (5.6)$$

where C_1 and C_2 are constants, ρ is the radius in the spatial domain and λ the wavelength of the light. Using g as the inverse Fourier transform of Eq. 5.5 and \hat{f} from Eq. 4.6, we can compute the fidelity (Eq. 4.7) in the spatial domain. Using the power spectra of \hat{f} and g , the fidelity can be re-expressed in the frequency domain. Fig. 5.5 shows fidelity against \hat{k} in both domains using a low pass filter of radius $r = 16$ pixels with an image size of 128x128. Notice that the figures of spatial fidelity are good for large values of \hat{k} but that there is a strong decay in the frequency fidelity. Large values of \hat{k} produce straightened approximations to the curved fringes, which is obviously an undesirable effect. Finally, a similar test was made using as the input an image with logarithmically scaled intensity distribution. The

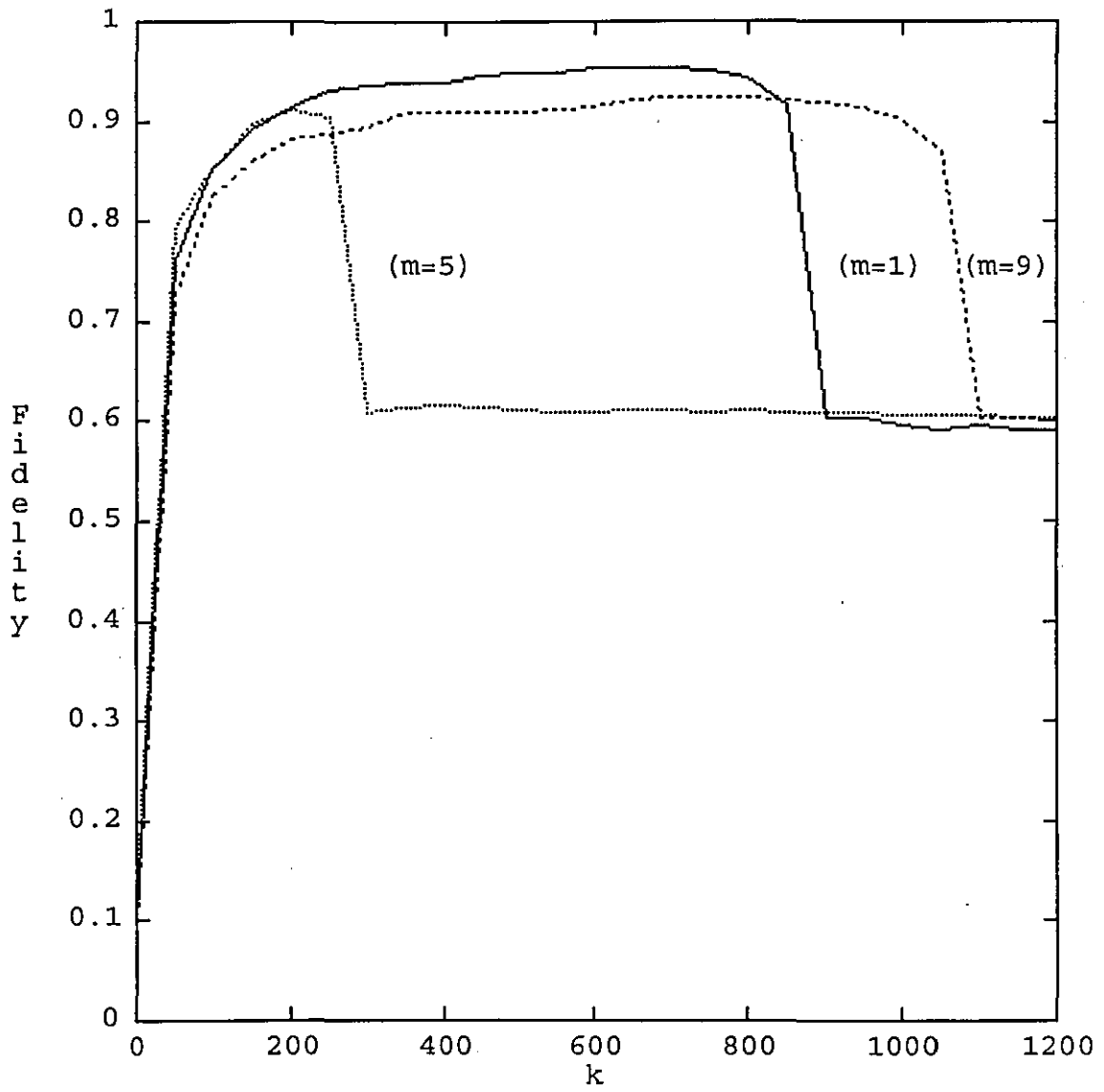


Figure 5.4: Image fidelity against the constant \hat{k} for $2m$ straight fringes.

results show increased fidelity values, with a similar behavior for the fidelity curves of Fig. 5.5 being observed.

The described method was implemented by the author on an image processing system running on a PC-386 computer. This system uses an Imaging Technology Inc. VIPA accelerator board which can perform 32-bit floating-point arithmetic functions on image data much faster than the host computer. For an image of 512 x 512 pixels with a resolution of 256 grey levels, the system can evaluate a Fourier transform in about 3 s.

The experimental addition fringe patterns used to evaluate the method were produced by adding in the image processing system two primary speckle interferograms generated from a standard ESPI interferometer in an in-plane configuration. For each fringe pattern, another two specklegrams were recorded but with no displacement between exposures. The addition of these provided the reference interferogram needed for the contrast enhancement and the noise reduction techniques described previously.

Figure 5.6(a) shows a typical addition fringe pattern obtained for an in-plane rotation. It may be seen that the fringe quality is very poor and a high level of speckle noise is present. Fig. 5.6(b) was produced by subtracting a reference interferogram from the previous one. It is seen that most of the time-invariant noise is removed by the subtraction process, thus giving a very noticeable improvement in fringe visibility.

Figure 5.7(a) shows the high quality smoothed fringe pattern obtained by the application of the SSIR method to the enhanced fringe pattern of Fig. 5.6(b). This last image was obtained using $\hat{k} = 3$, but it was checked that values for \hat{k}

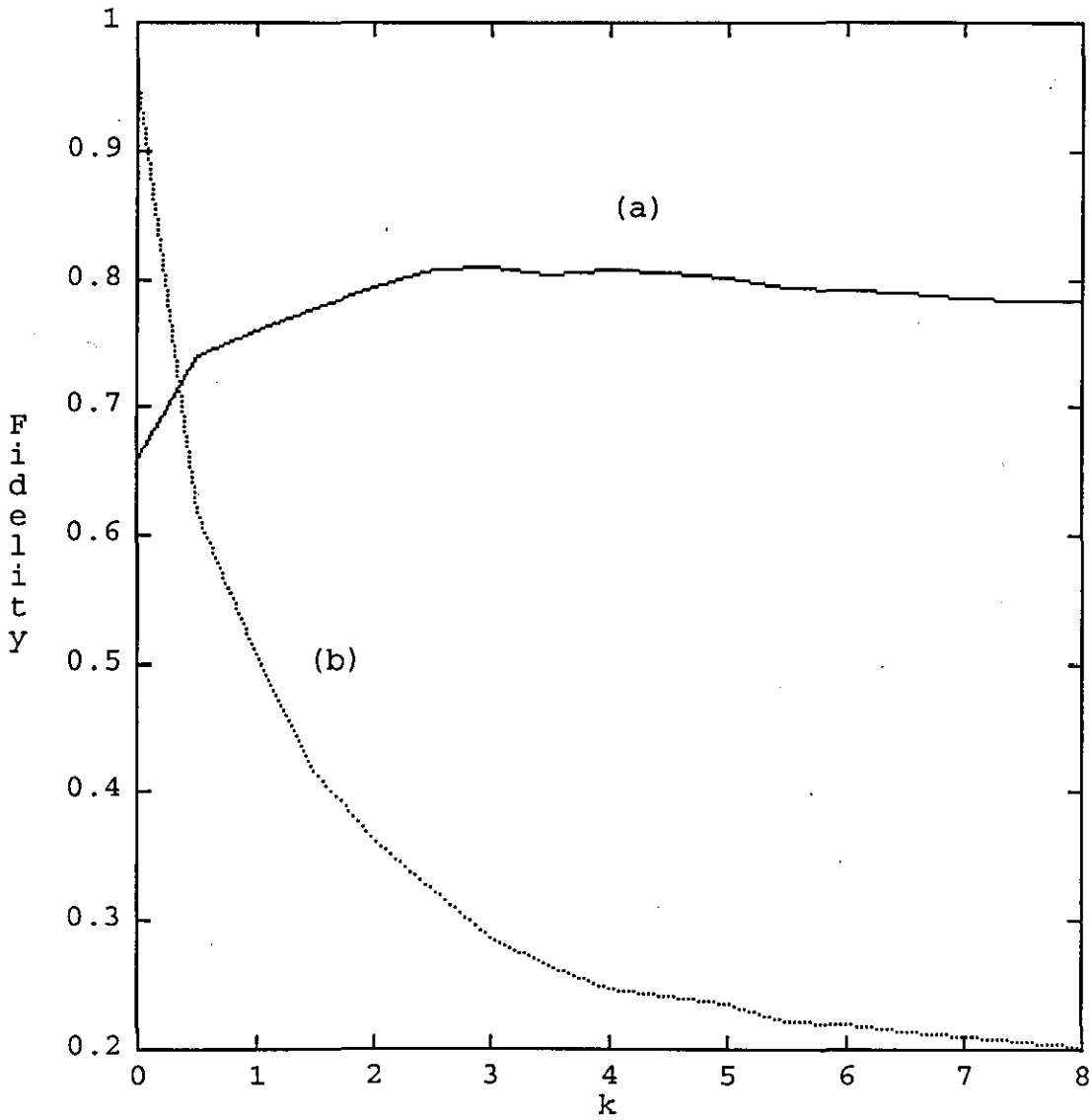


Figure 5.5: Image fidelity against \hat{k} for curved fringes of $C_1 = 0.7$, $C_2 = 3.0$ and $r = 16$ pixels in: (a) the spatial domain, (b) the frequency domain.

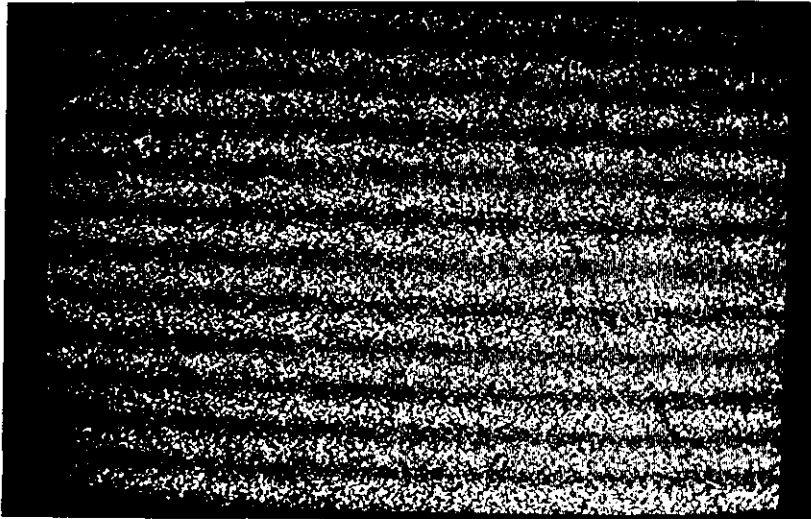
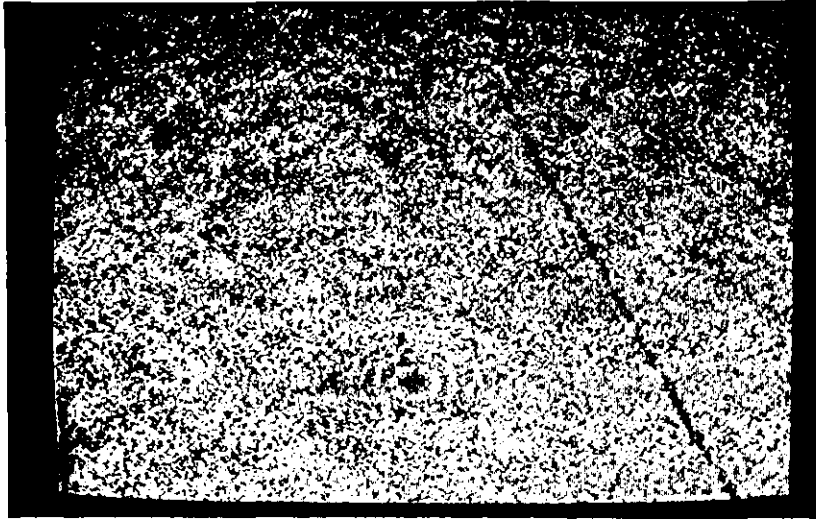


Figure 5.6: (a) ESPI addition fringes generated by adding two interferograms with a in-plane rotation introduced between both exposures; (b) enhanced pattern obtained by subtracting a reference interferogram.

ranging in the interval from 1 to 10 did not give any appreciable difference in the filter performance. For comparison, Fig. 5.7(b) shows the image obtained by low pass Fourier filtering the enhanced fringe pattern of Fig. 5.6(b). Even though the Fourier filter reduces the noise contribution, it also generates a noticeable blur in the fringe pattern which will introduce anomalies in the phase evaluation.

The computer generated fringes provide a method to assess the performance of the noise reduction approach. Computer tests show that fringe restoration using the spectral subtraction method produces for curved fringes decreasing figures of quality whereas for straight fringes the quality figures can be very high.

5.3 Noise Reduction Using a Scale-Space Filter

In this section, the utility of applying a scale-space filter to reduce speckle noise in ESPI fringes is investigated [106]. In general terms, this is a nonlinear clustering filter based on information theory and statistical mechanics which reduces noise while preserving edges. Each filtered pixel is estimated by its neighbouring pixels. The filter has only one parameter which governs the size of the spatial neighbourhood of data on which its output depends. As a result, filtering is carried out in an adaptive and completely unsupervised manner. Using computer generated and experimental ESPI fringe patterns,

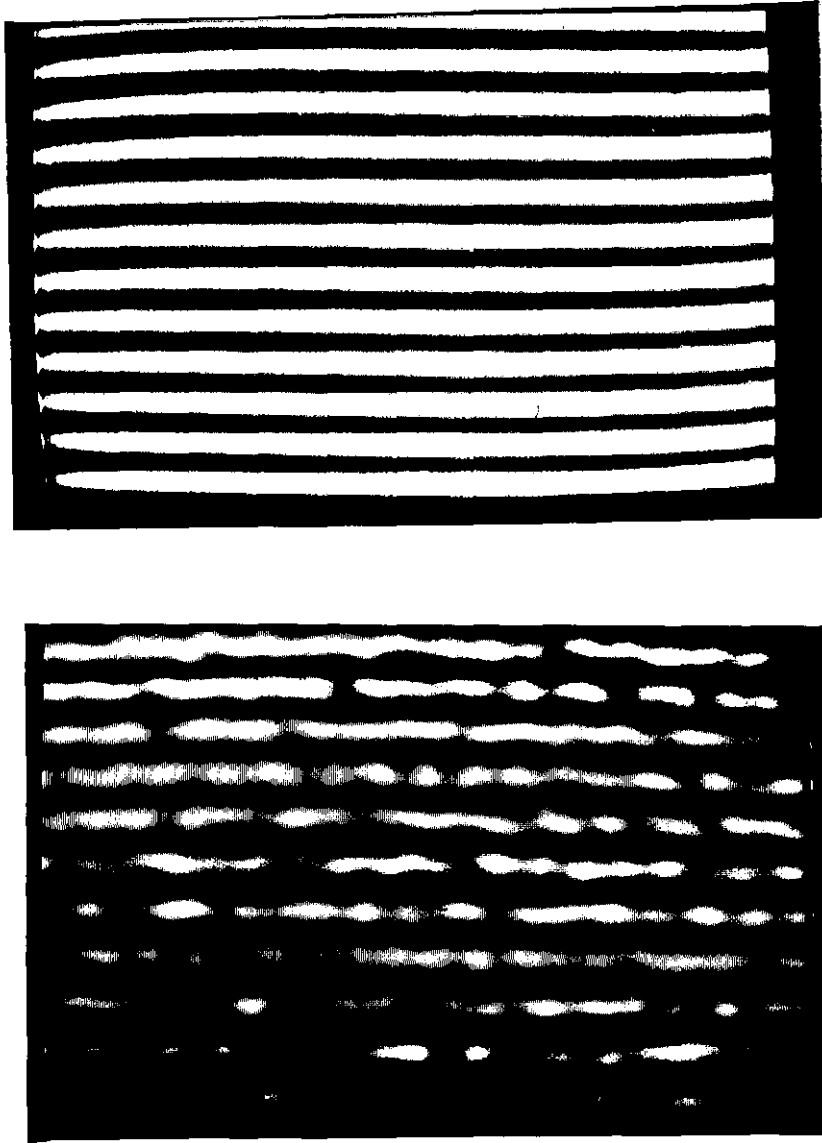


Figure 5.7: Fringe pattern of Fig. 5.6(b) after being processed by: (a) the spectral subtraction image restoration method; (b) Fourier low pass filtering.

it can be shown that the scale-space filter provides better noise suppression than the low-pass Fourier filter while preserving important image details.

A detailed derivation and description of the characteristics of the scale-space filter can be found in the literature [106, 107, 108, 109] therefore only a brief description is given here. To describe the filter first a definition of two parameters is necessary. First, the scale in the input domain is represented by α that is defined to be inversely proportional to the size M of the local window used to estimate the intensity I_{ij} , it is taken as

$$\alpha = 1/2^M \quad (5.7)$$

Secondly, the intensity changes in a local neighbourhood represented by the local variance σ_I^2 defined by

$$\sigma_I^2 = \frac{\sum_{k,l} (I_{kl} - \bar{I})^2 q_{kl}}{\sum_{k,l} q_{kl}} \quad (5.8)$$

where \bar{I} is the average intensity of the pixels which belong to this neighbourhood defined as.

$$\bar{I} = \frac{\sum_{k,l} I_{kl} q_{kl}}{\sum_{k,l} q_{kl}} \quad (5.9)$$

Then the local variance can be used to define

$$\beta = (2\sigma_I^2)^{-1} \quad (5.10)$$

were a small σ_f^2 implies that pixels within the local window have a low noise level producing a large β value.

The noise smoothed intensity I_{ij} of each pixel of the image is calculated using a neighbourhood of $M \times M$ pixels. and to simplify the writing, a limit $W = (M - 1)/2$ is introduced using

$$I_{ij} = \left(\sum_{k,l=-W}^W I_{i-k,j-l} q_{kl} p_{kl} \right) / \sum_{k,l=-W}^W q_{kl} p_{kl} \quad (5.11)$$

where

$$q_{kl} = e^{-\alpha(k^2+l^2)} \quad (5.12)$$

$$p_{kl} = e^{-\beta(I_{kl}-I_{ij})^2} \quad (5.13)$$

The operation of the filter can be explained as follows. From Eq. 5.11, the smoothed value I_{ij} of the central pixel can be interpreted as a cluster centre given the grey levels I_{kl} of pixels within the local window and q_{kl} as the weight given to each I_{kl} . It is also seen from Eq. 5.12 that the parameter α is a measure of scale in the input space, as data near the central pixel should give more information than far pixels. For example, if $\alpha = \infty$, then $q_{kl} = 1$ when $k = i$ and $l = j$, and 0 otherwise. This result implies that every pixel is preserved perfectly. Conversely, a small value of α implies that more neighbours can contribute to the evaluation of I_{ij} . The parameter β

in Eq. 5.13 is related with the intensity variations of pixels belonging to the spatial window defined by the scale α in the input domain.

The scale-space filter smooths noise by applying several iterations to the input image setting the initial value I_{ij} of the central pixel to \bar{I} . The number of iterations can be controlled by the Speckle Index (Section 4.2). If the difference of the Speckle Index between two successive iterations falls below a fixed threshold, the iterations are stopped. In practice, 3 iterations of the filter were found to give acceptable results for ESPI fringes.

Finally, it is important to point out that the scale-space filter was derived for smoothing additive noise. For this reason, data are logarithmically transformed before the filter application.

The computer generated ESPI fringe patterns were created for a resolution of 512x512 pixels by means of the simulation method presented by the authors in Ref. [50]. The assessment was performed using again Eq. 4.6 as the ESPI fringes without noise and the fidelity and the speckle index parameters described in section 4.2.

Figure 5.8(a) shows a computer simulated fringe pattern with variable frequency and visibility used to evaluate the performance of the scale-space filter. The smoothed fringe pattern after the application of the scale-space filter with a 9x9 window and 3 iterations is shown in Fig. 5.8(b). It is seen that noise is effectively suppressed by the filter and that a noticeable increment of visibility is observed near the top of the fringe pattern. However, a slight decrease of visibility can be seen as the fringe density increases towards the right hand side of the image.

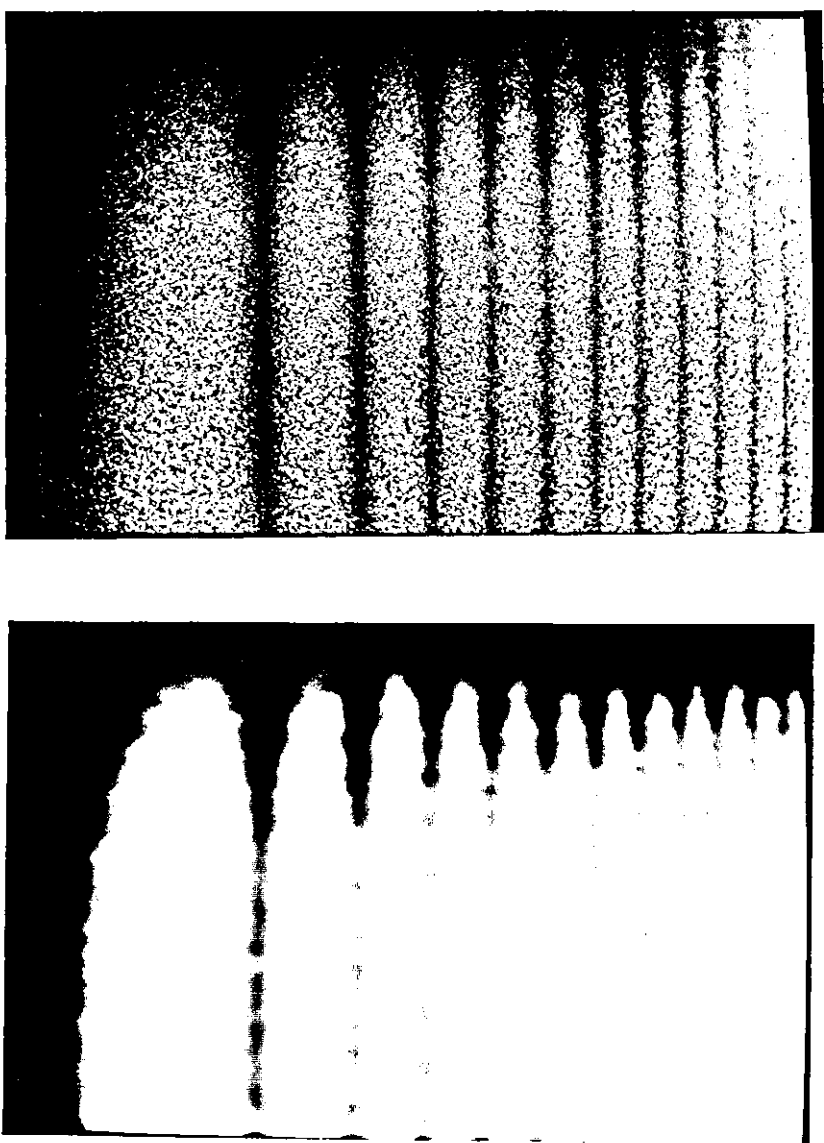


Figure 5.8: Computer simulated fringes with variable frequency and visibility: (a) original image; (b) smoothed image using the scale-space filter for a 9x9 window and 3 iterations.

A quantitative measurement of the noise reduction is given by the Speckle Index. The unfiltered fringe pattern shown in Fig. 5.8(a) gives a value of $s = 0.71$ while the image smoothed with the scale-space filter shown in Fig. 5.8(b), a value $s = 0.029$ is obtained. For comparison, a low-pass Fourier filter applied to the fringe pattern of Fig. 5.8(a) with a radius of 14 pixels gives a slightly higher value of $s = 0.083$. These figures show how speckle noise has been greatly reduced by the application of the scale-space filter.

The influence of different filters in the wrapped phase distribution is an important issue in terms of Engineering applications due to its direct relation to the evaluation of the displacement field, and hence to strain or surface form. For this reason, the wrapped phase distribution ϕ was calculated using three phase-shifted patterns after smoothing each one with a scale-space filter. The phase distribution ϕ was evaluated by a phase stepping technique of two steps and three frames described in table 2.1(see subsection 2.6.1). This calculation allows us to determine the Fidelity value given by the wrapped phase distribution by evaluating the wrapped phase map generated by three phase-shifted noise-free fringe patterns. Smoothing each fringe pattern with the scale-space filter for a 9x9 window and 3 iterations, a Fidelity value of $\bar{\Phi} = 0.91$ was obtained. This value compares quite well with $\bar{\Phi} = 0.94$ obtained after a similar calculation by using a low-pass Fourier filter with a radius of 14 pixels.

One of the main advantages of the scale-space filter is its ability to preserve zero intensity regions usually produced in ESPI by the finite dimensions of the test object and by illumination changes due to concavities or shadowing. To illustrate this advantage, a zero intensity hole was included in three

phase-shifted computer generated fringe patterns. Figure 5.9(a) shows the unfiltered fringe pattern generated for a phase step of 0° . The wrapped phase distribution determined after filtering each pattern with the scale-space filter for a 9×9 window and 3 iterations is seen in Fig. 5.9(b).

From Fig. 5.9(b), it is seen that the gray level distribution obtained using the scale-space filter is maintained nearly constant in the hole region, with minimal distortion of the valid phase data around the edges. In contrast, Fig. 5.9(c) shows the wrapped phase distribution evaluated after a similar calculation but using a low-pass Fourier filter with a radius of 14 pixels. In this last figure, it is observed that the hole is smaller than the one in the unfiltered image shown in Fig. 5.9(a) and also that undesirable phase errors are introduced around the edges, with invalid 'data' appearing in the region itself.

The RMS error σ gives a quantitative measurement of the gray level errors introduced in the hole region. For the wrapped phase distribution evaluated by smoothing with the scale-space filter (Fig. 5.9(b)), a value of $\sigma = 18.6$ is obtained while $\sigma = 55.1$ is calculated by using low-pass Fourier filtering. Figure 5.10 shows plots of the wrapped phase distribution surrounding the hole region after applying both the scale-space and the Fourier filters. For comparison, this figure also shows the plot of the phase obtained from three phase-shifted noise-free fringe patterns along the same direction. It is seen that the phase obtained by using the scale-space filter is quite similar to that evaluated for the noise-free fringe patterns. In contrast, the plot of the phase determined by means of the low-pass Fourier filter strongly departs from the noise-free phase.

In terms of an Engineering application, the resulting loss of the zero intensity regions due to the finite dimensions of the test specimen or to illumination changes, produces a misleading spatial localization of the object and causes local phase distortions at or near the edges. To illustrate this effect, an experimental fringe pattern was recorded. Figure 5.11(a) shows an unfiltered fringe pattern generated by a cracked specimen subjected to a tensile load. In this application, it is important to know the phase distribution in the immediate vicinity of the crack tip as it propagates across the specimen under increasing load. Hence the exact spatial localization of the crack and tip must be segmented from the phase data during the fringe analysis process.

The filtered image obtained by means of the scale-space filter for a 11x11 window and 3 iterations is shown in Fig. 5.11(b). For this image, a Speckle Index value of $s = 0.042$ is obtained. The smoothed fringe pattern determined by using a low-pass Fourier filter with a radius of 10 pixels is shown in Fig. 5.11(c), which gives a Speckle Index value of $s = 0.076$. It is observed that the propagating crack tip has been preserved in the image smoothed with the scale-space filter. On the other hand, not only has the crack tip been blurred and the slot reduced in width in the image smoothed by the low-pass Fourier filter, but also nonzero data has appeared over the slot region. This effect causes inaccuracies in the spatial relationship between the measurement encoded in the fringe pattern (e.g. strain) and the feature of the specimen (i.e. the propagating crack tip).

The number of iterations of the scale space filter (using both 9x9 and 11x11 windows) was increased to test for dependency on fringe frequency. It was

found that increasing above three iterations had no significant effect on reducing the speckle index.

It should be emphasized that the comparatively long computer processing time involved is one of the main limitation of this method. It can be argued that processing time is an important parameter in assessing overall efficiency of the technique. As an example, using a 486 PC running at 66 MHz with the GNU C compiler, the following times were obtained: 200 sec for a 256x256 image, $M=7$ and 3 iterations, 2050 sec for a 512x512 image $M=11$ and 3 iterations. For comparison, a low pass Fourier filter takes 7 seconds for a 256x256 image and 60 seconds for a 512x512 image. As always, processing speed can be improved with more efficient coding or hardware accelerator chips such as the popular TI C80.

5.4 Summary and Remarks

Throughout this chapter the techniques have been subjected to an analysis of their performance for solving the noise problem in pulsed ESPI fringe patterns.

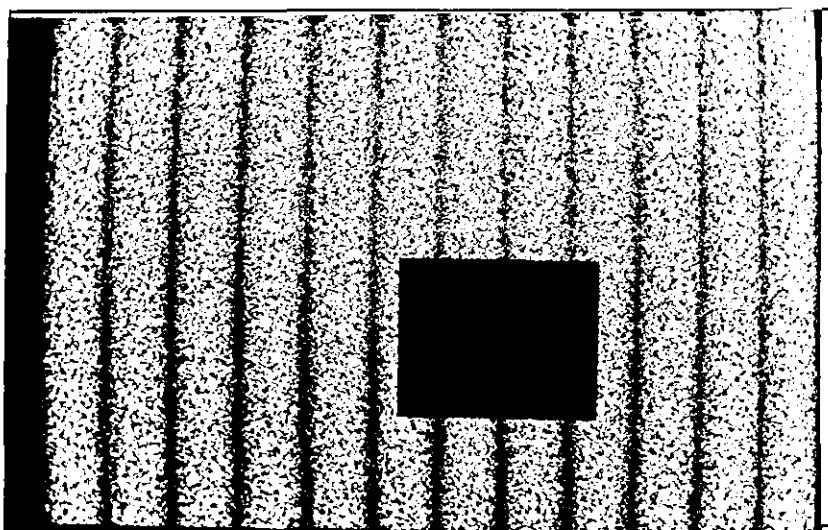
Among the SAR noise reduction techniques it was found that the most efficient methods fall in the category of nonlinear algorithms. This is a natural consequence due to the statistical nature of the speckle field discussed in chapter 3. However as those techniques were developed to enhance speckled images with fine details, their performance in the processing of ESPI fringe

patterns still leave some undesirable high frequency noise in comparison with the low-pass Fourier filter.

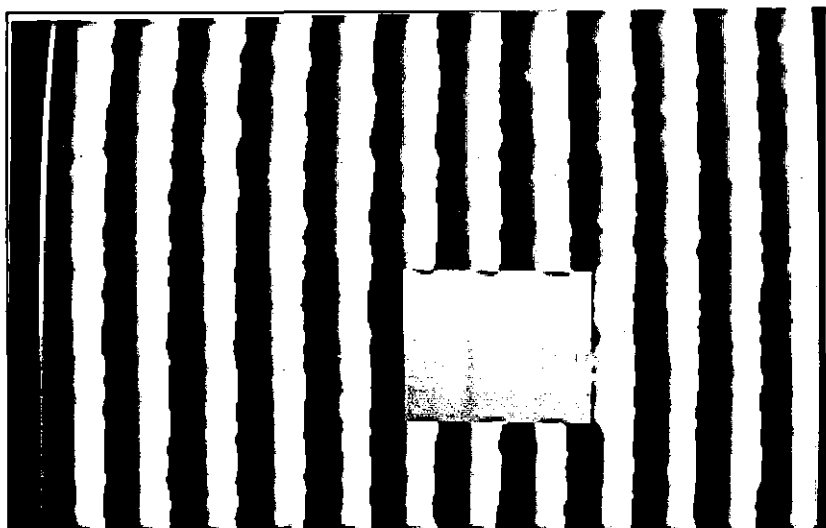
The SSIR method presented in section four, has been shown to be highly efficient if straight fringes are processed. Unfortunately, the performance of this filter decreases for curved fringes.

The scale-space filter has been the most efficient method for noise reduction tested in this thesis. It has shown to be comparable to the low-pass Fourier filter in terms of the quality parameters. Also, the scale-space filter outperforms the low-pass Fourier filter because it preserves the zero intensity regions. This last feature of the filter is similar to the obtained in the SAR methods but with the smoothing characteristics of the low-pass Fourier filter. However, in terms of the processing time is not as good as the other techniques.

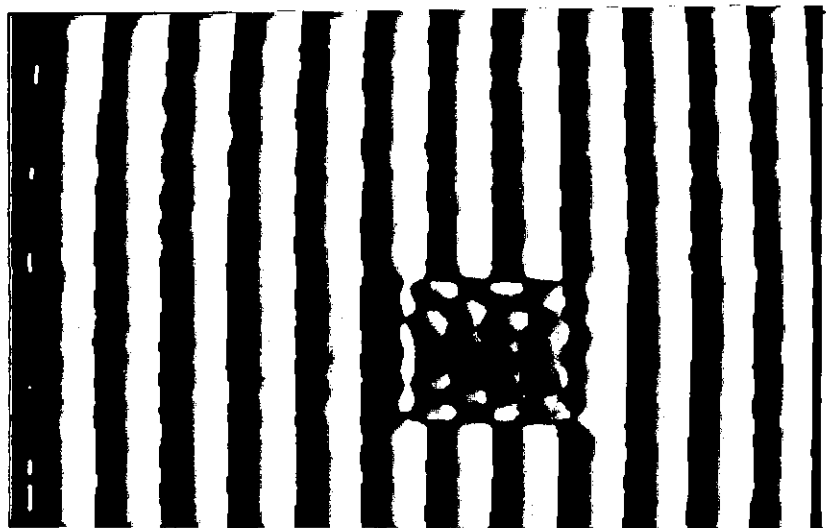
The tradeoff between processing time and quality of the noise reduction technique seems to be directly related: the processing time increases if a better performance in noise reduction is desired. The search for faster methods with smaller processing times is still a current trend in the research of noise reduction algorithms.



(a)



(b)



(c)

Figure 5.9: Wrapped phase distribution evaluated from 3 shifted computer generated fringe patterns which include a simulated hole: (a) original image for a phase step of 0° ; (b) phase determined from 3 smoothed patterns using the scale-space filter for a 9×9 window and 3 iterations; (c) phase determined from 3 patterns smoothed with a low-pass Fourier filter.

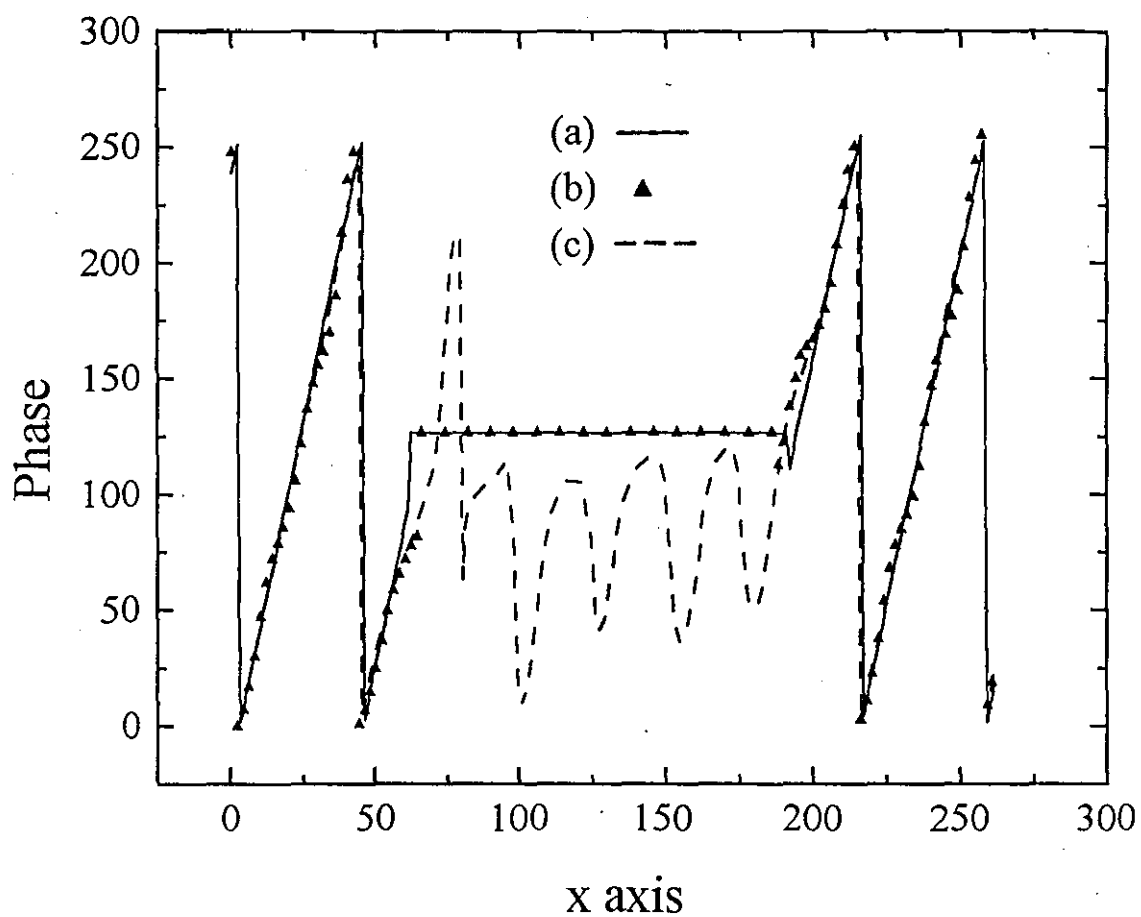
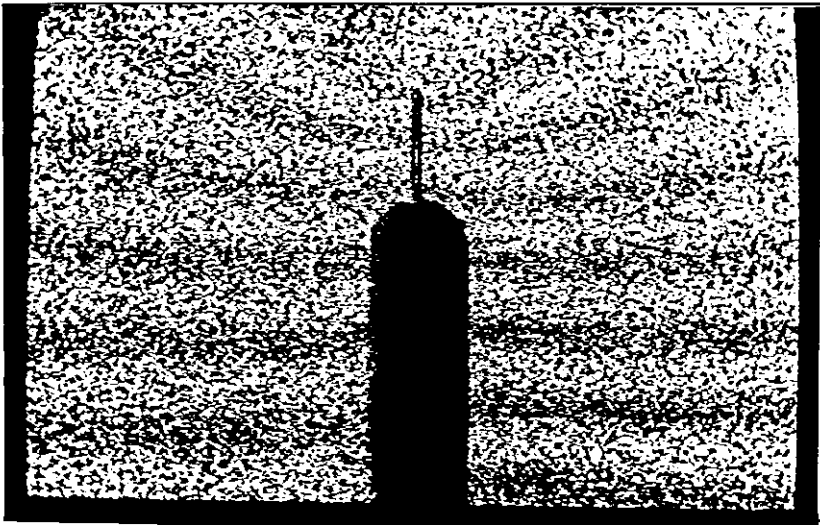
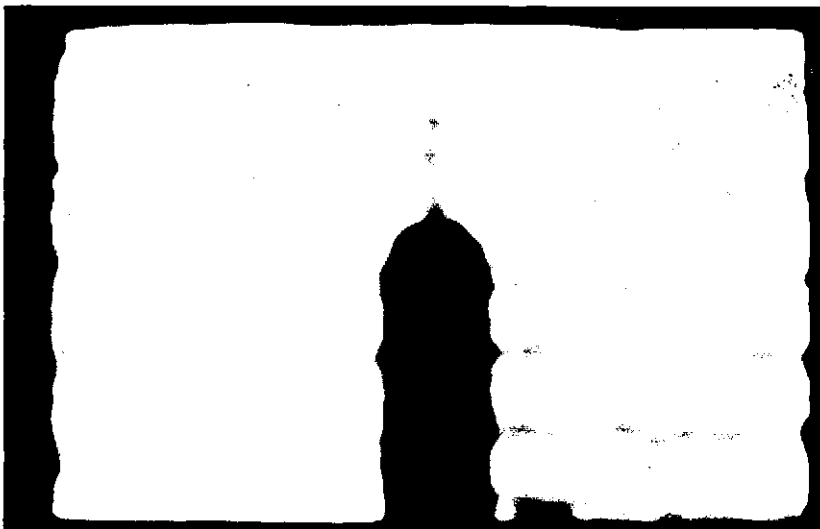


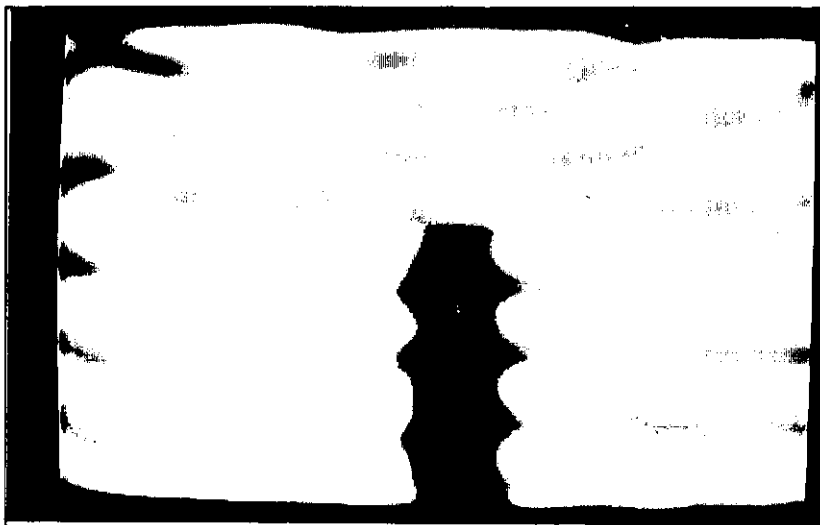
Figure 5.10: Plot of the wrapped phase distribution along a horizontal line across the hole: (a) for a noise-free pattern; (b) for Fig. 5.9(b); (c) for Fig. 5.9(c).



(a)



(b)



(c)

Figure 5.11: Fringe pattern recorded experimentally: (a) original image; (b) smoothed image using the scale-space filter for a 11×11 window and 3 iterations; (c) smoothed image obtained by low-pass Fourier filtering.

Chapter 6

Enhancement of Addition Fringe Patterns

In chapter 2 section 2.5.1 the zero order removal technique was shown to be effective for enhancement of addition fringe patterns. However, a further enhancement of addition fringe patterns can be achieved using gray level transformations. From the distribution of intensity obtained after the zero order removal of section 2.5.1, it is easy to see that the image comprises a large quantity of pixels near to the darker end of the grey level scale. In order to compensate for this effect a logarithm transformation ($\ln(1 + I)$) followed by a normalization gives brighter fringe patterns. This transformation also has been successfully applied in SAR [54]. Fig. 6.1 shows a comparison between the image of fig.2.5(a) and the logarithm scaled image. It can be observed that the intensity has been boosted, but the similarity with the subtraction fringes is lost.

A useful gray level transformation proposed here is the shifted exponential:

$$I' = e^{-\zeta_0|I-I_{max}|} \quad (6.1)$$

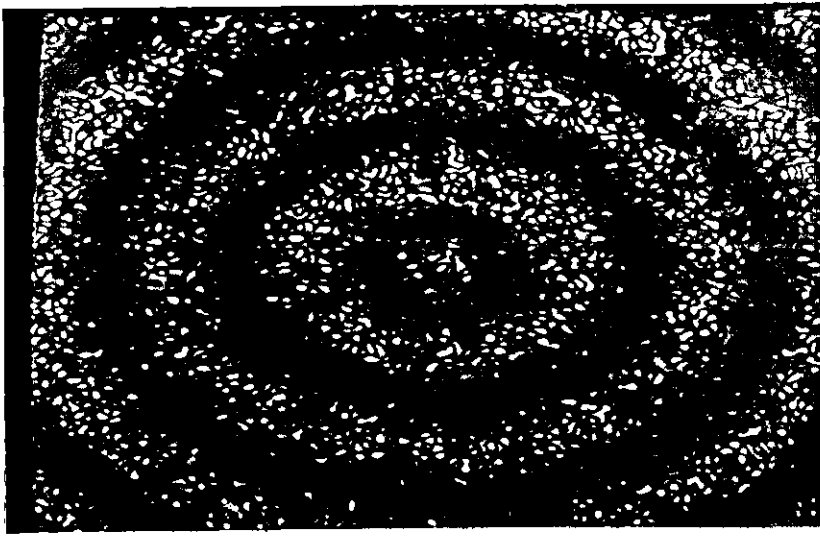
where ζ_0 is a constant and I_{max} is the maximum intensity of the ESPI pattern.

After normalization, this transformation produces a fringe contrast similar to the subtraction ones. For a comparison, figure 6.1(c) shows the result of the shifted exponential transformation.

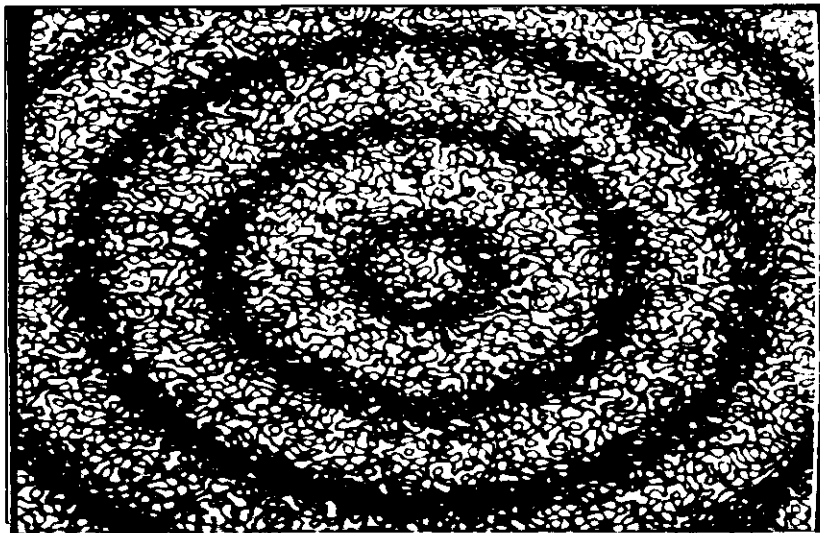
6.1 Experimental Enhancement of Addition Fringes by Zero Order Removal

In the experimental results, an out-of-plane ESPI interferometer was used to generate the two primary speckle interferograms of a torsion plate. These interferograms were recorded with a displacement between exposures. The addition of these is shown in figure 6.2(a). Next, the techniques presented in section 2.5.1: zero order removal technique and shifted exponential gray level transformation were applied. The resulting fringe pattern is easily perceived in figure 6.2(b).

It can be seen that an outstanding increase in visibility of the fringes has been reached. However, their general appearance seems to be of lower contrast than those obtained with subtraction correlation. This point was previously discussed in relation to the computer generated images of section 2.5.1.



(a)



(b)



(c)

Figure 6.1: Grey scale re-transformation of the intensity distribution of an enhanced addition pattern: (a) Enhanced addition pattern, (b) Logarithm re-transformation of intensity values, (c) Shifted exponential re-transformation of intensity values.

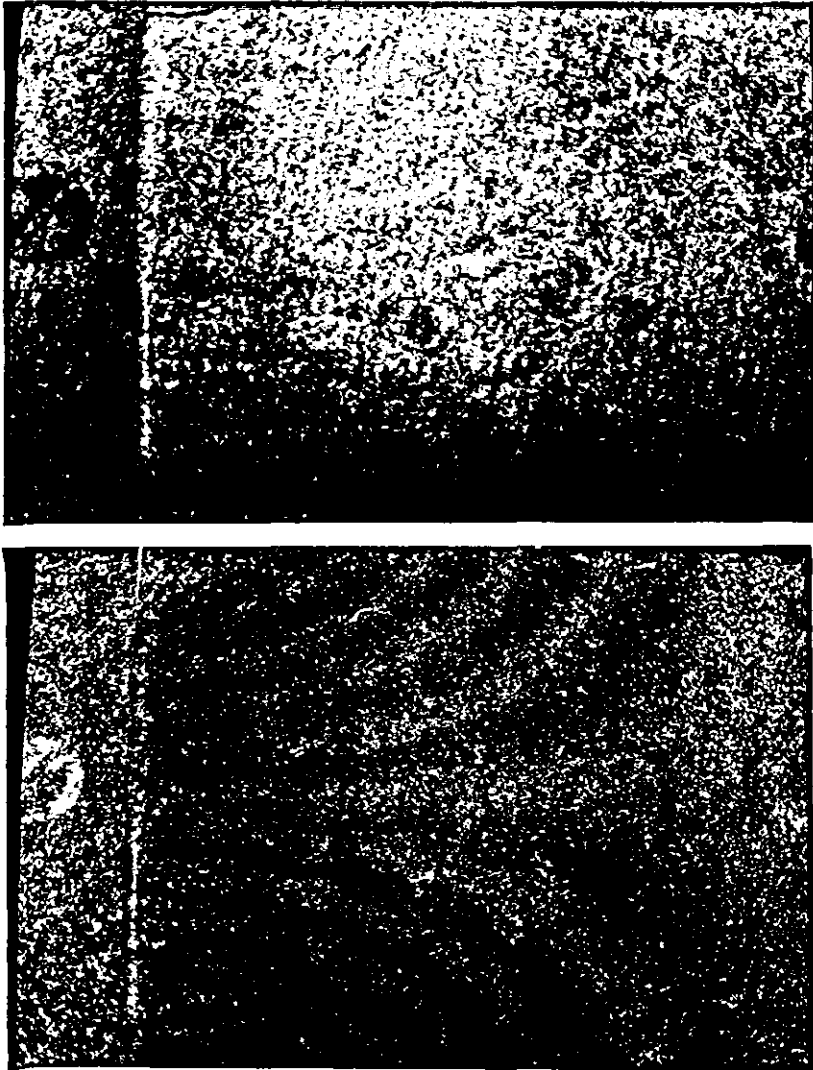


Figure 6.2: (a) ESPI addition fringes generated by adding two interferograms with torsion introduced between both exposures; (b) enhanced pattern obtained by zero order removal and a shifted exponential grey level transformation.

6.2 Enhancement of Addition Fringes by Subtraction of a Reference Interferogram

A detailed theoretical and experimental investigation of the contrast enhancement produced by the subtraction of two addition fringe patterns can be found in Ref. [12]. Therefore, only a brief account is given here.

The irradiance, I_1 , of the correlation fringes generated by the addition of two speckle interferograms recorded within the same TV frame may be written as [6]

$$I_1 = A + B [\cos\Psi + \cos(\Psi + \Delta\alpha)], \quad (6.2)$$

with

$$A = 2(I_0 + I_r) \quad \text{and} \quad B = 2\sqrt{I_0 I_r} \quad (6.3)$$

where I_0 and I_r are the irradiances of the object and reference beams, respectively, Ψ is the random speckle phase, and $\Delta\alpha$ is the phase difference introduced by the deformation.

Assuming that is possible to obtain a reference interferogram with the object in static or dynamic equilibrium, a new double pulse is fired by the laser such that no deformation is introduced between the pulses. Irradiance I_2 caused by the addition of these last two speckle interferograms is thus given by

$$I_2 = A + 2 B \cos\Psi. \quad (6.4)$$

Using Eqs. 6.2 and 6.4, it is easy to show that

$$I_{12} = I_2 - I_1 = 2 B \sin^2\left(\Psi + \frac{\Delta\alpha}{2}\right) \sin^2\frac{\Delta\alpha}{2}. \quad (6.5)$$

Here irradiance I_{12} describes high quality \sin^2 fringes with a visibility equal to subtraction fringes. In this way, by subtracting a reference interferogram, one can obtain addition fringes of improved visibility, allowing ESPI to be used for transient phenomena analysis. It should be noted that the above analysis assumes that speckle phase Ψ is the same for recording of irradiance distributions I_1 and I_2 . This is a familiar condition for the formation of ESPI correlation fringes [67].

In the experimental results presented in section 5.2 the addition fringes were enhanced by subtraction of a reference interferogram so the quality is the same as the subtraction fringes.

The main disadvantage of this method arises in the case of transient events as a requirement of special experimental conditions; i.e. the synchronization of the transient event with the two consecutive double pulses. In the case of oscillatory events, it is assumed that the reference interferogram I_1 is registered in static position such that exactly the same interferogram is obtained when the oscillating object is in its equilibrium position. However this is only true for purely periodic events, any slight depart from this condition can produce combined interferograms [12].

Chapter 7

Phase Extraction Methods

In this chapter, the carrier fringe technique used in this thesis is analyzed to describe the main limitations that are introduced when ESPI fringes are processed with this method. As a complement, the phase unwrapping algorithm used during the work undertaken for this thesis is described briefly.

7.1 Carrier fringe limitations

In evaluating its overall performance, it is useful to estimate how the carrier fringe method compares to conventional techniques. Vlad & Malacara [72] provide an excellent analysis of carrier fringe methods and their limitations, and Green et al [110] specifically investigate limitations of the Fourier domain phase extraction technique. The reader is referred to these publications for a full theoretical analysis; here a brief description of the practical consequences

is presented. Essentially there are four main limitations in measurement accuracy and range, these being due to bandwidth, signal to noise ratio, filtering and sampling, and speckle size.

i. Bandwidth.

It is generally agreed that the first two terms and $\bar{\phi}(x, y)$ in Equation 2.10 must be slowly varying compared to the carrier frequency ϕ_0 . It is thus the carrier frequency magnitude which limits the displacement measuring range. The carrier frequency is modulated by the slope of the phase function, $\partial\bar{\phi}(x, y)/\partial x$ and so we have the condition [72] to avoid over-modulation of

$$\phi_0 \ll \left| \frac{\partial\bar{\phi}(x, y)}{\partial x} \right|_{max} \quad (7.1)$$

If ϕ_0 is not large enough for a given target displacement, then the lobes in the Fourier spectrum (Figure 2.7(b)) will not be well separated (i.e. there is insufficient bandwidth) and the method will fail. This can be seen experimentally when initially vertical carrier fringes become so curved that they cross a line parallel to the x-axis more than once. For a predominantly x-directed displacement, this effect manifests itself in an infinite fringe separation. Vlad and Malacara [72] suggest that for the Holographic case, this separability condition is met if $\phi_0 \gg 3\bar{B}$ where \bar{B} is the signal bandwidth, assuming that the carrier lobe is broadened by $\pm\bar{B}$.

ii. Signal to noise ratio and speckle size.

These essentially limit the upper modulation frequency of the carrier

fringes. When the fringes are formed by speckle correlation and so the maximum carrier frequency is itself limited by the speckle size. This will in general be well below the Nyquist limit for the TV system employed (around 4 speckles per cycle of carrier are required practically). Green et al [110] found that an acceptable noise limit was reached at a signal to noise ratio of around 2.0 using 4 pixels per fringe resolution. The aim must be to keep the speckle size as small as possible, within the optical resolution limit of the camera. This actually has an associated bonus in that a large camera aperture is implied, making the technique more light efficient. The fringe visibility (modulation depth) must also be high to achieve sufficient signal to noise ratio everywhere in the image.

iii. **Filtering and sampling.**

The image edges constitute a spatial sampling window. The discrete Fourier transform assumes a periodic repeat of the data outside this window and thus abrupt changes in carrier magnitude cause spurious frequencies in the Fourier domain which limit the lobe separability [110]. Application of a simple Hanning window to the modulated carrier fringes can significantly increase the separability and hence the performance of the method. A rectangular filter was chosen for simplicity but its sharp cutoff characteristic induces ‘ringing’ in the extracted phase. A Gaussian or Butterworth filter profile would perform better in this respect.

7.2 Phase Unwrapping Algorithm

Unwrapping of phase maps is currently the subject of extensive research in which a large number of techniques have been developed for automated fringe analysis [62, 111]. Other algorithms have evolved in isolated research groups from diverse areas such as magnetic resonance imaging [112] and SAR [113]. In general terms the algorithms can be classified as path-following (either in space or in time) and of estimation of phase values by using local phase differences [112].

In this thesis, the Cosine Transform phase unwrapping developed by Ghiglia & Romero was chosen for processing phase maps due to its robustness against noise. As it is based on a least squares phase estimation method, the remaining noise after the noise reduction algorithms does not corrupt strongly the resulting unwrapped phase values. A review of the basic theory for the algorithm 1 described in [63] is presented next and some inconveniences of the implemented algorithm are discussed briefly.

In the original paper [63] the theory for two different methods is described in detail, here only the basic equations required for the calculation of the non-iterative, non-weighted algorithm are presented. The reader is strongly recommended to consult this publication for full details of the mathematical development.

The algorithm is based on the estimation of the phase differences by means of a least squares procedure that can be shown to be mathematically identical

to the solution of the Poisson equation on a rectangular grid with Neumann boundary conditions (i.e. $\partial\psi/\partial x; \partial\psi/\partial y = 0$).

The Neumann boundary conditions in our case can be imposed to the wrapped phase map for rows, columns and corners of a $M \times N$ wrapped phase array $\psi_{i,j}$ as

$$\begin{aligned} \psi_{i,0} &= \psi_{i,1} \\ \psi_{i,N-1} &= \psi_{i,N-2} \quad i = 0, \dots, M-1 \end{aligned} \quad (7.2)$$

$$\begin{aligned} \psi_{0,j} &= \psi_{1,j} \\ \psi_{M-1,j} &= \psi_{M-2,j} \quad j = 0, \dots, N-1 \end{aligned} \quad (7.3)$$

$$\begin{aligned} \psi_{0,0} &= \psi_{1,1} \\ \psi_{0,N-1} &= \psi_{1,N-2} \\ \psi_{M-1,0} &= \psi_{M-2,1} \\ \psi_{M-1,N-1} &= \psi_{M-2,N-2}. \end{aligned} \quad (7.4)$$

After imposing these conditions the next step is to calculate the right hand term¹ of the discrete representation of Poisson equation:

$$\rho_{i,j} = (\Delta_{i,j}^x - \Delta_{i-1,j}^x) - (\Delta_{i,j}^y - \Delta_{i,j-1}^y). \quad (7.5)$$

¹The left hand term equation that arises from the least squares phase unwrapping solution that relates the wrapped phase differences to the unwrapped phase values has been avoided in the explanation to provide a clearer view of the steps involved in the algorithm.

where the phase difference term $\Delta_{i,j}$ is defined in the horizontal and vertical directions as

$$\Delta_{i,j}^x = W(\psi_{i+1,j} - \psi_{i,j}) \quad (7.6)$$

$$\Delta_{i,j}^y = W(\psi_{i,j+1} - \psi_{i,j}) \quad (7.7)$$

$\rho_{i,j}$ is the Laplacian phase vector [111] and W is a wrapping operator that wraps all values of its argument into the range $(-\pi, \pi)$.

The next step involves the forward two-dimensional discrete cosine transform (DCT) calculation that can be performed using the numerical recipes software [114]. Then, the solution requires the calculation of:

$$\hat{\phi}_{\bar{m},\bar{n}} = \frac{\hat{\rho}_{\bar{m},\bar{n}}}{2(\cos(\pi\bar{m}/M) + \cos(\pi\bar{n}/N) - 2)} \quad (7.8)$$

from the $\hat{\rho}$ values of the DCT. In this equation (\bar{m}, \bar{n}) are the coordinates in the resulting values of the DCT.

Finally, after applying the inverse DCT to the filtered result of Eq. 7.8 the least-squares unwrapped phase values $\phi_{i,j}$ are obtained.

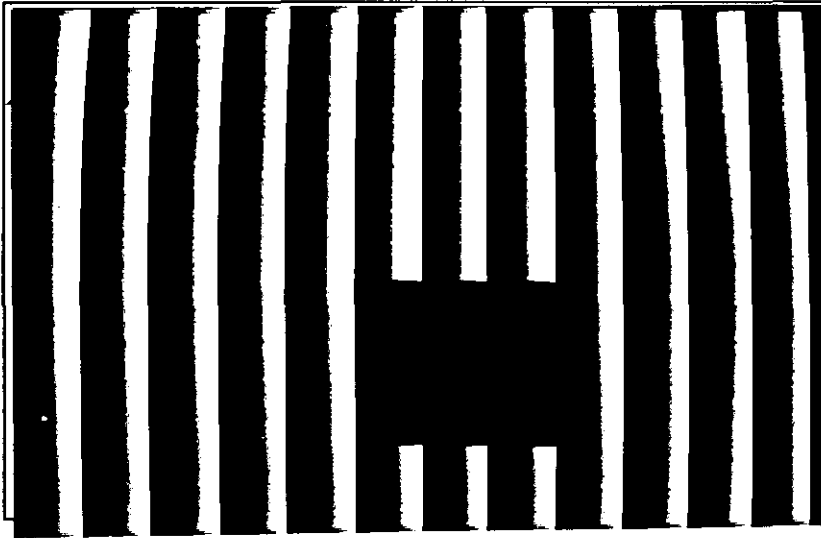
This algorithm has been tested in the original paper for inconsistencies in the phase values. It has been shown that it distorts slightly the phase values in the local neighborhood of the inconsistency. However is not very noticeable in the phase maps provided. For this reason, figures 7.1(a)-(c) show this effect in greater detail. Figure 7.1(a) presents a phase map that was generated by using the two step, three frames phase stepping method with parallel fringes. As a additional feature a zero intensity region (inconsistency) was masked in the fringe patterns. Figure 7.1(c) presents the resulting re-wrapped

phase after the phase estimation shown in Fig. 7.1(b). It can be seen that the number of phase steps in the surrounding area of the inconsistency has decreased. This can be interpreted as a decrease of the horizontal slope in the phase function. When the required phase values are normalized at the end, this effect is not important. However when related to displacement values, this decrease in slope can represent a misleading reduced displacement.

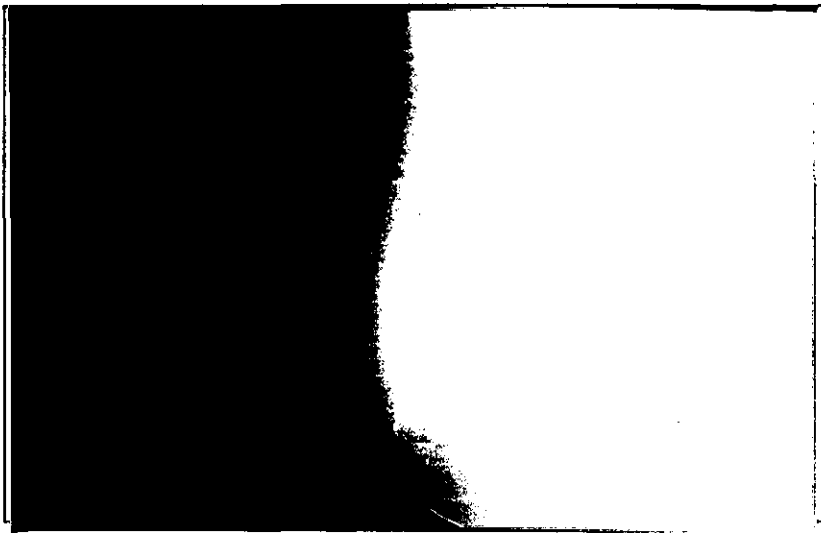
Another interesting effect of the application of the algorithm previously described arises when the object is smaller than the area of processing. Figure 7.2(a) shows a phase map that is included in an area smaller than the processing area. The re-wrapped result of the algorithm is presented in figure 7.2(c) from the unwrapped phase map of Fig. 7.2(b). It can be observed a similar effect than the discussed previously for the inconsistency "submerged" in the phase map. The number of phase jumps inside the area of the original phase map has decreased, so attempt of measuring inside the area will produce erroneous figures. Also new phase jumps are now present in the regions previously with zero phase. This effect is not important from the practical point of view because a mask can be generated to avoid this area.

This mentioned problems disappear when the Picard iteration algorithm ("algorithm 2" of the Ghiglia paper) is used. This algorithm preserve the zero phase areas without changing the phase slope, given sufficient iterations and correct choice of weights [111]. However, for the experimental purposes of this work the "algorithm 1" preserves some details (perhaps inconsistencies) that can be useful for spatial localization of the object details.

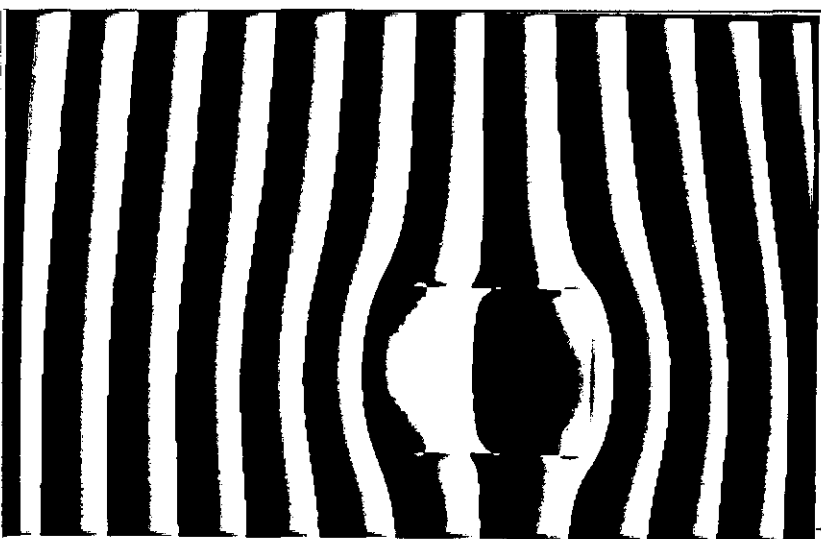
The research in the area of phase unwrapping algorithms is still very intense,



(a)

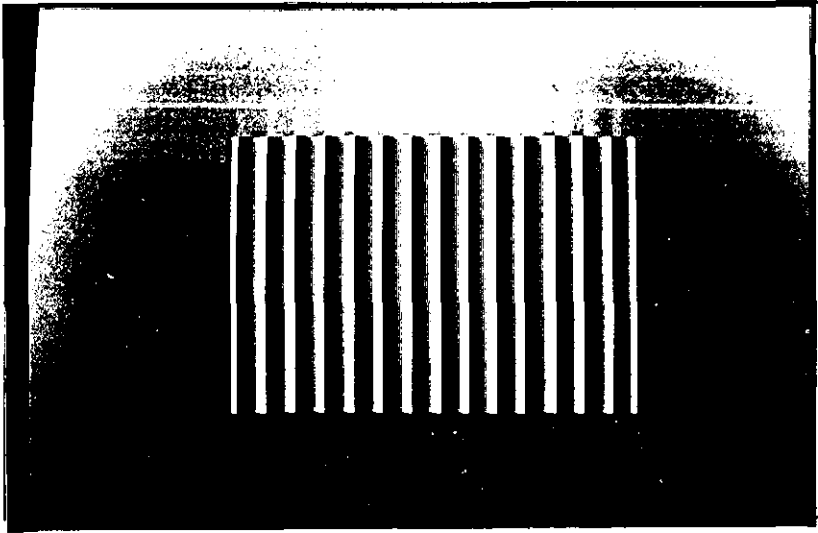


(b)

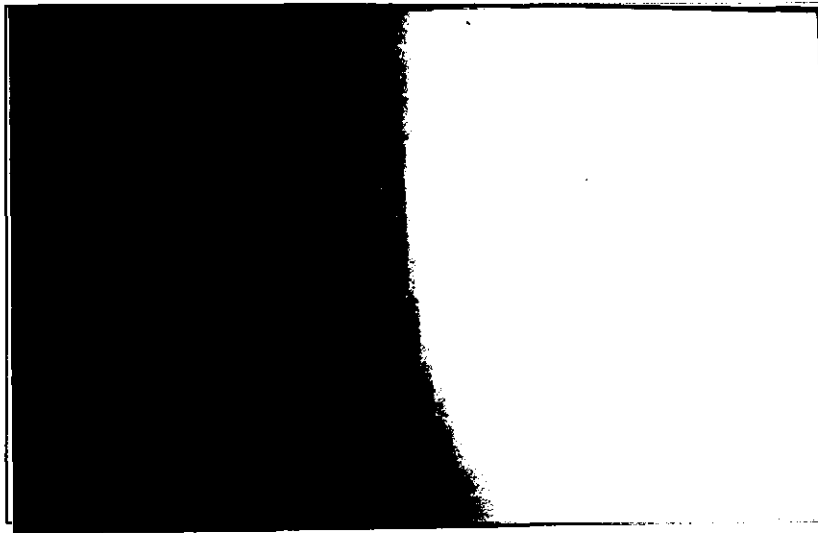


(c)

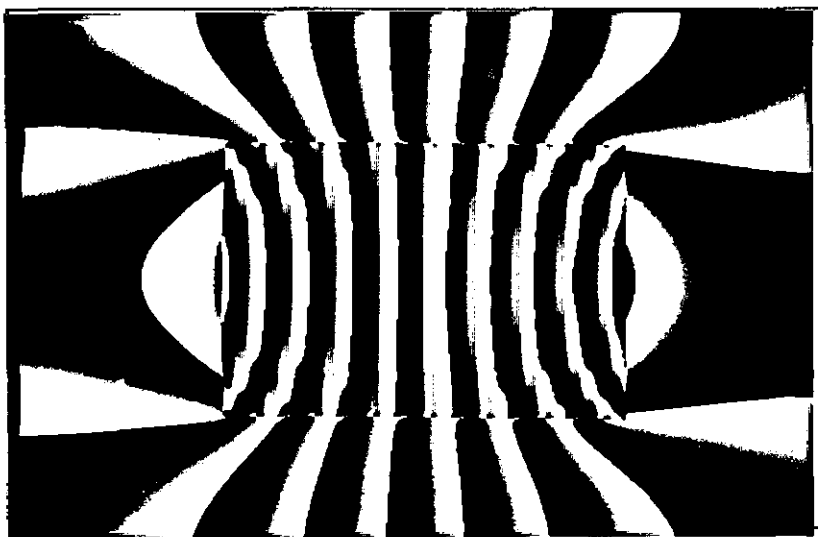
Figure 7.1: (a) Phase map with a square zero phase region. (b) Unwrapped phase map from values depicted in (a). (c) Rerapped phase values for comparison with figure (a).



(a)



(b)



(c)

Figure 7.2: (a) Phase map smaller than the processing region used for unwrapping. (b) Unwrapped phase map from values depicted in (a). (c) Rewrapped phase values for comparison with figure (a).

for the purposes of transient event detection the faster algorithms seems to be the more appropriated. Provided, of course, that the unwrapped phase preserve the spatial details of the object.

Chapter 8

Whole Field Transient Event Detection

This chapter describes the author's solution to the problem of transient event detection using an electro-optical system to produce carrier fringes in very short intervals of time. This procedure allows the unambiguous extraction of phase (as was shown in section 2.5 and chapter 6) even from addition fringe patterns. Although this last technique was tested using only real-time subtraction correlation in a experiment with a single pulse Nd:YAG laser, it is easy to see from the CW experiments presented there that the addition correlation case will not differ significantly.

Finally, in the last section a comparison of the three optical techniques discussed in this thesis for whole field transient event detection and their trade-offs is presented.

8.1 High Speed Optical System for Carrier Generation

To overcome many of the mentioned limitations of the preceding two systems discussed in subsections 2.7.1 and 2.7.2, an electro-optical system based on the use of a Pockels cell has been developed by the author [115] that enables the introduction of addition carrier fringes between the firing of two consecutive laser pulses. The method uses a standard frame transfer CCD camera without undue restriction of the laser pulse separation, and allows calculation of the wrapped phase distribution from a single image using Spatial Synchronous Detection (SSD) [71] i.e. carrier fringes.

In this chapter the pertinent optical system and phase evaluation method are described, together with experimental measurements performed using a continuous-wave laser. Also, preliminary results obtained with a Nd:YAG single pulsed laser are presented in the analysis of a transient event. To finalize, some of the limitations of the developed method are also discussed.

Spatial modulation in correlated out-of-plane ESPI patterns can be easily obtained by a simple tilt of the object after the acquisition of the first speckle field. As the correlation relies on the phase difference introduced with respect to the reference beam, the same effect can be obtained by tilting the reference beam. However, ESPI sensitivity to small movements of the optical components makes this task difficult if a mechanical device is used, since the spatial synchronous technique requires a constant phase modulation. Also, the speed of any applied tilt would cause inevitable vibrations in the optical

rig due to the high accelerations needed. The author presents here an electro-optical system which produces carrier fringes for the application of the SSD technique in an out-of-plane ESPI. To obtain carrier fringes, the interferometer has been modified to generate two consecutive reference beams tilted with respect to each other. One or other of these beams is introduced into the interferometer by means of the electro-optical system shown in Figure 8.1.

The key element in the high speed modulation procedure is a Pockels cell (PC) located after the light beam that is reflected from mirror M0. Its voltage is controlled to obtain either horizontal or vertical output polarization. After the Pockels cell, the beam is expanded by a collimator (C) and passes through a polarizing beam splitter (PB) that is used to redirect the beam to one of the two mirrors M1 or M2. If the reference beam is horizontally polarized, the output from the polarizing beam splitter is sent to M1, passing first through a $1/4$ wave plate (W) that transforms the linear polarization into a circular one. After the M1, the light beam is returned with its circular polarization in the opposite direction. After the wave plate, the resulting polarization is rotated by 90° and passes through the beam splitter. The component at 45° is then selected by means of a dichroic polarizer P1. The resulting beam is used as the first reference beam of an out-of-plane ESPI interferometer. When the Pockels cell produces vertical polarization, a similar process occurs but this time the trajectory is via M2. After P1, the component at 45° gives a second reference beam. After the non-polarizing beam splitter (NPB), each reference beam then interferes with the polarized object beam that arrives through the polarizer P2, the camera lens and the non-polarizing beam splitter.

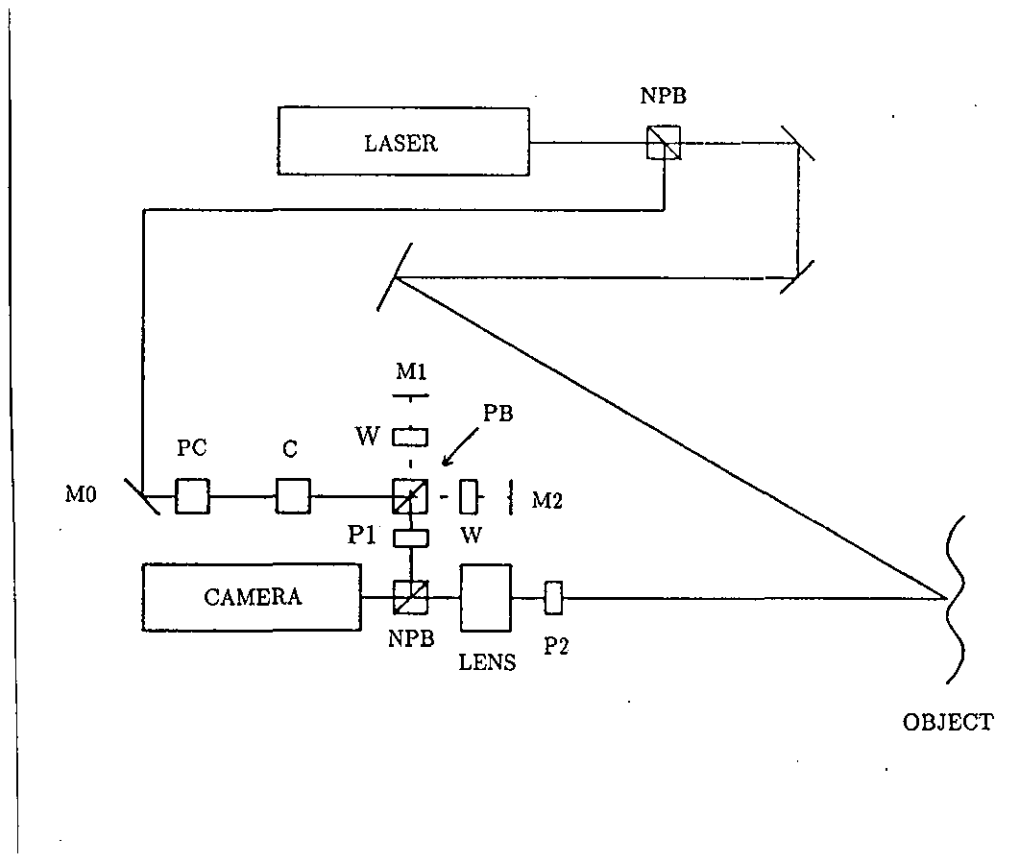


Figure 8.1: Diagram of the electro-optical system used to generate carrier fringes.

Mirrors M1 and M2 form a simple Michelson arrangement. When these are perpendicular, each state of polarization produced by the Pockels cell gives two identical reference beams after P1. However, if a tilt is introduced in one of the mirrors, the path difference gives carrier fringes when the addition correlation procedure is applied. To set up the apparatus, a predetermined number of carrier fringes can be generated by reducing the voltage in the Pockels cell to allow components of both beams to reach the camera. Then, a careful manual adjustment of the tilt between mirrors M1 and M2 in the Michelson arrangement can produce any desired number and orientation of carrier fringes over the camera face plate. These are adjusted by observing the monitor screen.

In application of the method, the object under test is subjected to a transient displacement while the two reference beams are used separately. Each reference beam is synchronized in time, so that each interferes consecutively with one of the two light pulses generated in the twin pulsed laser. As the polarization state introduced by the Pockels cell can be changed at a very high speed, the system is able to introduce carrier fringes between the firing of the laser pulses. Thus the procedure can be used to extract displacement phase unambiguously from the ESPI addition fringes recorded.

Before the phase extraction process can be carried out, it is necessary to remove the speckle noise from the image. This was accomplished in the Fourier domain using a thresholded (power magnitude selective) filter, followed by a low-pass (frequency selective) ideal filter. Thus both high and low frequency components of speckle noise were removed, whilst retaining the modulated frequencies of interest. A detailed description of phase evaluation using the

SSD method can be found in references [71, 72], therefore, only a brief account is given here.

The digitized intensity $I(x, y)$ of the filtered correlation fringes modulated by a vertical carrier fringe pattern of frequency f_0 may be written as

$$I(x, y) = a(x, y) + b(x, y) \cos[\phi_p(x, y) + 2\pi f_0 x] \quad (8.1)$$

Here $a(x, y)$ represents the background intensity, $b(x, y)$ is the local contrast of the fringes and $\phi_p(x, y)$ is the phase term to be evaluated. It is supposed that the spatial variations of $a(x, y)$, $b(x, y)$ and $\phi_p(x, y)$ are slow compared to the carrier frequency f_0 [72, 110]. As vertical carrier fringes have been used, the analysis proceeds by treating each of the N horizontal lines of the image in isolation.

The products $I_s(x)_{n_0} = I(x)_{n_0} \sin(2\pi f_0 x)$ and $I_c(x)_{n_0} = I(x)_{n_0} \cos(2\pi f_0 x)$ are evaluated, the subscript n_0 being an integer in the range $(0 \leq n_0 < N)$ denoting the line to be analysed. It can then be demonstrated that in the frequency domain each product consists of three separated terms. The first two terms are at the carrier frequency f_0 and at $2f_0$, while the third is centred about the frequency origin. This last term represents a low-frequency moiré pattern which is formed when the intensity $I(x)_{n_0}$ of the modulated carrier fringes is multiplied by $\sin(2\pi f_0 x)$ or by $\cos(2\pi f_0 x)$. This term can be separated from the remaining terms by using a low-pass filter $h(x)$. Filtering may be performed in either the space domain (convolution mask filter) or in the frequency domain (rectangular Fourier filter $H(u)$). The resulting

filtered image lines $G_s(x)_{n_0}$ and $G_c(x)_{n_0}$ may then be processed to extract the wrapped phase $\phi(x)$ using the relation

$$\phi_{n_0}(x) = \arctan \left\{ \frac{G_s(x)_{n_0}}{G_c(x)_{n_0}} \right\} \quad (8.2)$$

The SSD method is thus quite simple to apply when only a single frame of intensity data is available. However, it must be pointed out that the low spatial frequency moiré must be efficiently isolated to keep the phase measurement error small.

To test the electro-optical system under static loading conditions, a continuous wave laser was used in lieu of the intended pulsed source to generate addition carrier fringes using the optical layout in Figure 8.1. An Imaging Technology FG100 frame grabber and PC host computer were used to perform the real time addition of consecutive TV frames at a resolution of 512x512 pixels at 64 grey levels (6 bits per pixel). Fringe quality was first improved by zero order removal from the Fourier power spectrum followed by contrast enhancement. Resulting images were stored on hard disc for later processing at 8 bit grey level resolution.

To confirm the generation of carrier fringes due to the tilt between mirrors M1 and M2, two speckle fields were recorded with the target (a square metal plate firmly supported at its edges) undeformed. A voltage was applied to the Pockels cell to switch reference beams before the acquisition of the second field, and carrier fringes were thus formed by addition. Figure 8.2(a) shows the carrier fringes obtained. Carrier frequency may be controlled by adjusting the angle of tilt between the mirrors. Figure 8.2(b) shows the

resulting modulated addition carrier fringes when a central load is applied to the target. The speckle noise reduction filters are then applied to the modulated fringe pattern of Figure 8.2(b) in the two dimensional Fourier domain. Results of this process are shown in Figure 8.3(a).

When the modulated carrier fringe pattern is processed line by line using a one dimensional Fourier transform, two frequency lobes or 'side bands' appear in the power spectrum as shown in Figure 8.3(b). Both lobes are shifted from the zero order towards the edges of the spectrum by an amount determined by the carrier frequency. When the object displacement is applied, these lobes will broaden. The underlying intensity distribution is generated mostly by the speckle noise in conjunction with the sampling effects of the CCD camera. For the application of the SSD method, a low-pass rectangular Fourier filter $H(u)$ is applied whose width is determined by the displacement. Initially, this width may be set equal to half the value of the carrier frequency, but larger bandwidths will require this to be increased (see section 2.6.3).

It is seen in Figure 8.3(c) that the wrapped phase obtained using Eq. 8.2 is almost free of defects. To provide a better picture of the phase, the cosine transform unwrapping algorithm [63] was applied to the wrapped phase maps, the results obtained being shown in the wire frame plot in Figure 8.4.

The accuracy and range of this method are slightly less than that of the more 'conventional' phase stepping techniques, but it has the significant advantage of unambiguous phase determination from a single fringe pattern. This factor is vital in determining transient event analysis capability, as twin pulsed addition displacement using very short pulse separations only becomes feasible with this technique. Assuming sufficiently low switching times for the

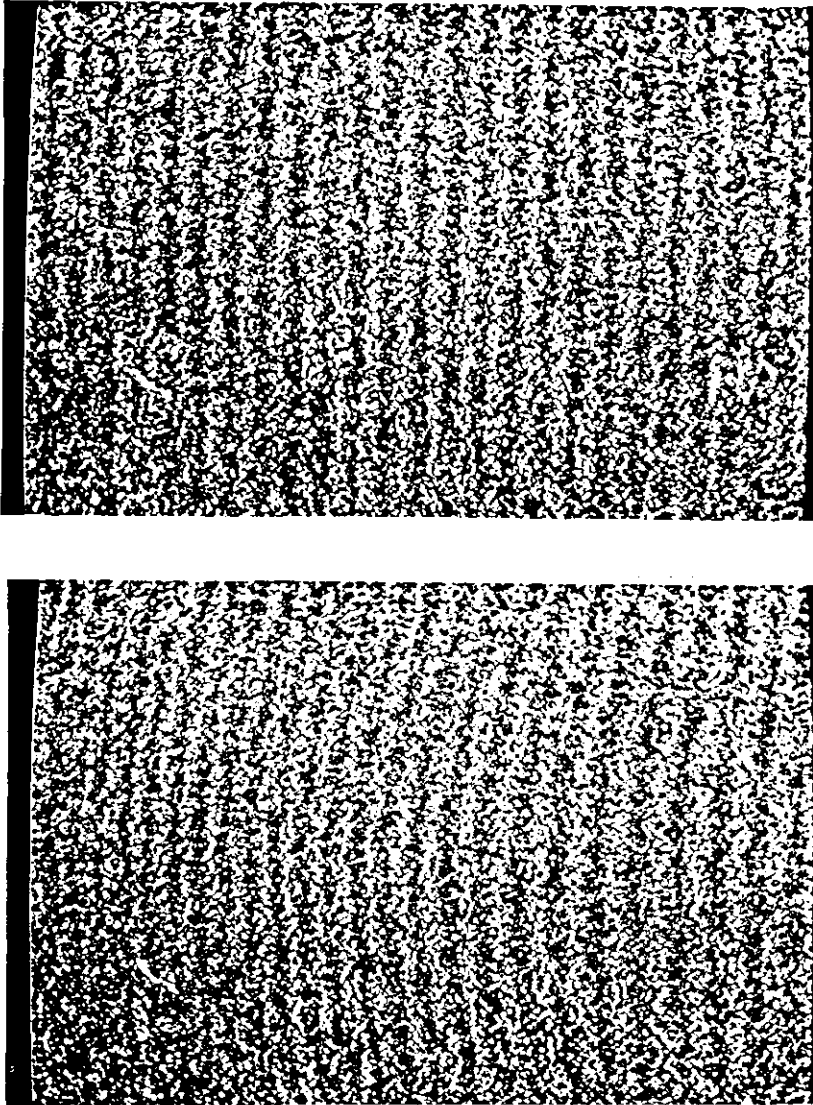
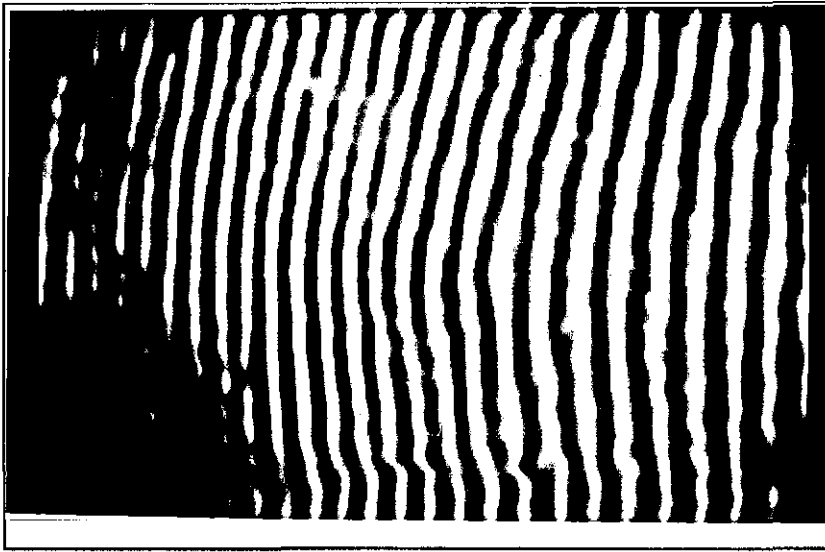
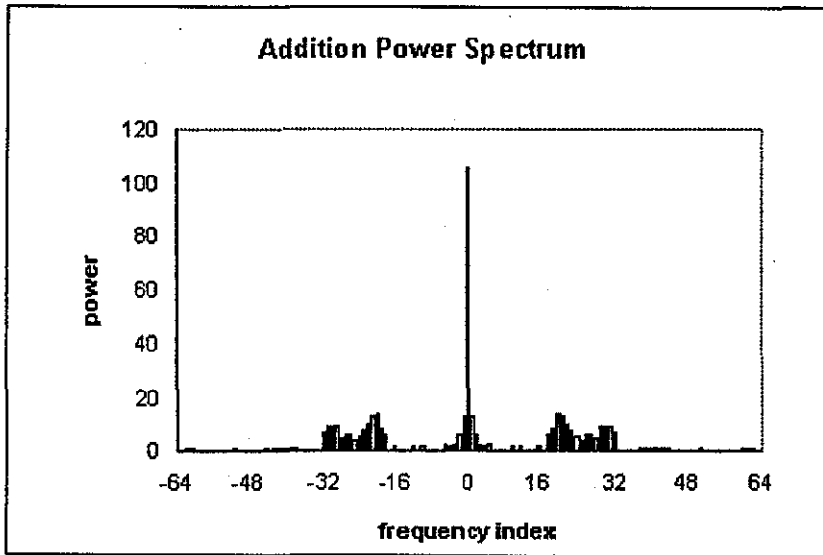


Figure 8.2: (a) Typical pattern of vertical addition carrier fringes produced by a small tilt between the reference path mirrors, after enhancement by zero order removal. (b) Vertical carrier fringes modulated by a central displacement of the target plate, after enhancement by zero order removal.



(a)



(b)



(c)

Figure 8.3: (a) Image obtained by the application of low-pass and amplitude thresholded Fourier filters to the fringe pattern shown in Figure 8.2(b). (b) Fourier transform power spectrum of one line of the fringe pattern shown in Fig. 8.3(a). (c) Wrapped phase map obtained after processing line by line the filtered fringe pattern of Figure 8.3(a).

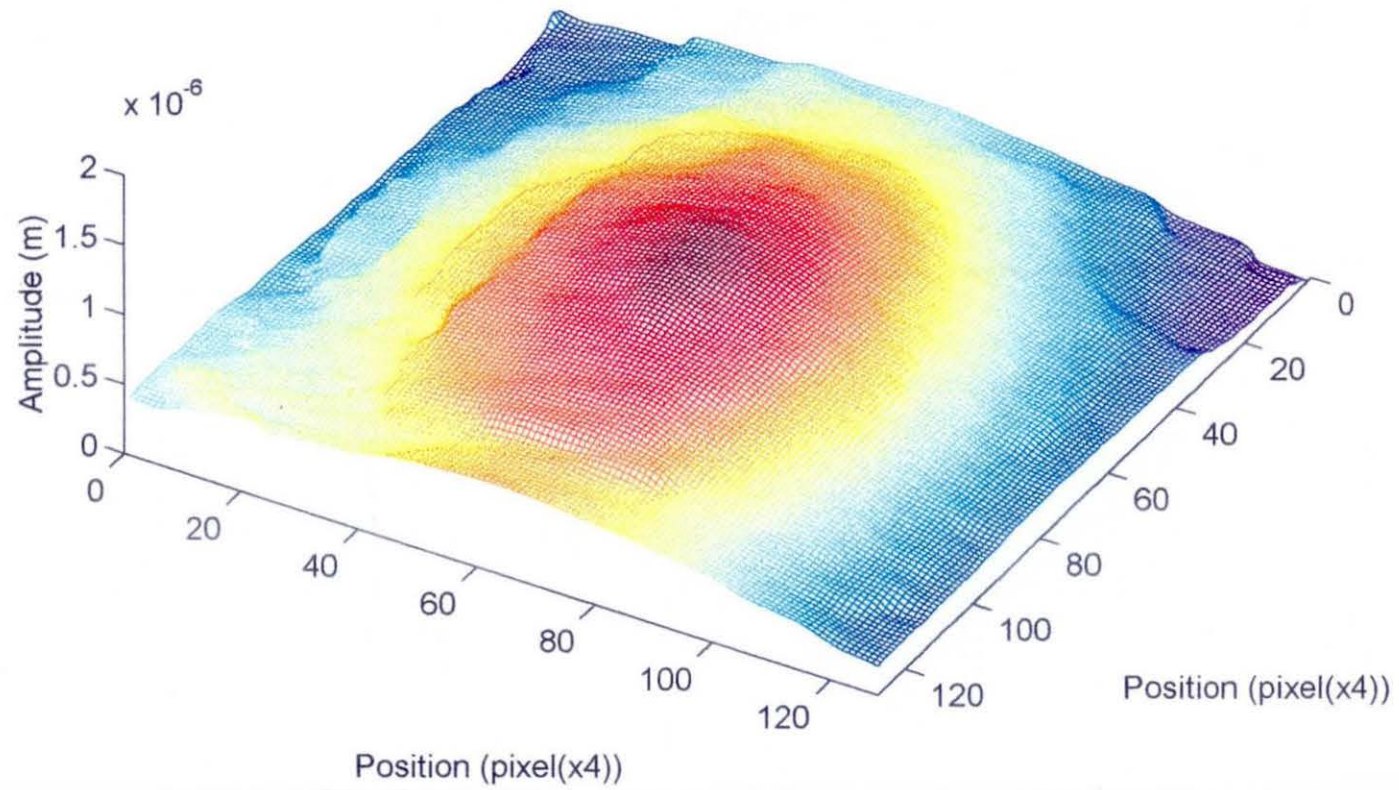


Figure 8.4: Wire frame plot of the displacement phase distribution after applying the cosine transform unwrapper to the phase map of Figure 8.3(c).

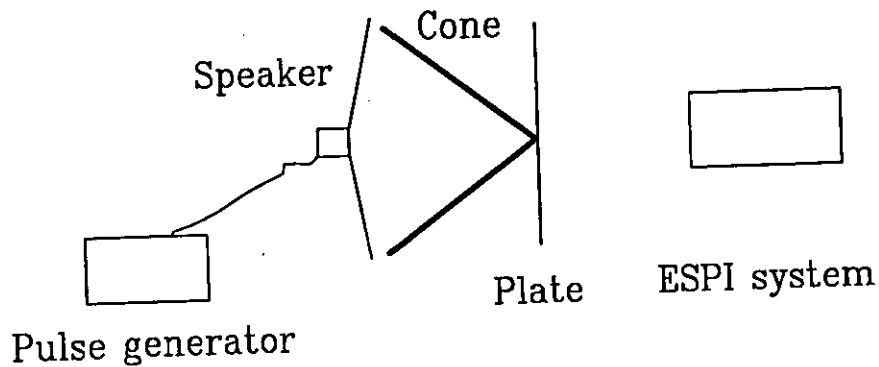


Figure 8.5: Experimental set-up to excite a plane plate by using a sonic pulse.

Pockel cell (around 25ns for our device), data acquisition speed is therefore limited only by camera frame rate and laser twin-pulse repetition rate.

The previous experimental results presented here using the CW laser can be extended if the electro-optical system is used with a Nd:YAG pulsed laser. As a preliminary test, single pulse subtraction carrier fringes were first obtained. Each pulse was synchronized at the camera frame rate so when one frame was grabbed and subtracted from the subsequent frames and a change in polarization of the Pockels cell was introduced, the carrier fringes were seen in real time.

To test this system in a transient experiment, a plastic plane plate was excited by means of sonic pulses using a cone in front of a loudspeaker as shown in Fig. 8.5. When no excitation was used, each frame gives a carrier fringe pattern. When the mechanical wave strikes the plate the carrier fringes are seen to become modulated. The event was first recorded in a video recorder and then replayed to grab a sequence of four frames shown after applying a

low-pass filter in figure 8.6. Each carrier fringe pattern shown in this figure was separated by a time delay of 40ms.

Figures 8.7 and 8.8 show consecutively the wrapped and unwrapped phase maps obtained after processing the carrier fringe patterns shown in Figure 8.6 and after applying the cosine transform phase unwrapper.

As was seen in section 2.6.3 the main drawbacks of bandwidth reduced range, resolution and noise problems associated with the carrier fringes are all present in this experiment.

Tests by the author (see Table 8.1) using a centre loaded target plate indicate that if this separability condition alone determines the maximum measurable displacement, there is no significant reduction in measuring range for the carrier fringe technique. An estimation of the practical upper displacement limit for 'conventional' out-of-plane ESPI subtraction was 25 fringes, giving an equivalent central displacement magnitude of $6.43\mu\text{m}$. As can be seen, this equates to the maximum displacement measurable by the carrier fringe technique for this target, assuming lobe separability limitations only. However, the higher frequencies of the broadened side bands must still be resolved by the system. This resolution depends on the camera and processing electronics as well as on the speckle size. In Table 8.1, both the lobe separability and frequency resolution limitations (as implied by Equation 7.1) were found to hold up to around a central displacement of $3.6\mu\text{m}$ with 28 carrier fringes. Thus the method would seem to have little over half the measurement range of conventional ESPI for this target.

The fringe visibility becomes a problem for areas of poor illumination or low

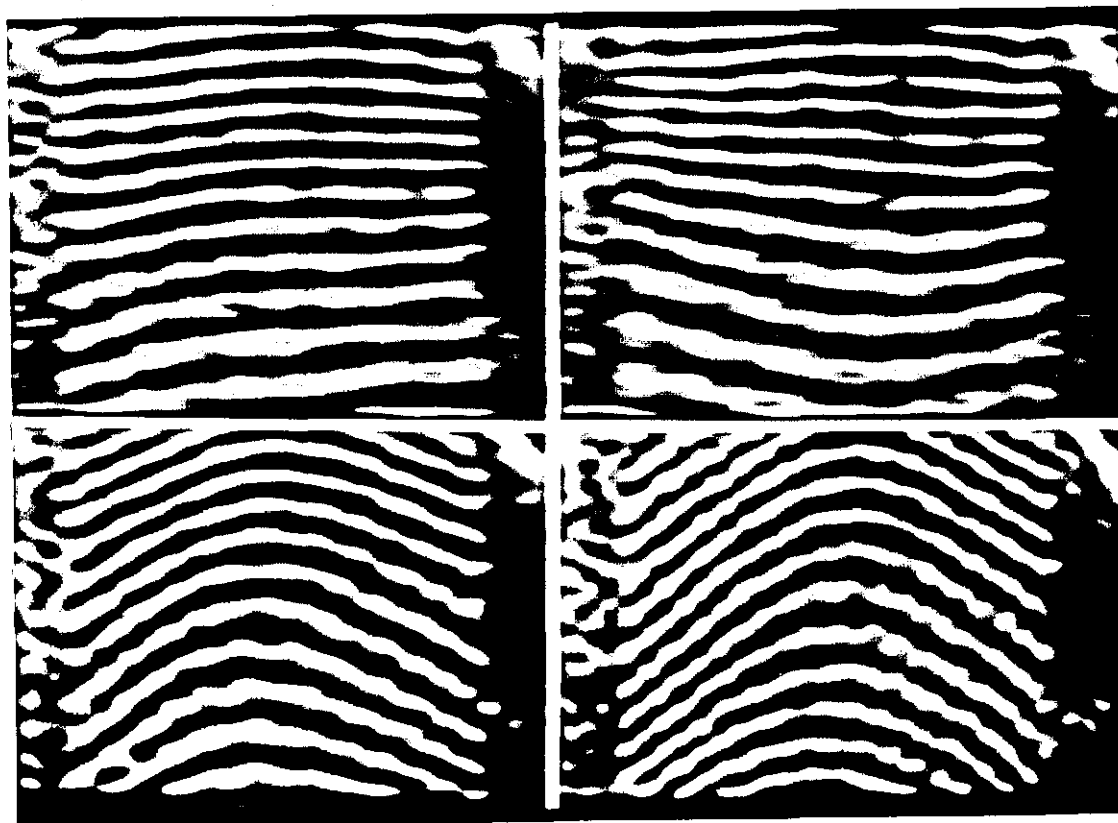


Figure 8.6: Sequence of four frames of a transient event in time intervals of 40ms obtained by the application of a low-pass filter in the ESPI carrier fringes.

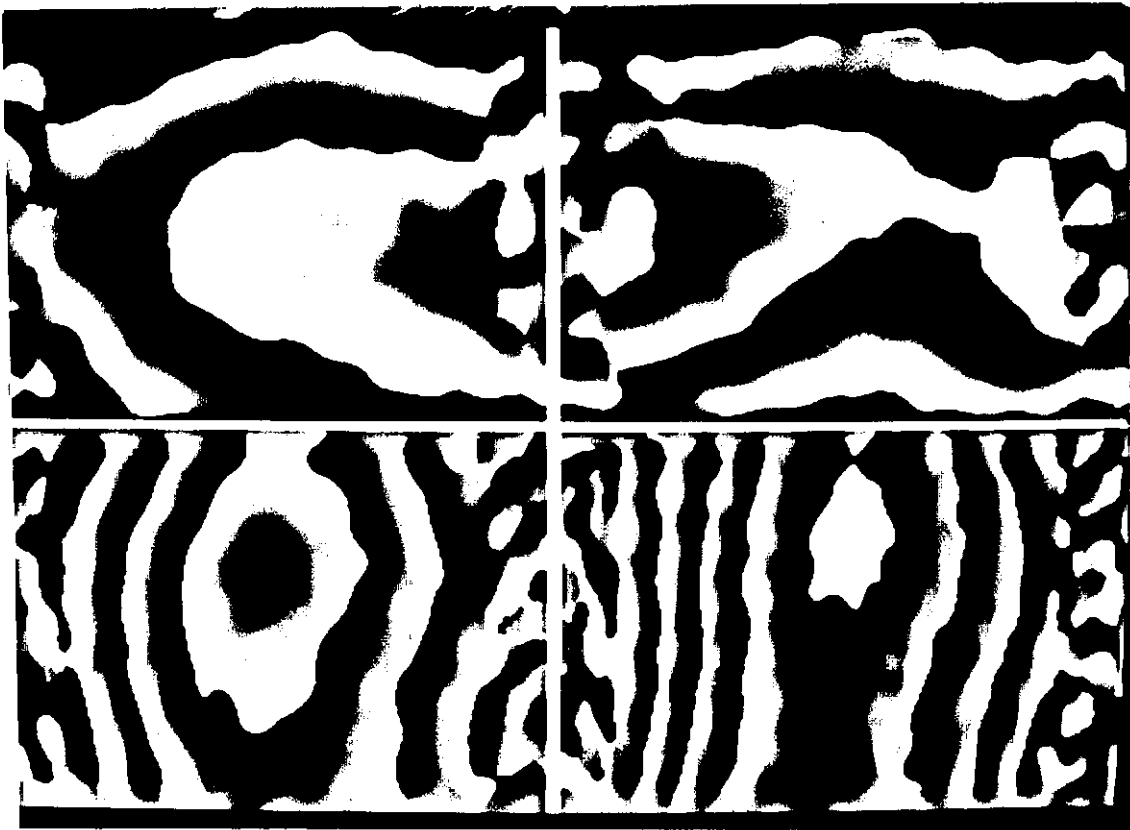


Figure 8.7: Wrapped phase maps obtained after processing the carrier fringe patterns shown in Figure 8.6.

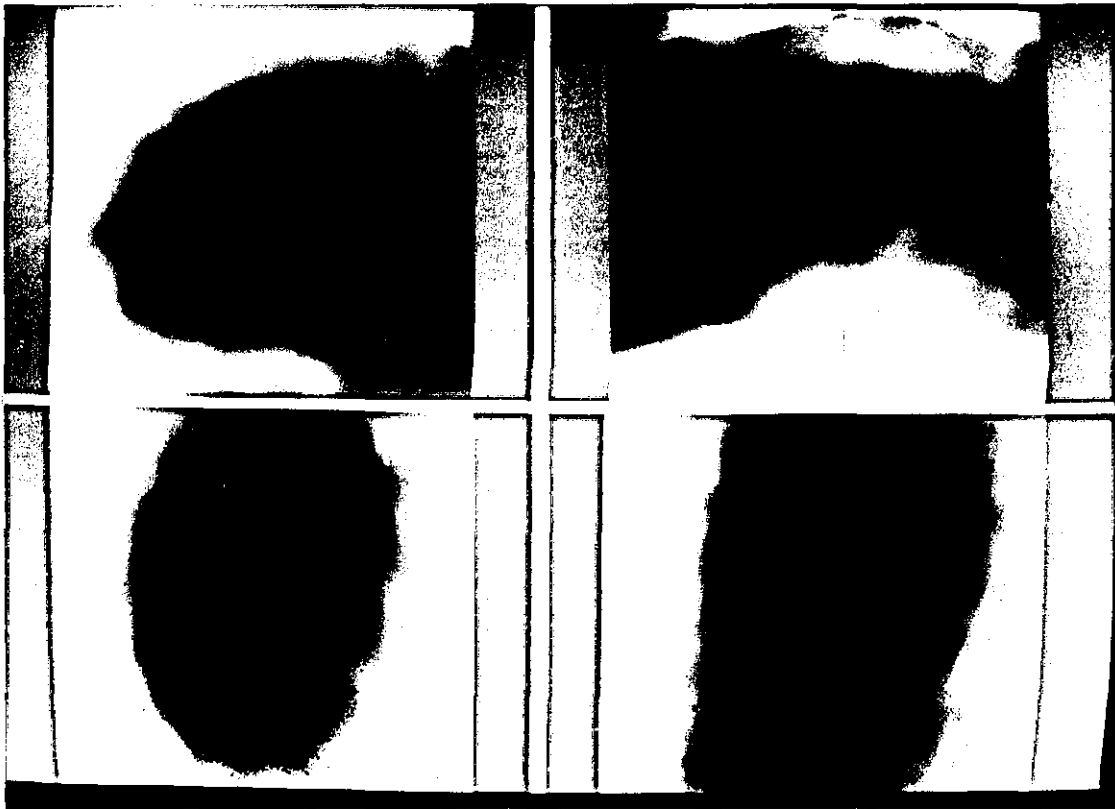


Figure 8.8: Unwrapped phase maps obtained after applying the cosine transform phase unwrapper to the phase maps of Figure 8.6.

No. of Carrier Fringes	Carrier frequency (/pixel)	No. of equivalent ESPI fringes	Plate Central Displacement (μm)
4	0.008	2	0.51
8	0.016	3	0.77
12	0.023	5	1.29
16	0.031	7.5	1.93
20	0.038	9.3	2.39
24	0.047	11	2.83
28	0.055	14	3.60
47	0.092	25	6.43

Table 8.1: Modulation limit for a fixed number of carrier fringes at a given displacement of the target surface.

surface reflectance; the effect is readily apparent in the lower left corner of Figures 8.3(a) and 8.3(c). In this case, a poor quality, badly optimized spatial filter in the interferometer has caused uneven illumination in the reference wavefront, resulting in reduced speckle modulation in this area.

The electro-optical system presented here allows also the introduction of carrier fringes between the firing of two laser pulses in pulsed addition ESPI. Although a standard frame transfer CCD is employed, the laser pulse separation is not unduly restricted. Figure 8.9 shows a schematic diagram with the change of polarization of the Pockels cell used to introduce addition carrier fringes indicated in dotted lines. When the rise time of the Pockels cell is made to coincide in time with the interval of time between the twin pulses carrier addition fringes can be generated in times as short as 25ns for the Pockels cell used in the experiment. The pulse width in this case was of 300ns and the recovery time of the cell to produce horizontal polarization was of $3\mu\text{s}$.

To conclude, the system allows unambiguous calculation of the wrapped phase distribution using the Spatial Synchronous Detection method from a single fringe pattern. Quantitative phase measurements using a CW laser have been performed on a metal plate subjected to out-of-plane displacement to illustrate the performance of the approach. As a complementary experiment a transient event was analyzed using a Nd:YAG laser in single pulse mode and the electro-optical system. Finally, a synchronization procedure was described to obtain carrier addition fringes.

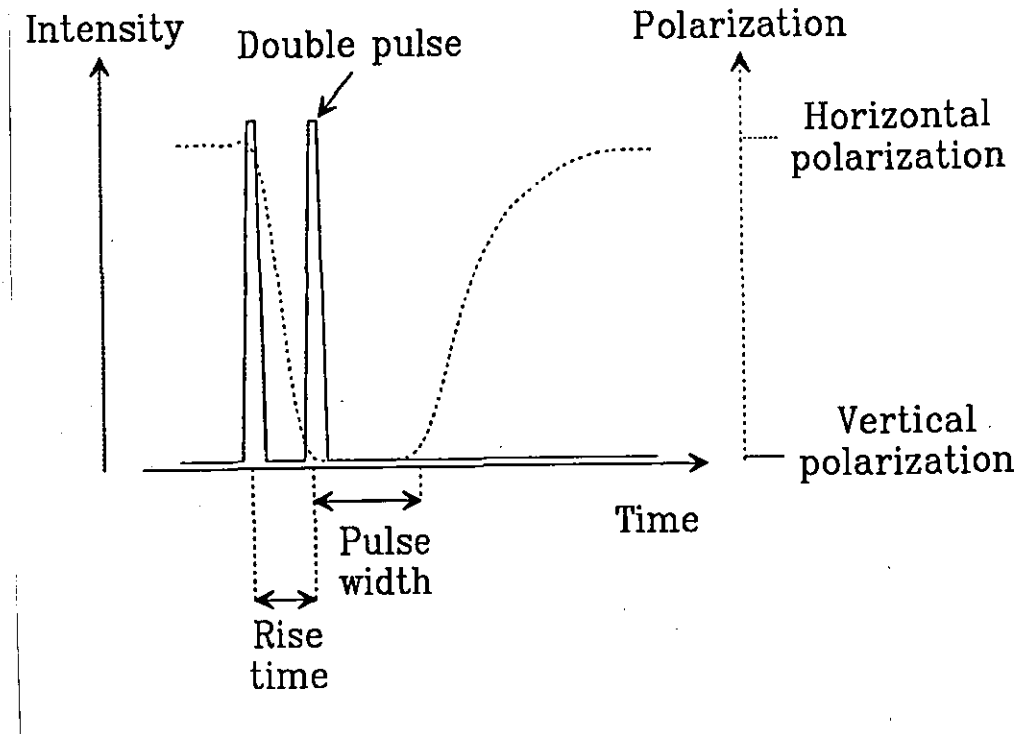


Figure 8.9: Schematic diagram of the Pockels cell change of polarization synchronized with a twin pulse in time. Left axis and continue line show the intensity of the twin pulse. Right axis and dotted line shows the polarization changes.

The accuracy and range of the method are less than those of 'conventional' phase stepped ESPI, the overall measuring range being about half that of out-of-plane subtraction fringes for the target tested. However, the significant advantage of the method lies in its ability to capture very fast transient displacements. It must therefore be emphasized that large deformations over such short (tenths of microseconds or less) time periods represent unusually large stress factors which would not normally be encountered. In any case, the laser pulse separation can be reduced, to compensate for larger displacement amplitudes, down to 50ns or lower for this technique, dependent on the Pockels cell used.

8.2 Discussion of Trade-offs

To summarize, it can be seen in the last sections that whole field transient event analysis can be performed by using different approaches based on different ways of expressing the phase in the ESPI interferogram and by using different hardware.

Of particular interest for detection of fast transient events is the capability of the reviewed systems for handling small time delays between pulses. The length in time of these delays allows the analysis of transient events at different scales of displacement. Thus, given our limited range of distance measurement and controlling this delay, it is possible to capture a event evolving at unknown speed by adjusting the delay to fit the magnitude of the event. To reconstruct successfully the time evolution of a transient event, it is necessary to record enough equi-spaced samples of the event in order

to be within the Nyquist sampling limit. If a successive set of twin pulses is used, then the time separation between sets of twin pulses will determine this limit. For equi-spaced samples it is also convenient to choose the minimum number of samples allowed by the Nyquist limit: a lower the number of frames will greatly benefit the frame transference rate. This semi-continuous sampling requires a pulsed laser producing pulses at the Nyquist frequency and a high speed transference of the fringe patterns to a recording device. In this case it is important to avoid delays in the transference of the aquired fringe patterns.

The multi-camera approach [73] allows the simultaneous recording of three separate phase steps, offering the advantage of operation and transference of the fringe patterns at the camera speed. However, the tranference of three fringe patterns is time consuming and requires a threefold increase in the number of transmission lines and processors that handle the generated data. Also, it is a complicated optical set-up with a large number of optical elements in which special calibration procedures are required and the possibility of optical misalignments increases in proportion to the number of optical elements.

On the other hand, this method gives strong intensities in the CCD plane by using a small speckle size. Unfortunatley, at least in one third of the collected intensity is lost due to the reduction of light caused by the beam splitters and external reflections in the optical surfaces of the elements that form the system.

Several contrasting points can be noted when a comparison of the multicamera technique versus the spatial phase-shifting technique (SPS) [75] is made.

First it can be seen that in the SPS technique there is a time delay introduced when the two speckle fields are recorded in the interlaced fields. As both fields are transferred sequentially, a camera switching time is introduced between fields. This switching time makes this technique of non-simultaneous character in comparison with the multi-camera approach. Even though this time can be as small as $5\mu\text{s}$ it defines a lower limit in the time in which the events can be recorded. Nonetheless, this technique can cope very successfully with the analysis of vibrations found in some engines and turbines (i.e. $\leq 5\text{ kHz}$) as well as with the analysis of transient events using twin pulses with a time delay of the mentioned camera switching time. Unfortunately, the amount of light received in each camera frame is reduced strongly due to the large speckle size in the interline geometric distribution.

When the technique proposed by the author is compared with the other mentioned techniques, it can be seen that it is a non-simultaneous acquisition in comparison with the multicamera technique. However, it only requires processing of a single interferogram, while in the others techniques the processing time is increased in proportion to the number of interferograms (two for the SPS and three for the multicamera techniques). The multicamera approach acquires the speckle interferograms simultaneously, but the number of processors must be increased to deal with three interferograms. Also, it should be noted that the switching of a solid state pulsed laser is usually performed by Pockels cells, so the shortest time that can be obtained between consecutive pulses is dictated also by a Pockels cell response time. Under this circumstance, the additional advantage of using simultaneous acquisition could not be so relevant if it is limited by the twin pulse separation. On the other hand, the proposed technique does not suffer from a decrease of

intensity -as in the SPS and multicamera techniques- while achieving switching capabilities of the order of the twin pulse separation (i.e. $\approx 20\text{ns}$). As seen in the previous chapters, the proposed technique has a limited range of resolution in displacement of approximately half the range of resolution of conventional techniques. However, this is not a problem for analysis of transient events given the possibility of decreasing the separation between pulses and so obtaining a reduction in the observed range of displacement.

All the techniques discussed depend strongly on the camera technology and on the transference of the acquired interferograms for recording or for processing. If a continuous coverage in time of the transient events is desired the main limiting factor in commercial cameras is the field transfer rate of 50 Hz (CCIR/PAL field rate). Even with the method proposed by the author in which a single addition interferogram is transferred, only one frame can be transferred every 40 ms. To improve the transference rate, faster cameras are needed. Unfortunately, the camera technology increases in price with the speed. Another limitation is also introduced if the acquired data is transmitted to a computer (camera-to-computer transference), in this case the computer is used as a recording device and processing if possible. The computer bus is then capable of handling just a number of bytes per second. For the most modern buses such as the PCI, the transference rate is limited to 65 Mb/s or 991 images per second of 256×256 bytes allowing to transfer images to computer memory (or to fast hard drive) at a rate of 1 ms per frame. Assuming this transference rate, the analysis of vibrations at 1KHz (1ms of time period) will become soon a reality. However, to analyze vibrations of 5 kHz a frame transference of 0.2ms ($1/5\text{kHz}$) will be necessary. Thus, to achieve this camera-to-computer transfer rate an improving factor

in transference of ≈ 5 times is required. On the other hand, if the fringe pattern data is gathered by a high speed camera and transferred to a high speed video-recorder, the play-back at lower speeds can give enough time to transfer and analyze data at lower speeds. However, an inevitable loss of spatial resolution is usually obtained by using high speed video. In any case, the advantage of processing a single interferogram is evident.

The transfer rates limitations are defined by the hardware involved and the actual technology. For the camera-to-computer transference rate, it implies that a variable speed acquisition technology is more suitable to supply images at different resolutions and/or speeds. It is more convenient due to the increased transference rates obtained by reducing resolution and also because of the variable times introduced by computer processing. For the camera-to-video and then video-to-computer transference the solution is usually expensive due to the specialized devices needed.

To conclude, the carrier fringe technique is a more simple way of extracting the phase information, it does not decrease the object intensity, it can be used for the analysis of very short transient events, a single fringe pattern can be transferred in shortest times to a storing device and computer processing is faster.

Chapter 9

Discussions and Conclusions

9.1 Future of Opto-Electronic Developments

The future of the technology for displacement measurement by non destructive techniques can be seen as two and three dimensional quasi-continuous displacement measurement. The use of single point optical techniques has only been successful due to the low resolution in time of the whole field and 3D measurement techniques. A comparison of the transference bandwidth figures mentioned in section 8.2 for the camera-to-computer transference of images of 256x256 bytes and in section 1.1 for the LDV shows that to acheive similar magnitudes it is necessary to improve the actual values of camera-to-computer transference time by a factor of 50. If smaller processing times for whole field measurement techniques could be obtained, an improved resolution would give more advantages for the quasi-continuous analysis of displacements. The analysis of this data in the frequency domain could also

provide in the near future the necessary data for whole field modal analysis. All this depends on the availability of faster optical techniques combined with fast cameras and digitising electronics to gather the displacement data, and with the availability of fast processors to cope with the large amounts of data generated.

Nowadays, it is easy to observe the growing tendency to transform electronic devices to provide high response times and improved quality. This tendency can be seen in computer technology, in which the average time for doubling the processing speed is just two years. The new improved capabilities of handling large amounts of data will certainly improve the ESPI processing systems to obtain smaller processings times in the coming years.

Semiconductor laser technology is also evolving rapidly and is merging with the old laser technology. Nowadays, diode lasers are replacing the flashlamps previously used in Nd:YAG lasers giving more flexibility in the synchronization of the pulse repetition rates. Also, the associated problems of laser diode technology such as lack of coherence and elliptical beam profiles are being tackled. New integrated systems with fiber optics have nearly gaussian beam profiles and can oscillate at 0-2Mhz, having coherence lengths from 10 meters in the case of continous emission to a few millimeters for high frequency oscillations. These capabilities allow the generation of more pulses per second than so far obtained in solid state lasers.

Although these systems are more compact in size and cheaper than the solid state lasers, they have a number of intrinsic problems to acheive the Nd:YAG capabilities. First semi-conductor lasers are usually switched with a fixed time interval between pulses that in the shortest time acheivable is still

greater than the minimum lapsed time between pulses of a Nd:YAG twin pulse (e.g. $\approx 500\text{ns}$ vs. $\approx 20\text{ns}$). Thus it is necessary to improve the pulse repetition rate to achieve similar lapsed times between pulses. Secondly, and ignoring the possible thermal effects, a custom made electronic driver is required to generate a single pair of pulses with a low frequency (50Hz) repetition rate.

The technical problems associated with semiconductor lasers seems to have a short term solution. Thus it is easy to see that in a few years the pulsed capabilities of this technology will make diode lasers the preferred replacement of the Nd:YAG pulsed lasers.

9.2 Assessment of Speckle Noise

Computer simulated speckle has been shown to be useful for the generation of error-free ESPI patterns in the out-of-plane, in-plane and shearing equivalent optical configurations. For the out-of-plane configuration the effect of sampling and the influence of the reference beam has been described using the probability density functions generated by the computer model. The effect of addition and subtraction correlation has also been described in the same way. It can be concluded that a slight change in the aperture or relation between interfering beams would produce changes in the PDF so some *a priori* knowledge function must be adopted for every particular situation in ESPI.

The computer generated ESPI fringe patterns provide a robust technique to

assess the performance of the enhancement and noise reduction techniques without the inconveniences of experimental errors.

A methodology to assess the results of any noise reduction approach in the spatial, frequency and phase domains has been suggested and used to assess the performance of diverse noise reduction techniques. It was seen that to assess the noise reduction techniques it is necessary to use two different parameters, the fidelity and the speckle index parameters.

In terms of assessing the quality of the displacement measurement, an evaluation of the whole ESPI process is extremely important for definition of international standards. Also, calibration procedures and traceability would be beneficial in order to reduce uncertainty and provide confidence for industrial users.

9.3 Noise Reduction Techniques

In the section on noise reduction, the performance of various techniques when applied to ESPI fringe patterns has been assessed. It can be noticed that the best performance is achieved by the techniques that preserve the object details while smoothing the speckle. Also, it is observed that the most successful algorithms are of a nonlinear nature, a natural consequence produced by the random characteristics of the speckle correlation.

The role of noise reduction has been discussed in relation with the subsequent stages for the overall processing of ESPI fringe patterns. As noise is the main problem, it was shown to be present from the correlation stage of the speckle

fields and hence affects all the subsequent processing stages. As all the ESPI processing stages try to reduce the noise, there is not an ideal place in which it can be reduced more efficiently. However, it has been emphasized that the reduction of noise should not affect the shape of the object under analysis, in the same way if the noise is reduced in the subsequent stages this should be taken into account.

It is the belief of the author that a robust ESPI noise reduction algorithm has an optimum position in the ESPI data processing algorithm: it must be applied immediately after the correlation process. In this way the subsequent stages of phase extraction and unwrapping can be optimized to process only clean fringe patterns without introducing adverse effects to the displacement values by simultaneously attempting to reduce noise. If not, the final results can be erroneous due to error propagation through all the ESPI processing stages.

Double pulse addition fringes have been enhanced by two methods: by subtraction of a reference beam and by zero order removal followed by a contrast transformation. The second method can be implemented in real-time using a fast digital signal processor. The conditions for observing the addition enhanced fringes has been also discussed.

9.4 Phase Extraction

The standard algorithms for phase extraction using phase stepping and carrier fringes have been reviewed.

As software processing time is important in the case of ESPI transient systems, it can be noticed that in this situation, a single interferogram is more appropriate than several interferograms. This is seen when an increase in processing time occurs when noise reduction techniques are applied to more than one interferogram. Hence from these observations, the carrier fringe extraction method can be seen to be faster than the techniques that require more than one interferogram. An additional advantage of the carrier fringe method is that can be easily implemented in a digital signal processor, such as the C80 from Texas Instruments.

The phase unwrapping algorithm used in this work was explained and tested in performance for some particular cases in which some minor deficiencies were shown. As was observed in the relevant section, the most appropriated unwrappers for transient event detection are those performed in the least possible time while preserving the object details and correct phase distribution.

9.5 Systems for Transient Event Detection

The most promising whole field optical systems suitable for transient event detection using ESPI have been reviewed. It was seen that the less complex and more efficient system is the one proposed by the author. This system allows unambiguous phase extraction from a single addition or subtraction correlated interferogram.

A system designed to analyze transient phenomena must utilise an optical

system able to produce the necessary interferograms to obtain the phase data in a straightforward way; ready for subsequent software and/or electronic processing. If phase is calculated using software, it must be highly efficient in time while producing in its output a high quality phase measurement. In a later stage, the software calculations can be incorporated into a special purpose electronic device with lower responses times.

It is the believe of the author that further work must be oriented to the research and characterization of ESPI software techniques (section 2.4.1), optimized in time for the case of "transient systems". Also, these techniques must not give misleading or distorted phase values, by improper or unoptimized algorithms. This can be checked by using the assessment techniques discussed in section 4.2. If an efficient integration of optics, electronics and software is incorporated in a transient system, the next logical step would be to optimize the software techniques by transferring them into DSP hardware like the C80 from Texas Instruments.

9.6 Future Applications in ESPI

Assuming that a high speed ESPI system with time resolutions similar to those obtained in the LDVs is built, it will eventually replace the LDV scanning systems providing the same kind of whole field studies. Of particular importance is the ability to obtain a modal and frequency analysis in the study of vibrating objects. This studies will be provided with such technology with the possibility of analysing the instantaneous whole field of view

as an added bonus. This last feature will provide a better understanding of phenomena such as crack propagation and shock wave transmission.

Whole field transient event analysis can also provide energy measurements, that are becoming more important as the optimization of energy transmission is starting to be a critical concern in structural engineering. This new measurement capability will improve the design of energy-efficient mechanical systems and by consequence save important amounts of energy. A crucial factor in energy measurements is the analysis of power flow in which a good time-resolution is necessary to extract the evolution in time of the first and second order derivatives of displacement or strain.

Using a similar approach to tomography, the whole field analysis of transient events can be used for the study of internal defects in materials. In this case, a decrease in the energy of the travelling mechanical wave is produced by hidden structures inside the material. As internal masses affect in a 3D way the distribution of energy, and only an external view of the displacement is made by the present optical systems, the 3D techniques would provide a deeper understanding of this phenomena. This will be possible only by using transient analysis systems, but for oscillating objects the continuous pumping of energy into the system might make the analysis more difficult.

The variety and complexity of possible solutions requires still a great amount of research towards faster techniques. The solution presented in this thesis for the unambiguous phase extraction problem from a single interferogram using the fast electro-optical system can be seen as a promising start in the search for such techniques.

To conclude, it is hoped that in the near future this work will contribute towards making the pulsed ESPI technique a useful alternative to other optical techniques for dynamic analysis, and will offer the possibility of tackling more complex engineering problems.

GLOSSARY

f	Focal length.
x, y	Horizontal and vertical spatial coordinates.
U	Wavefront complex amplitude.
\hat{U}	Sampled complex amplitude wavefront.
Ψ	Random phase.
\hat{m}, \hat{n}	Integer spatial coordinates.
$N \times N$	Square matrix integer dimensions.
N	Number of rows in a matrix.
r	Radius of a circular low pass Fourier filter.
$\hat{\sigma}_0$	Subjective speckle size from a computer simulation of a speckle field.
u, v	Integer coordinates in the frequency domain.
i, j	Horizontal and vertical integer coordinates in the spatial domain.
\mathcal{F}	Fourier transformation.
\mathcal{F}^{-1}	Inverse Fourier transformation.

x_1, y_1	Horizontal and vertical spatial coordinates in a scattering plane.
\bar{r}	Radius of an optical system exit pupil.
I	Intensity.
H	Low pass Fourier filter.
$\langle I \rangle$	Mean intensity.
$p(I) \langle I \rangle$	Normalized probability density function.
σ_I	Standard deviation of intensity.
$\langle I_N \rangle$	Intensity average of a speckle field plus a coherent background.
I_0	Modified Bessel function of the first kind, zero order.
$p_I(I) \langle I_N \rangle$	Normalized probability density function for the sum of a speckle pattern and a coherent background.
$p_A(I)$	Normalized probability density function for the intensity addition of two uncorrelated speckle fields.
$p_B(I)$	Non-normalized probability density function for

	the intensity addition of two uncorrelated speckle field plus coherent background.
I_1, I_2	Random intensity values inside the speckle size for two speckle fields.
$\sigma_{I_1}, \sigma_{I_2}$	Standard deviations of random intensity values inside the speckle size for two speckle fields.
\hat{I}	Intensity of a simulated speckle field for an out-of-plane ESPI.
$\Delta\alpha$	Phase change introduced by a deformation in the ESPI simulation of an object under test.
R	Amplitude of a reference beam in a simulated out-of-plane ESPI.
φ	Phase of a reference beam in a simulated out-of-plane ESPI.
ζ	Phase of a symmetrical illumination in a simulated in-plane ESPI.
\hat{i}	Defined as $\sqrt{-1}$.
S^-, S^+	Symmetrical amplitude speckle fields for a simulated shearing ESPI.
\hat{m}_0	Shear distance introduced between two sheared speckle fields in a simulated shearing ESPI.

\hat{f}	Uncorrupted image for quality assessment.
g	Corrupted image for quality assessment.
Φ	Image fidelity parameter for quality assessment.
$\bar{\Phi}$	Discrete representation of image fidelity parameter for quality assessment.
T	Relative structural content parameter for quality assessment.
Q	Correlation quality parameter for quality assessment.
s	Speckle index parameter for quality assessment.
σ_{ij}	Local standard deviation at pixel (i, j) .
\bar{I}_{ij}	Local average intensity at pixel (i, j) .
C	Speckle contrast.
N_0	Number of uncorrelated speckle patterns.
h	Impulse response function.
\hat{A}	Normalizing constant.
$\hat{\beta}$	Ratio between local standard deviation and local intensity.
σ_{I_0}	Local standard deviation.

t	One dimensional spatial coordinate.
x_0, y_0	Spatial location of pixel in the centre of a local neighbourhood.
$\hat{I}_{x_0 y_0}$	Averaged intensity in the two sigma range.
$I_{x_0 y_0}$	Intensity value in the centre of a local neighbourhood.
σ_{I_0}	Local variance in a square window.
$\pm n, \pm m$	Local limits for square window of size $(2n+1) \times (2m+1)$.
K	Threshold for reducing spot noise in the Lee filter.
I_2	Speckle field intensity values prior to correlation.
I_{12}	Intensity values after correlation of two speckle fields.
\hat{k}	constant for the spectral subtraction image restoration filter.
$\hat{\theta}$	Phase of $\mathcal{F}(I_{12})$.
ρ	Radius in the spatial domain.
C_1, C_2	Constants used to produce a simulated object deformation that gives curved fringes in a computer simulated out-of-plane ESPI.

λ	Wavelength of the light.
f	Inverse Fourier transformation of $I(u, v)$.
m	Integer used to represent an even number of fringes.
k, l	Spatial integer coordinates in a local neighbourhood of a i, j pixel.
I_{ij}	Intensity at pixel (i, j) .
$M \times M$	Square matrix dimensions of a local neighbourhood.
W	Limit defined as $W = (M - 1)/2$.
k, l	Spatial coordinates of a local neighbourhood.
q_{kl}	Weights that depend on the spatial coordinates k, l of a local neighbourhood.
p_{kl}	Weights that depend on the intensity values in a local neighbourhood.
α	Constant parameter defined as inversely proportional to the size M of a local window.
β	Local parameter defined as inversely proportional to the local variance.
σ_I^2	local variance.

\bar{I}_t	Average intensity of the pixels in a local neighbourhood.
I'	Transformed intensity values after a shifted exponential transformation.
ζ_0	Constant of the shifted exponential transformation.
I_{max}	Maximum intensity of the ESPI fringe pattern.
I_1	Correlation fringes generated by addition of two speckle interferograms.
I_0	Intensity of the object beam in an out-of-plane ESPI.
I_r	Intensity of a reference beam in an out-of-plane ESPI.
A, B	Constants expressed in terms of I_0 and I_r .
S	Number of steps for phase stepping.
F	Number of frames for phase stepping.
γ	Radians of a phase shift.
$\bar{\alpha}$	Phase function of an arbitrary fringe pattern.
a, b, c	Constant functions to re-express a fringe pattern.

\mathcal{A}, \mathcal{C}	Fourier transform of a and c .
ϕ	Wrapped phase values.
U_0	Complex amplitude of a plane reference wavefront.
\bar{k}	Wave number.
ϕ_0	Optical path of a reference wavefront.
$\bar{\phi}$	Wavefront optical path.
\bar{I}_a	Low-pass filtered version of I .
ψ	Wrapped phase values.
\bar{B}	Signal bandwidth.
$M \times N$	Rectangular dimensions of columns and rows of a wrapped phase array.
$\rho_{i,j}$	Discrete representation of Poisson equation.
Δ^x, Δ^y	Phase difference terms along horizontal and vertical directions.
W	Wrapping operator.
$\hat{\phi}$	Unwrapped phase values.
\bar{m}, \bar{n}	coordinates in the resulting values of the discrete cosine transform.

θ	Reference beam inclination in an out-of-plane ESPI configuration.
σ_0	Subjective speckle size of an optical system.
r_0	Radius of the optical system exit pupil.
$g_0, g_{-\pi/2}, g_{+\pi/2}$	Simulated fringe patterns correlated by subtraction with phase steps of $0, -\pi/2$ and $+\pi/2$ respectively.
\bar{I}	Sampled intensity of a simulated speckle pattern.
\hat{I}_t	Sampled intensity of a simulated speckle pattern with a tilted reference beam.
$\hat{\alpha}$	Phase introduced by the reference beam.
ϕ_p	Phase term.
f_0	Carrier frequency.
n_0	Index for horizontal lines.
I_s, I_c	Sine and cosine products of the intensity along an horizontal line.
G_s, G_c	Low pass filtered I_s, I_c .

Bibliography

- [1] T. J. Cookson, J. N. Butters, and H. C. Pollard. Pulsed lasers in electronic speckle pattern interferometry. *Optics and Laser Technology*, 10:119-124, 1978.
- [2] F. Mendoza Santoyo, D. Kerr, J. R. Tyrer, and T. C. West. A novel approach to whole field vibration analysis using a pulsed laser system. In *Proc. SPIE 1136*, pages 335-345, 1989.
- [3] G. Pedrini, B. Pfister, and H. Tiziani. Double pulse-electronic speckle interferometry. *Journal of Modern Optics*, 40 No. 1:89-96, 1993.
- [4] This kind of cameras are produced by Cordin Corporation 2230 South 3270 West, Salt Lake City, Utah 84119-1194, USA.
- [5] P. Hariharan. *Optical Interferometry*. Academic Press, 1985.
- [6] R. Jones and C. Wykes. *Holographic and Speckle Interferometry (2nd ed.)*. Cambridge U. Press, Cambridge, 1989.
- [7] J. N. Butters and J. A. Leendertz. Speckle pattern and holographic techniques in engineering metrology. *Opt. Laser Technol.*, 3:26-30, 1971.

- [8] S. D. Ramsey A. Macovski and L. F. Schaefer. Time-lapse interferometry and contouring using television systems. *Applied Optics*, 10 No. 12:2722–2727, 1971.
- [9] P. C. Montgomery. *Forward looking innovations in electronic speckle pattern interferometry*. PhD thesis, Loughborough University of Technology, Loughborough Leicestershire U.K., 1987.
- [10] J. M. Huntley. High speed laser speckle photography rotating mirror camera control-system and applications. *Optical Engineering*, 33 No. 5:1700–1707, 1994.
- [11] J. R. Tyrer. Two Laser Speckle Correlation. Pat. 8712933.
- [12] D. Kerr G. H. Kaufmann and N. A. Halliwell. Contrast enhancement of ESPI pulsed addition fringes. *Opt. Laser Eng.*, 20:25–34, 1994.
- [13] G. Pavic. Measurement of structure borne wave intensity, part i: Formulation of the methods. *Journal of Sound and Vibration*, 49(2):221–230, 1976.
- [14] G. Pavic. Structural surface intensity: An alternative approach in vibration analysis and diagnosis. *Journal of Sound and Vibration*, 115(3):405–422, 1987.
- [15] T. Kreis. Digital holographic interference-phase measurement using the Fourier-transform method. *J. Opt. Soc. Am.*, A **3**:847–855, 1986.
- [16] N. Halliwell. *Laser Vibrometry*. Chapman & Hall, London, 1993.
- [17] Vibrometers operator's manual for polytec vibrometer series ofv-3000 / ofv-302, ofv-501, ofv-502, 1994.

- [18] The 1994 newport catalog, 1994.
- [19] D. Post. *Handbook on Experimental Stress Analysis*, chapter 7. Mc Graw Hill, 1987. The Society for Experimental Mechanics.
- [20] J. S. Epstein. Moire interferometry, i and ii. *Optics and Lasers in Engineering*, 13 nos. 1 and 2, 1990.
- [21] C. B. Scruby and L. E. Drain. *Laser Ultrasonics, Techniques and Applications*. Adam Hilger, Bristol, 1990.
- [22] E. Archbold, J. M. Burch, A. E. Ennos, and P. A. Taylor. Visual observations of surface vibration nodal patterns. *Nature*, 222:263-265, 1969.
- [23] K. A. Stetson. New design for laser image speckle interferometer. *Optics and Laser Technology*, 2:179-181, 1970.
- [24] J. A. Leendertz. Interferometric displacement measurement on scattering surfaces utilizing speckle effect. *J. Phys. E: Sci. Instrum.*, 3:214-218, 1970.
- [25] E. Archbold, J. M. Burch, and A. E. Ennos. Recording of in-plane surface displacement by double-exposure speckle photography. *Opt. Acta*, 17:883-898, 1970.
- [26] J. N. Butters and J. A. Leendertz. *J. Phys. E: Sci. Instrum.*, 4:277-279, 1971 .
- [27] Gudmunn A. Slettemoen. Optimal signal processing in electronic speckle pattern interferometry. *Opt. Commun.*, 23:213-216, 1977.

- [28] Gudmunn A. Slettemoen. General analysis of fringe contrast in electronic speckle pattern interferometry. *Opt. Acta*, 26:313–327, 1979.
- [29] Gudmunn A. Slettemoen. Electronic speckle pattern interferometric system based on a speckle reference beam. *Appl. Opt.*, 119:616–623, 1980.
- [30] R. Spooren. Double-pulse subtraction TV holography. *Opt. Eng.*, 31 No. 5:1000–1007, 1992.
- [31] J. R. Tyrer. *Toward Commercial Realisation of wholefield interferometric analysis*. PhD thesis. Loughborough University of Technology, Mechanical Engineering Department, Loughborough, 1989.
- [32] B. Pfister, M. Beck, and H. Tiziani. Speckleinterferometrie mit alternativen phasenschiebe-methode an beispielen aus der defektanalyse. In W. Waiderlich, editor, *Laser in der Technik: Vortrage Des 10. Internationalen Kongresses Laser 91*. pages 63–67, Berlin, 1992. Springer-Verlag.
- [33] R. S. Sirohi. Speckle shear interferometry-a review. *Journal of Optics, Optical Society of India*, 13(4):95–113, 1984.
- [34] J. N. Petzing and J. R. Tyrer. In-plane electronic speckle pattern shearing interferometry: A theoretical analysis supported with experimental results. In *Photomechanics*, volume 2342, pages 27–36. SPIE, 1994.
- [35] S. Takemoto. Applications of holography and ESPI in geophysical sciences. In J. D. Trolinger, editor, *Optical Inspection and Testing*, volume CR46, pages 175–196. SPIE, 1992.

- [36] J. N. Petzing and J. R. Tyrer. Shearing interferometry for power ultrasonic vibration analysis. In *Recent Advances in Experimental Mechanics*, pages 631–636. J. F. Silva Gomes, 1994.
- [37] J. N. Petzing, J. R. Tyrer, and J. R. Oswin. Measuring flextensional transducer mode shapes underwater using laser speckle interferometry. In *Sonar Transducers '95*, volume 17 (Pt 3), pages 220–229. Institute of Acoustics, 1995.
- [38] S. N. Bobo. Shearographic strain assessment for inspection of fossil-fuel power plants. *Materials Evaluation*, pages 1308–1311, 1991.
- [39] D. Paoletti, G. S. Spagnolo, M. Facchini, and P. Zanetta. Artwork diagnostics with fiber-optic digital speckle pattern interferometry. *Applied Optics*, 32(31):6236–6241, 1993.
- [40] R. Tyrer J, C. Heras-Palou, and T. Slater. Three dimensional human femoral strain analysis using ESPI. In *Fringe Analysis '94*, pages 24–32, York University, 1994.
- [41] ESPI system for in-plane and out-of-plane displacement measurement, Ettenmeyer Germany.
- [42] B. F. Pouet and S. Krishnaswamy. Additive/subtractive decorrelated electronic speckle pattern interferometry. *Optical Engineering*, 32 No. 6:1360–1369, 1993.
- [43] C. J. Oliver. Information from SAR images. *J. Phys. D: Appl. Phys.*, 24:1493–1514, 1991.

- [44] L. J. Porcello, N. G. Massey, R. B. Innes, and J. M. Marks. Speckle reduction in synthetic-aperture radars. *J. Opt. Soc. Am.*, 66(11):1305–1311, 1976.
- [45] A. Ohya, S. Suta, I. Akiyama, T. Itoh, and M. Nakajima. Speckle noise-reduction using PM pulses. *Acoustical Imaging*, 17 Ch. 81:295–302, 1989.
- [46] T. M. Srinivasan, V. Srinivasan, and B. Suresh. Speckle noise model and its optional removal in ultrasound 2D B-scan images. In *Proc. of the annual international conference of the IEEE Engineering in medicine and biology society*, New York, 1988.
- [47] J. M. Huntley. Speckle interferometry: noise reduction by correlation fringe averaging. *Applied Optics*. 31 No. 14:2412–2414, 1992.
- [48] T. S. McKenchnie. Speckle reduction. In J. C. Dainty, editor, *Laser Speckle and Related Phenomena in Topics in Applied Physics Vol. 9*. Springer Verlag, Berlin, 1981.
- [49] A. Davila, G. H. Kaufmann, and D. Kerr. A scale-space filter for smoothing electronic speckle pattern interferometry fringes. *Submitted to Optical Engineering*.
- [50] A. Davila, G. H. Kaufmann, and D. Kerr. An evaluation of synthetic aperture radar noise reduction techniques for the smoothing of electronic speckle pattern interferometry fringes. *Modern Optics*, 42:1795–1804, 1995.
- [51] P. Varman and C. Wykes. Smoothing of speckle and Moiré fringes by computer processing. *Opt. Laser Eng.*, 3:87–100, 1982.

- [52] I. W. Bowler and K. Paler. Gabor filters applied to electronic speckle pattern interferometer images. *Proc. IEE Second Int. Conf. on Image Processing*, pages 24–26, 1986.
- [53] H. Zhi and R. B. Johansson. Adaptive filter for enhancement of fringe patterns. *Optics and Lasers in Engineering*, 15:241–251, 1991.
- [54] J. S. Lim. Techniques for speckle noise removal. *Opt. Eng.*, 20:670–678, 1981.
- [55] D. Kerr, F. Mendoza Santoyo, and J.R. Tyrer. Manipulation of the Fourier components of speckle fringe patterns as a part of an interferometric analysis process. *J. Mod. Opt.*, 36:195–203, 1989.
- [56] V. S. Frost, J. A. Stiles, K. S. Shanmugan, and J. C. Holtman. A model for radar images and its applications to adaptive digital filtering of multiplicative noise. *IEEE Transactions on pattern analysis and machine intelligence*, 4 No. 2:157–166, 1982.
- [57] T. R. Crimmins. Geometric filter for speckle reduction. *Applied Optics*, 24 No. 10:1438–1443, 1985.
- [58] J. S. Lee. Speckle suppression and analysis for SAR images. *Optical Engineering*, 25 No. 5:636–643, 1986.
- [59] J. W. Goodman. Some fundamental properties of speckle. *J. Opt. Soc. Am.*, 66(11):1145–1149, 1976.
- [60] C. Gonzalez Rafael and Paul Wintz. *Digital Image Processing*. Addison-Wesley Publishing company, 1987.

- [61] J. Gu, Y. Y. Hung, and F. Chen. Iteration algorithm for computer-aided speckle interferometry. *Applied Optics*, 33 No. 23:5308–5316, 1994.
- [62] J. M. Huntley. New methods for unwrapping noisy phase maps. In *Proceedings of International Conference on Interferometry*. To be published by the SPIE, May 16–20 1994.
- [63] D. C. Ghiglia and L. A. Romero. Robust two-dimensional weighted and unweighted phase unwrapping that uses fast transforms and iterative methods. *J. Opt. Soc. Am. A*, 11 No. 1:107–117, 1994.
- [64] Catherine Wykes. Use of electronic speckle pattern interferometry (ESPI) in the measurement of static and dynamic surface displacements. *Optical Engineering*, 21 No. 3:400–406, 1982.
- [65] Katherine Creath. *Interferogram Analysis*, chapter 4, pages 94–140. Institute of Physics, 1993.
- [66] J. M. Huntley and H. Saldner. Temporal phase unwrapping algorithm for automated interferogram analysis. *Applied Optics*, 32(17):3047–3052, 1993.
- [67] D. Kerr, F. Mendoza Santoyo, and J. R. Tyrer. Extraction of phase data from ESPI fringes using a single-phase-step method: A novel approach. *Journal of the Optical Society of America*, 7(5):820–826, 1990.
- [68] K. Hibino, B. F. Oreb, D. I. Farrant, and K. G. Larkin. Phase shifting for nonsinusoidal waveforms with phase-shift errors. *Journal of the Optical Society of America*, 12(4):761–768, 1995.

- [69] A. J. Moore, J. R. Tyrer, and F. Mendoza Santoyo. Phase extraction from electronic speckle pattern interferometry addition fringes. *Applied Optics*, 33(31):7312, 1994.
- [70] Manuel Servin Guirado. *Advanced Techniques for Fringe Analysis*. PhD thesis, Centro de Investigaciones en Optica, 1993.
- [71] K.H. Womack. Interferometric phase measurement using spatial synchronous detection. *Opt. Eng.*, 23:391–395, 1984.
- [72] V. I. Vlad and D. Malacara. Direct spatial reconstruction of optical phase from phase-modulated images. In E. Wolf, editor, *Progress in Optics*, pages 261–317. Elsevier Science, 1994.
- [73] A.J.P. van Haasteren and H. Frankena. Real-time displacement measurement using a multicamera phase-stepping speckle interferometer. *App. Opt.*, 33:4137–4142, 1994.
- [74] G. Jin, N. Bao, and P. S. Chung. Application of a novel phase-shift method using a computer-controlled polarization mechanism. *Optical Engineering*, 33(8):2733–2737, 1994.
- [75] G. Pedrini and H. Tiziani. Double-pulse electronic speckle interferometry for vibration analysis. *Applied Optics*, 33 No. 34:7857–7863, 1994.
- [76] J.C. Dainty. *Speckle Statistics and the detection of images in hologram reconstructions of bubble chamber tracks and other objects*. PhD thesis, Imperial College of Science, Technology and Medicine Blackett Laboratory, Optics Section, London, 1972.

- [77] A. R. Weeks and H. R. Myler. Computer-generated noise images for the evaluation of image processing algorithms. *Optical Eng.*, 32 No. 5:982–992, 1993.
- [78] I. Newton. *Optics, Book I, Prop. VIII, Prob. II*. Reprinted: 1952, Dover Publications, New York, 1730.
- [79] K. Exner. Uber die Fraunhofer'shen ringe, die quetelet'shen streifen und verwandte erscheinungen. *Sitzungsber. Kaiserl. Akad. Wiss. (Wien)*, 76:522, 1877.
- [80] H. M. Escamilla-Taylor. *Some Aspects of Speckle Patterns Produced by a Small Number of Scatterers*. PhD thesis, Imperial College of Science, Technology and Medicine Blackett Laboratory, Optics Section, London, 1990.
- [81] J.C. Dainty. The statistics of speckle patterns. In E. Wolf, editor, *Progress in Optics Vol. XIV*. North-Holland Publishing Co., Amsterdam.
- [82] J.C. Dainty. *Laser Speckle and Related Phenomena*. Topics in Applied Physics Vol. 9. Springer Verlag, Berlin, 1984.
- [83] Special Issue. Speckle in optics. Special Issue of the J. Opt. Soc. Am. Vol. 66, November 1976.
- [84] L. Allen and D. G. C. Jones. An analysis of the granularity of scattered optical maser light. *Physics Letters*, 7 No. 5:321–323, 1963.
- [85] R. N. Bracewell. *The Fourier transform and its applications*. McGraw-Hill, 1978.

- [86] J. M. Huntley. Speckle photography fringe analysis: assessment of current algorithms. *Applied Optics*, 28 No. 20:4316–4322, 1989.
- [87] B. D. Guenther, C. R. Christensen, and A. Jain. Digital processing of speckle images. In *Proc. IEEE Conf. on Pattern Recognition and Image Processing*, Chicago, IL., May 1978.
- [88] J. W. Goodman. Statistical properties of laser speckle patterns. In J. C. Dainty, editor, *Laser Speckle and Related Phenomena in Topics in Applied Physics Vol. 9*, pages 29–36. Springer Verlag, Berlin, 1984.
- [89] A. E. Ennos. Speckle interferometry. In J. C. Dainty, editor, *Laser Speckle and Related Phenomena in Topics in Applied Physics Vol. 9*. Springer Verlag, Berlin, 1981.
- [90] J. W. Goodman. Statistical properties of laser speckle patterns. In J. C. Dainty, editor, *Laser Speckle and Related Phenomena in Topics in Applied Physics Vol. 9*, pages 19–21. Springer Verlag, Berlin, 1984.
- [91] J. W. Goodman. Statistical properties of laser speckle patterns. In J. C. Dainty, editor, *Laser Speckle and Related Phenomena in Topics in Applied Physics Vol. 9*, pages 21–26. Springer Verlag, Berlin, 1984.
- [92] J. W. Goodman. Some effects of target-induced scintillation on optical radar performance. *Proceedings of the IEEE*, 53 No. 11:1688–1700, 1965.
- [93] W. K. Pratt. *Digital Image Processing*. Wiley, 1978.
- [94] E. H. Linfoot. Transmission factors and optical design. *J. Opt. Soc. Am.*, 46 No. 9:740–752, 1956.

- [95] M. Tur, K. C. Chin, and J. W. Goodman. When is speckle noise multiplicative? *Applied Optics*, 21 No. 7:1157–1159, 1982.
- [96] K. M. Crennell and I. W. Bowler. The smoothing of electronic speckle pattern interferometric images. *Optics and Lasers in Engineering*, 7:163–173, 1986/87.
- [97] C. H. Chen. Adaptive image filtering. *Proc. Pattern Recog. and Image Processing*, 8:259–270, 1979.
- [98] T. F. Knoll. Adaptive gray scale mapping to reduce registration noise in difference images. *Computer Vision, Graphics and Image Processing*, 33 No. 2:129–137, 1986.
- [99] D. T. Kuan, A. A. Sawchuk, T. C. Strand, and P. Chavel. Adaptive noise smoothing filter for images with signal dependent noise. *IEEE Trans. on Pattern Analysis and Machine Intelligence*, 7 No. 2:165–177, 1985.
- [100] J. S. Lee. A simple speckle smoothing algorithm for SAR images. *IEEE Trans. on Syst. Man and Cyber.*, SMC-13:85–89, 1983.
- [101] P. Dewaele et al. Comparison of some speckle reduction techniques for sar. In *IGARSS '90*, 1990.
- [102] N. Macfarlane and M. Thomas. Speckle reduction algorithms and their application to sar images. In *Proc. of the 10th Anniversary Conference on Satellite Remote Sensing*, Remote Sensing Society, Reading, 1984.

- [103] J. W. Goodman. Statistical properties of laser speckle patterns. In J. C. Dainty, editor, *Laser Speckle and Related Phenomena in Topics in Applied Physics Vol. 9*. Springer Verlag, Berlin, 1984.
- [104] F. J. Martin and R. W. Turner. SAR speckle reduction by weighted filtering. *Int. J. Remote Sensing*, 14(9):1759–1774, 1993.
- [105] J. S. Lim. Image restoration by short space spectral subtraction. *IEEE Trans. on Acoust. Speech Sig. Proc.*, 28:191–197, 1980.
- [106] Y. F. Wong. A non-linear scale-space filter by physical computation. In C. A. Kamm et al., editor, *Workshop on Neural Networks for Signal Processing*, pages 241–250. Proc. IEEE, 1993.
- [107] A. P. Witkin. Scale-space filtering. In *Proc. International Joint Conference on Artificial Intelligence*, pages 1019–1022, Karlsruhe, Germany, 1983.
- [108] J. Babaud, A. P. Witkin, M. Baduin, and R. O. Duda. Uniqueness of the gaussian kernel for scale-space filtering. *IEEE Transactions on Pattern Analysis and Machine Intelligence*, PAMI-8(1):26–33, 1986.
- [109] P. Perona and J. Malik. Scale-space and edge detection using anisotropic diffusion. *IEEE Transactions on Pattern Analysis and Machine Intelligence*, 12(7):629–639, 1990.
- [110] R.J. Green, J.G. Walker, and D.W. Robinson. Investigation of the fourier transform method of fringe pattern analysis. *Opt. Laser Eng.*, 8:29, 1988.

- [111] D. Kerr, G. H. Kaufmann, and G. E. Galizzi. Unwrapping of interferometric phase fringe maps using the discrete cosine transform. *Applied Optics*. In print.
- [112] S. M. Song, S. Napel, N. J. Pelc, and G. H. Glover. Phase unwrapping of MR phase images using Poisson equation. *IEEE Transactions on Image Processing*, 4(5):667-675. 1995.
- [113] D. C. Ghiglia and G. A. Mastin. Two-dimensional phase correction of synthetic-aperture-radar. *Optics Letters*, 14:1104-1106, 1989.
- [114] W. H. Press, B. P. Flannery, S. A. Teukolsky, and W. T. Vetterling. *Numerical Recipes: The Art of Scientific Computing*. Cambridge U. Press, Cambridge, 1986.
- [115] A. Davila, D. Kerr, and G. H. Kaufmann. Fast electro-optical system for pulsed ESPI carrier fringe generation. *Optics Communications*, 123:457-464, 1996.

